

TECHNISCHE UNIVERSITÄT MÜNCHEN
Fakultät für Physik

Human-sized X-ray Dark-field Imaging

Pre-clinical studies and translation of imaging methods

Jana Katharina Luise Andrejewski

Vollständiger Abdruck der von der Fakultät für Physik der Technischen Universität München zur Erlangung des akademischen Grades einer

Doktorin der Naturwissenschaften (Dr. rer. nat.)

genehmigten Dissertation.

Vorsitzender: Prof. Dr. Martin Zacharias

Prüfer der Dissertation: 1. Prof. Dr. Julia Herzen
2. Assoc. Prof. Martin Bech, Ph.D.

Die Dissertation wurde am 12.11.2021 bei der Technischen Universität München eingereicht und durch die Fakultät für Physik am 14.12.2021 angenommen.

Abstract

X-ray dark-field and phase-contrast imaging is based on small-angle scattering and phase-shifts that the X-rays experience when passing through a medium offering complementary imaging modalities. As these shifts cannot be observed directly, various methods have been developed to measure them. One of these methods is grating-based X-ray imaging. Here, the phase information of the X-rays is measured by interference patterns, generated by placing X-ray optical gratings in the beam path. Numerous studies demonstrated applications of dark-field and phase-contrast imaging in medical imaging and material sciences, both in two- and three-dimensions. Among the medical applications, especially lung imaging was found to be promising. First studies were restricted to a small field of view as the available grating size is limited. Therefore, a setup for dark-field thorax radiography of pigs and humans was developed and implemented as a scanning setup.

The results of this thesis can be divided into three sections. In the first section, two medical imaging studies were conducted. First, ex-vivo human and phantom measurements were used to determine the optimal tube voltage for X-ray dark-field thorax imaging. It was found that lower tube voltages than for conventional attenuation-based radiography provide strongest signal, highest contrast, and best image quality. Second, the dark-field signal strengths of other organs and body parts were investigated. Dark-field signal was also found in bones, due to calcifications, and foreign bodies. The next section describes an alternative acquisition method. Instead of moving the gratings during image acquisition, the sample was moved. A subsequent comparison of images from both acquisition methods showed comparable attenuation and dark-field images from both methods. The last section transfers two imaging methods from setups with a small field of view to setups with a large field of view. First, X-ray vector radiography, which measures the directional scattering of X-rays, was tested on large specimens such as bones. Then, a method similar to tomosynthesis was presented to obtain three-dimensional dark-field information. For this method, both the resolution in the third dimension was improved and the applied dose was reduced.

Zusammenfassung

Phasenkontrast- und Dunkelfeldbildgebung mit Röntgenstrahlen sind ergänzende Bildgebungsmodalitäten. Diese basieren auf Kleinwinkelstreuung und Phasenverschiebungen, die Röntgenstrahlen beim Durchdringen eines Mediums erfahren. Diese Verschiebungen können nicht direkt beobachtet werden, weshalb verschiedene Methoden entwickelt wurden, um sie zu messen. Eine von diesen ist die gitterbasierte Röntgenbildgebung. Dabei wird die Phaseninformation der Röntgenstrahlen anhand von Interferenzerscheinungen, welche mit Hilfe röntgenoptischer Gitter erzeugt werden, gemessen. Zahlreiche Studien haben Anwendungen der Phasenkontrast- und Dunkelfeldbildgebung sowohl in der medizinischen Bildgebung als auch in den Materialwissenschaften in zwei und drei Dimensionen gezeigt. Bei den medizinischen Anwendungen stellte sich besonders die Lungenbildgebung als vielversprechend heraus. Erste Studien waren auf ein kleines Sichtfeld beschränkt, da die verfügbare Gittergröße begrenzt ist. Daher wurde ein Aufbau für Thoraxradiografien für Schweine und Menschen entwickelt und als Scanaufbau implementiert.

Die Ergebnisse aus dieser Arbeit können in drei Teilbereiche unterteilt werden. Im ersten Teilbereich wurden zwei Studien zur medizinischen Bildgebung durchgeführt. Zuerst wurde mit Hilfe von ex-vivo Human- und Phantommessungen die ideale Röhrenspannung für Thorax-Aufnahmen bestimmt. Dabei wurde festgestellt, dass niedrigere Röhrenspannungen als in der klassischen schwächungsbasierten Radiographie das stärkste Signal, den höchsten Kontrast und die beste Bildqualität liefern. Anschließend wurden die Dunkelfeldsignalstärken anderer Organe und Körperteile untersucht. Es wurde auch Dunkelfeldsignal in den Knochen, aufgrund von Kalzifikationen und in Fremdkörpern gefunden. Der nächste Teilbereich befasst sich mit der Abänderung der Aufnahme-prozedur. Anstatt die Gitter während der Aufnahme zu bewegen, wurde hier die Probe bewegt. Ein anschließender Vergleich von Bildern beider Aufnahmemethoden zeigte vergleichbare Schwächungs- und Dunkelfeldbilder beider Methoden. Der letzte Teilbereich zeigt die Übertragung zweier Bildgebungsmethoden von Aufbauten mit kleinem Sichtfeld zu Aufbauten mit großem Sichtfeld. Zuerst wurde die Röntgenvektorradiographie, die die richtungsabhängige Streuung der Röntgenstrahlung misst, an großen Proben, wie Knochen, erprobt. Anschließend wurde eine Methode ähnlich zur Tomosynthese vorgestellt, um dreidimensionale Dunkelfeldinformation zu erhalten. Für diese Methode wurde sowohl die Auflösung in der dritten Dimension verbessert als auch die applizierte Dosis reduziert.

List of Publications

First-authored publications (peer-reviewed)

A. P. Sauter*, **J. Andrejewski***, F. De Marco, K. Willer, L. B. Gromann, W. Noichl, F. Kriner, F. Fischer, C. Braun, T. Koehler, F. Meurer, A. A. Fingerle, D. Pfeiffer, E. Rummeny, J. Herzen and F. Pfeiffer. Optimization of tube voltage in X-ray dark-field chest radiography. *Scientific Reports* 9, 8699 (2019)

J. Andrejewski, F. De Marco, K. Willer, W. Noichl, A. Gustschin, T. Koehler, P. Meyer, F. Kriner, F. Fischer, C. Braun, A. A. Fingerle, J. Herzen, F. Pfeiffer and D. Pfeiffer. Whole-body x-ray dark-field radiography of a human cadaver. *European Radiology Experimental* 5, 6 (2021)

A. P. Sauter*, **J. Andrejewski***, M. Frank, K. Willer, J. Herzen, F. Meurer, A. A. Fingerle, M. R. Makowski, F. Pfeiffer and D. Pfeiffer Correlation of image quality parameters with tube voltage in X-ray dark-field chest radiography: a phantom study. *Scientific Reports* 11, 14130 (2021)

J. Andrejewski, F. De Marco, K. Willer, W. Noichl, T. Urban, M. Frank, A. Gustschin, P. Meyer, T. Koehler, F. Pfeiffer and J. Herzen. Retrieval of 3D information in X-ray dark-field imaging with a large field of view. *submitted*

*: shared first authorship

Co-authored publications (peer-reviewed)

A. A. Fingerle, F. De Marco, **J. Andrejewski**, K. Willer, L. B. Gromann, W. Noichl, F. Kriner, F. Fischer, C. Braun, H.-I. Maack, T. Pralow, T. Koehler, P. B. Noël, F. Meurer, D. Deniffel, A. P. Sauter, B. Haller, D. Pfeiffer, E. J. Rummeny, J. Herzen and F. Pfeiffer. Imaging features in post-mortem x-ray dark-field chest radiographs and correlation with conventional x-ray and CT. *European Radiology Experimental* 3, 25 (2019)

F. De Marco, K. Willer, L. B. Gromann, **J. Andrejewski**, K. Hellbach, A. Bähr, M. Dmochewicz, T. Koehler, H.-I. Maack, F. Pfeiffer and J. Herzen. Contrast-to-noise ratios and thickness-normalized, ventilation-dependent signal levels in dark-field and conventional in

vivo thorax radiographs of two pigs. *PLOS ONE* 14(6), e0217858 (2019)

E. M. Braig, N. Roiser, M. A. Kimm, M. Busse, **J. Andrejewski**, J. Scholz, C. Petrich, A. Gustschin, A. Sauter, J. Bodden, F. Meurer, R. Korbel, F. Pfeiffer, J. Herzen, D. Pfeiffer. X-ray Dark-Field Radiography: Potential for Visualization of Monosodium Urate Deposition. *Investigative Radiology* (2020)

K. Taphorn, F. De Marco, **J. Andrejewski**, T. Sellerer, F. Pfeiffer, J. Herzen. Grating-based spectral X-ray dark-field imaging for correlation with structural size measures. *Scientific Reports* 10, 13195 (2020)

J. Scholz, N. Roiser, E. M. Braig, C. Petrich, L. Birnbacher, **J. Andrejewski**, M. A. Kimm, A. Sauter, M. Busse, R. Korbel, J. Herzen, D. Pfeiffer X-ray dark-field radiography for in situ gout diagnosis by means of an ex vivo animal study. *Scientific Reports* 11, 19021 (2021)

S. Pinzek, T. Beckenbach, M. Viermetz, P. Meyer, A. Gustschin, **J. Andrejewski**, N. Gustschin, J. Herzen, J. Schulz, F. Pfeiffer Fabrication of x-ray absorption gratings via deep x-ray lithography using a conventional x-ray tube. *Journal of Micro/Nanopatterning, Materials, and Metrology* 20(4), 043801 (2021)

Oral presentations

RSNA - *Detection of Monosodium Urate Crystals in X-Ray Dark-Field Radiography*, Chicago, USA, Dec. 2019

Poster presentations

XNPIG - *Tube voltage optimization in X-ray dark-field human chest radiography*, Sendai, Japan, Oct. 2019

IMXP - *Tube voltage optimization in X-ray dark-field human chest radiography*, Munich, Germany, Jan. 2020

ECR - *Tube voltage optimization in X-ray dark-field human chest radiography*, online, July 2020

Contents

1	Historical context	1
2	Fundamentals of X-ray physics	5
2.1	The electromagnetic spectrum	5
2.2	X-ray sources	6
2.3	X-ray interaction with matter	8
2.4	X-ray imaging	14
2.5	Dose calculations	16
3	Grating-based X-ray imaging	17
3.1	Talbot effect	17
3.2	Talbot-Lau interferometer for incoherent sources	18
3.3	Signal extraction	21
3.4	Setups with a large field of view	23
3.5	X-ray vector radiography	26
4	Body section imaging	28
4.1	Classical tomography	28
4.2	Tomosynthesis	30
4.3	Computed tomography	31
5	Large field of view Talbot-Lau interferometer	32
5.1	Setup hardware	32
5.2	Data acquisition and processing	36

6	Tube voltage optimisation in X-ray dark-field human chest imaging	42
6.1	Tube voltage optimisation at the <i>linescanner</i>	43
6.2	Tube voltage optimisation at the <i>patientscanner</i>	52
6.3	Summary	59
7	Whole-body X-ray dark-field radiography of a human cadaver	61
7.1	Methods	61
7.2	Results	62
7.3	Discussion and conclusion	66
8	Image acquisition with a moving sample	69
8.1	Acquisition of data	69
8.2	Adaptation of processing	70
8.3	Samples taken with the <i>table-scan</i> acquisition	72
8.4	Problems with the <i>table-scan</i> acquisition	76
9	X-ray vector radiography at the <i>linescanner</i>	79
9.1	Materials and methods	80
9.2	XVR images of a wood sample	80
9.3	XVR images of a calf femur	82
9.4	Conclusion	84
10	Retrieval of 3D information in X-ray dark-field imaging with a large-field-of-view setup	85
10.1	Imaging acquisition and processing	85
10.2	Proof of principle measurements	87
10.3	Improvement of the resolution in z-direction	89
10.4	Measurements with a clinical lung phantom	96

11 Conclusion and outlook	102
A Supplementary information of Sec. 6.1	104
Bibliography	106
Abbreviations	117
Symbols	118
Acknowledgements	122

1 Historical context

Today, X-ray imaging is an important tool for medical applications and material science as it allows to view the inner structure of objects without opening or destroying them. In 1895, W. C. Röntgen discovered X-rays during experiments with discharge tubes [Röntgen, 1895]. In his experiments, he noticed that the degree of X-ray attenuation depends on the material, for example that bones create a darker shadow than the soft tissue surrounding them. However, as the acquired images were only two-dimensional, the shadows of different objects often overlap. Therefore, at an early stage, attempts were made to obtain depth information from the X-ray images. In the first body section imaging methods, X-ray tube and detector film were moved in order to image objects in one plane as sharply as possible while blurring objects from other planes as much as possible [Ziedses des Plantes, 1932; Grossmann, 1935; Littelton, 1996; Wall, 2011]. For all these methods, a separate exposure had to be recorded for each focal plane, leading to a high dose applied to the sample [Wall, 2011]. In the mid-20th century, predecessors of today's computed tomography (CT) were developed [Tetelbaum, 1957; Korenblum, 1958; Cormack, 1963; Hounsfield, 1973]. By either rotating the sample and simultaneously moving the detector film or rotating source and detector around the sample, a sinogram of the focal plane was recorded. For back-projection, analogue electrical methods or computer based processing was used [Korenblum, 1958; Hounsfield, 1973]. The improvement in CT devices, like the use of cone beams, multi-line detectors and a spiral acquisition mode, resulted in a reduction of scan time and dose. Furthermore, due to an increase in computational power the reconstruction time was decreased. To this day, X-ray imaging continues to advance towards better resolutions, shorter exposure times and lower doses.

One drawback of attenuation-based (visible light and X-ray) imaging is that for similarly attenuating materials, image contrast is low. This problem was solved by F. Zernike for light microscopy in the first half of the 20th century. He achieved the image contrast by interference of the beam through the object and the background beam. Furthermore, Zernike also proposed a method of dark-field microscopy, in which the direct beam is blocked and only the scattered light reaches the image plane [Zernike, 1942]. In the beginning of the 20th century, it was proven that X-rays are part of the electromagnetic spectrum. Hence, many principles can be transferred from visible light to the X-ray regime. U. Bonse and M. Hart also used interferometry to detect phase-shifts of X-rays passing through an object [Bonse, 1965]. Their interferometer consisted of three crystals cut from a single crystal block and used two separate beam paths, of which only one passes through the sample. By analysing the interference pattern of the two beams, information about the phase-shift in the sample could be obtained. However, this method is limited by the size of the crystal block. Subsequently other types of

X-ray phase-contrast and dark-field imaging techniques were developed, including propagation based and grating-based X-ray phase contrast imaging [Morrison, 1992; Clauser, 1992; Davis, 1995; Ingal, 1995; Snigirev, 1995; Chapman, 1996; Wilkins, 1996; Momose, 2003; Zdora, 2018]. Whereas the propagation based imaging techniques require high coherent X-rays. Furthermore, in propagation based imaging, one is not able to retrieve the dark-field information of a sample. This limitations do not exist for grating-based X-ray imaging.

In grating-based phase contrast imaging the so-called modulation grating imprints a periodic phase- or intensity modulation onto the X-ray beam, which is converted to an intensity modulation further downstream, commonly by exploiting the Talbot effect. An analyser grating demodulates the pattern, as detector pixel sizes are typically not sufficient to detect the original pattern directly [Momose, 2003; Weitkamp, 2005]. Later on, the first grating-based phase-contrast imaging system with a conventional X-ray source was developed [Pfeiffer, 2006]. Here, a third grating is placed close to the source to achieve the needed spatial coherence of X-rays, exploiting the Lau effect. The disengagement of these Talbot-Lau interferometers from synchrotron research institutions lowered costs and increased accessibility of X-ray phase-contrast imaging. Furthermore, it was found that the reduction in interferometric visibility caused by certain samples could be interpreted as an additional imaging modality [Pfeiffer, 2008]: in analogy to light microscopy, the so-called dark-field represents the small-angle scatter induced by an object. This small-angle scattering occurs at interfaces of different materials in an object, whose microstructure is typically smaller than the resolution of the imaging setup. Thus, it is possible to retrieve information about the sub-pixel microstructure of the object. In subsequent studies this new image modality was applied in basic research, non-destructive testing and medical diagnostics [Yashiro, 2010; Lynch, 2011; Strobl, 2014; Prade, 2016; Bachche, 2017; Arboleda, 2019; Braig, 2020; De Marco, 2020]. Concerning the latter, first experiments showed that the lung is the organ in the body which generates the strongest dark-field signal due to the many air tissue interfaces of the alveoli [Bech, 2013].

Further studies performed on mice examined the effect of pulmonary diseases affecting the alveolar structure on the dark-field signal. Results from studies of mice with pulmonary emphysema showed that the change in dark-field signal was stronger than the change in transmission signal compared to signals from control mice, and that pulmonary emphysema can be detected in an earlier stage using dark-field images [Schleede, 2012; Yaroshenko, 2013; Meinel, 2014; Hellbach, 2015]. For pulmonary fibrosis a similar effect was found [Yaroshenko, 2015]. Furthermore, images of mice with pneumothoraxes showed a higher contrast to noise ratio in the dark-field than in attenuation modality. A reader study reported an improved diagnosis of pneumothoraces using dark-field images [Hellbach, 2016]. Another mice study showed that the detection of lung cancer can be improved with X-ray dark-field imaging [Scherer, 2017]. Furthermore, it was shown, that acute lung inflammation is visible in dark-field images [Hellbach, 2018b].

Another possible clinical application for grating-based X-ray dark-field and differential-phase-contrast imaging is bone imaging. It has been shown that differential phase contrast generates a better contrast in bone imaging especially around the cartilage [Tanaka, 2012;

Nagashima, 2013; Momose, 2014; Horn, 2017; Seifert, 2019]. In contrast to the lung, which scatters X-rays isotropically, long bones scatter X-rays stronger perpendicular to their long axis. As a Talbot-Lau-interferometer with one-dimensional grating lamellae are only sensitive to X-rays scattered perpendicular to the grating lamellae orientation, the scattering strength depending on the samples orientation can be measured. The used method is called X-ray vector radiography (XVR) and is able to obtain information about the microstructure of the sample, i.e. the local average scattering power, the asymmetry of the scattering and the preferred scattering direction [Jensen, 2010a]. Several studies have been performed to investigate the orientation of the micro-structure in the bone and to receive information about the stiffness and the failure load of bones [Jensen, 2010b; Potdevin, 2012; Schaff, 2014; Baum, 2015; Eggl, 2015; Jud, 2017].

Almost all these studies were performed with a rather small field of view. Translating grating-based X-ray imaging to larger field of views is not straightforward. The biggest challenge is overcoming the limited size of the gratings. Due to manufacturing difficulties, it has not yet been possible to fabricate gratings of the size of clinical detectors used for example for chest radiography. However, by applying a scanning method, the needed size of the gratings can be reduced. For image acquisition either the sample is moved while the interferometer is stationary [Kottler, 2007; Seifert, 2019] or the sample remains stationary while the interferometer is moved [Koehler, 2015; Gromann, 2017]. Studies conducted on setups with a larger field of view showed that it is possible to generate dark-field signal in larger samples like pigs and human cadavers as well [Gromann, 2017; Willer, 2018; Hauke, 2018; Ludwig, 2019]. Furthermore, it was revealed that, like in the mice studies, pneumothoraces are better detectable using dark-field imaging than transmission imaging [Hellbach, 2018a]. Another study on porcine thoraxes showed a linear correlation between lung thickness and dark-field signal. Moreover, the dark-field signal per lung thickness decreases with increasing ventilation pressure [De Marco, 2019]. Furthermore, reader studies with radiologists evaluated image quality and detectability of abnormalities in X-ray dark-field chest radiography [Fingerle, 2019]. Recently, first studies evaluating dose characteristics and the improved diagnosis of chronic obstructive pulmonary disease on humans were presented [Frank, 2021; Willer, 2021; Gassert, 2021].

Even though many research papers were published concerning X-ray dark-field imaging, there are still questions to be answered. Especially the translation from small animal models to human imaging is an ongoing task and optimal imaging parameters have not yet been examined in detail. Therefore, this thesis investigates in pre-clinical studies the optimal tube voltage for X-ray dark-field chest radiography and the dark-field signal in other regions of the human body. Furthermore, the translation of XVR and tomosynthesis to a large-field-of-view X-ray dark-field setup is demonstrated.

Outline

The theoretical background for this thesis is described in Chap. 2 – 4. Chap. 2 focuses on general fundamentals of X-ray physics, like X-ray generation, interaction of X-rays with

matter and dose calculations. The principles of grating-based X-ray dark-field and phase-contrast imaging is described in Chap. 3. Chap. 4 gives a description of the principles of three-dimensional X-ray imaging. The setup used for the experiments in this thesis is described in Chap. 5. The experimental study is the determination of the optimal tube voltage for X-ray dark-field chest imaging in Chap. 6. Next, in Chap. 7, whole-body X-ray dark-field radiographs of a human cadaver are examined. In Chap. 8, an acquisition method with an moving sample is implemented. With this method, XVR images obtained with a large field of view are presented in Chap. 9. Chap. 10 addresses the retrieval of three-dimensional information in X-ray dark-field imaging for large samples. In the end (Chap. 11) a summary of the most important conclusions of this thesis and an outlook for possible future studies is given.

2 Fundamentals of X-ray physics

2.1 The electromagnetic spectrum

X-rays are electromagnetic radiation, lying in the electromagnetic spectrum between the ultraviolet rays and the gamma rays (cf. Fig. 2.1). The distinction between X-rays and ultraviolet- or gamma-rays is not clearly defined. Depending on the source the X-ray regime starts somewhere in the low three-digit eV range. The difference between X-rays and gamma rays can be either defined by an energy where the X-ray regime ends and the gamma ray regime starts. This is mostly done in astronomy where the maximal X-ray energy/ lowest gamma ray energy is around 0.5 MeV. The other way to differentiate between X- and gamma-rays is the way they are generated. X-rays are produced when charged particles change the energy levels of atoms or are accelerated in an external field, while gamma-rays are produced by radioactive decays and annihilation of matter and anti-matter. Like other radiation in the electromagnetic spectrum, X-rays can be described as particles or as wave. The energy E of a photon is given by

$$E = h_p \nu = \frac{h_p c}{\lambda}, \quad (2.1)$$

where h_p is the Planck-constant, ν is the frequency of the radiation, c is the speed of light, and λ is the wavelength. [Gratton, 1970; Attwood, 1999; Biswas, 2000; Cerrito, 2017; Andreo, 2017]

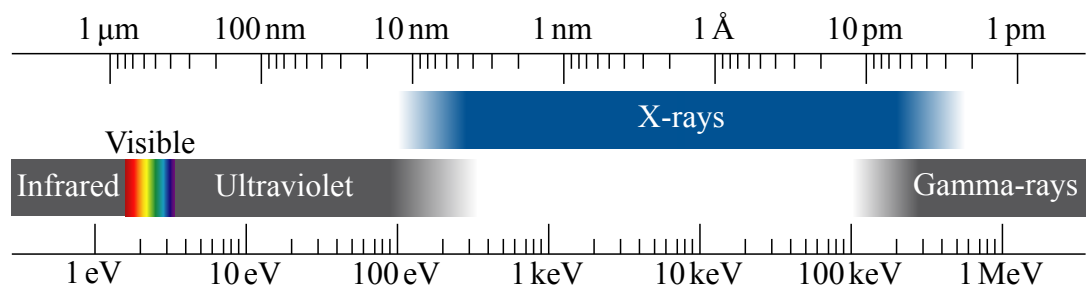


Figure 2.1: Electromagnetic spectrum from 1 eV to 1 MeV. The X-ray regime starts around 100 eV. Figure adapted from [Attwood, 1999; Cerrito, 2017].

2.2 X-ray sources

The first X-ray tubes were Crookes tubes. These were so called cold anode tubes where, if the pressure inside the tube is low enough and a voltage is applied between the cathode and the anode, current passes through the tube. If the pressure is further reduced, the electrons gain velocity and generate X-rays when hitting the anode. These tubes were mostly sealed off and it was not possible to adjust the vacuum inside the tube. Over time the ions combined with the anode material resulting in lower pressure. Thus, to still generate X-rays, the voltage had to be increased. Because of these vacuum changes inside the tube, they were instable. A further drawback was that the current and voltage could not be varied independently. In 1912 W. E. Coolidge overcame those difficulties. He used a tungsten spiral filament as cathode which emitted electrons due to thermal emission if a current is applied. Thus, an electron cloud accumulates around the anode. The higher the current of the cathode the more electrons are emitted. Then, those electrons are accelerated towards the anode by a high voltage applied between the cathode and the anode. Upon hitting the anode materials, X-rays are generated. The higher the applied voltage between the cathode and the anode is, the higher is the kinetic energy of the electrons and thus, the higher is the maximal possible energy of the X-rays. To reduce collisions of electrons (on their way to the anode) with gas molecules, which slow down the electrons, a high vacuum must be present inside the tube. As most of the electron energy is converted to heat the anode material has to be cooled to use the tubes at higher powers. This is usually done using a coolant fluid. A next important step in the development of X-ray tubes is the so-called rotating anode tube. A scheme of such a tube can be seen in Fig. 2.2 a). Here, the anode is a large disc which is hit by the electron beam off centre. The anode is rotated to distribute the heat over a larger area and thus it is possible to further increase the power of the tube. [vdPlaats, 1980; AlsNielsen, 2011; Dössel, 2016]

A typical X-ray spectrum generated by an X-ray tube is shown in Fig. 2.2 b). The broad part of the spectrum is the bremsstrahlung, which originates from decelerating electrons in the Coulomb-field of the atoms in the anode. The peaks originate from material characteristic fluorescence. Here, inner shell electrons of the atoms in the anode are kicked out of their shell by the impinging electrons from the cathode creating electron holes in this shell. Electrons from higher shells can relax into these holes and emit a photon with a specific energy i.e., the difference of the energy levels of the two shells. The maximal energy of the X-rays is limited by the acceleration voltage between cathode and anode. [AlsNielsen, 2011]

Other sources for X-rays are synchrotrons. Here, the so-called synchrotron radiation is emitted by accelerated relativistic electrons. Due to the relativistic Doppler-effect, the emitted radiation is mostly observed along the tangent of the electrons path. In a synchrotron, electrons, emitted from an electron gun, are accelerated in a linear accelerator and a booster ring. Then, these electrons are injected into the storage ring where the electrons are kept on a closed-loop path. It consists of a series of magnets (bending magnets and focusing magnets), insertion devices, generating the most intense synchrotron radiation, and radio frequency supplies to compensate for energy loss of the electrons due to the emission of synchrotron

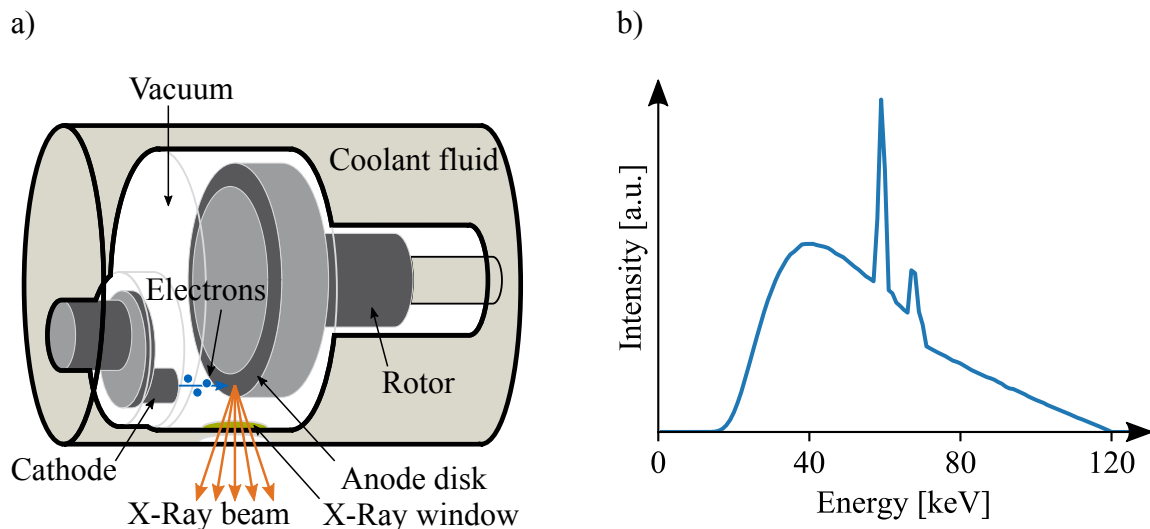


Figure 2.2: a) Schematic of an actively cooled rotating anode X-ray tube. In a vacuum chamber, the cathode emits electrons which are accelerated towards the anode disc. Upon hitting the anode material, X-rays are generated. To disperse the heat at the focal spot over a larger area, the Anode disc is rotated. b) Spectrum of an X-ray tube with tungsten as target material with 120 kV acceleration voltage pre-filtered with 3 mm aluminium. The broad part of the spectrum is the bremsstrahlung and the peaks correspond to the characteristic emission lines. Figure (a) adapted from [Behling, 2020].

radiation. Finally, the beamlines with the experimental hutches are placed tangentially to the storage ring at the bending magnets or along the axis of the insertion devices. The advantages of a synchrotron sources over laboratory sources include higher flux and monochromaticity, whereas the advantages of a laboratory sources are their relatively small size, lower purchase and maintenance costs, and greater accessibility. [Willmott, 2011]

The quality of an X-ray beam is described by the quantity ‘brilliance’. It takes into account the number of emitted photons per second, the beam divergence, the source spot size, and the spectral distribution. Synchrotrons have in general a high brilliance. X-ray tubes have in general a low brilliance as the spectral distribution is quite broad, the source spot size relatively large, and the beam divergence is relatively large. [Willmott, 2011]

The source spot size and spectral distribution are also important for the coherence of a X-ray source, which is particularly relevant in interference experiments. As these two properties are non-negligible for any real X-ray source, two wave emitted from this source will be out of phase at one point. The coherence can be measured in the coherence length, which is the distance when these two waves are out of phase. There are two different types of coherence: the longitudinal and transverse coherence lengths. Fig. 2.3 a) schematically illustrates the longitudinal coherence. Two plane waves A and B with slightly different wavelengths λ and $\lambda - \Delta\lambda$ propagate in the same direction. At point P they are in phase. As the waves have slightly different wavelengths, the phase difference between the two waves will change as

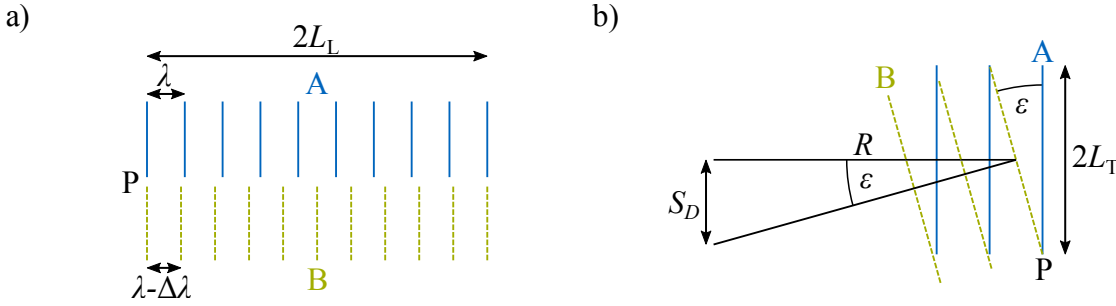


Figure 2.3: Schematic of longitudinal (a) and transverse (b) coherence. Longitudinal coherence is if two wave fronts (A and B), which are at a point P in phase, will be out of phase due to a slight difference in their respective wavelengths after L_L . If two wave fronts (A and B) have a slightly different propagation direction (i.e., because they originate from a source with size D at distance R) they are in phase in point P but will be out of phase in perpendicular direction from the propagation direction. Figure adapted from [AlsNielsen, 2011].

they propagate. The longitudinal coherence length L_L is defined as the distance in propagation direction until they are out of phase and thus $2L_L$ is the length when the two wave-fronts are again in phase. The longitudinal coherence length is given by [AlsNielsen, 2011]

$$L_L = \frac{1}{2} \frac{\lambda^2}{\Delta\lambda}. \quad (2.2)$$

A schematic to illustrate transverse coherence can be seen in Fig. 2.3 b). Two waves with the same wavelength λ but slightly different propagation direction by an angle $\Delta\theta$ are in phase at point P. Those two wave-fronts may for example originate from a source with size S_D at a distance R . As the propagation direction of the two waves is slightly different, both waves superimpose at different points along the wavefront with different relative phases. The transverse coherence length L_T is defined as the distance along wave-front A until both wave-fronts are out of phase. Thus, $2L_T$ is the distance until both wave-fronts are in phase again. The transverse coherence length is given by [AlsNielsen, 2011]

$$L_T = \frac{1}{2} \frac{\lambda}{(S_D/R)} = \frac{\lambda}{2} \left(\frac{R}{S_D} \right). \quad (2.3)$$

2.3 X-ray interaction with matter

When X-ray hit an object, several interaction can occur in the matter. These interactions lead to the effect of attenuating, scattering and phase-shift of the incoming X-ray wave. The probability for the different interaction depends on the X-ray energy. In the following the most important X-ray interactions with matter for the clinical X-ray imaging regime will be described.

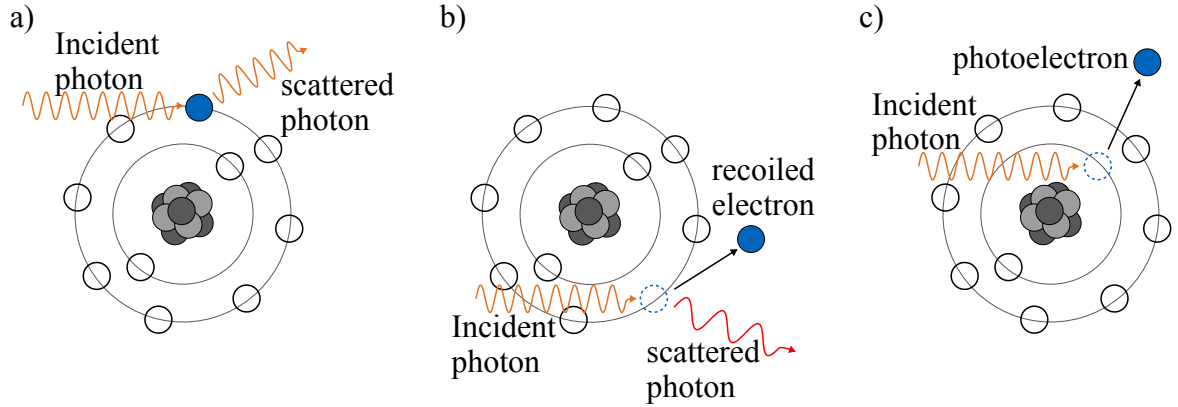


Figure 2.4: The three main interactions with matter which are important for bio medical imaging. a) In case of coherent scattering, the energy of the X-rays and of the electron, with which the photon interacts, remain unchanged. Only the propagation direction of the X-rays changes. b) An electron is emitted from the atom during incoherent scattering. As this requires energy the energy of the X-ray is lower after the scattering process. Furthermore, the propagation direction of the photon changes. c) In photoelectric absorption the complete energy of an X-ray photon is transferred to an electron of the atom, which is then ejected. Figure adapted from [Seibert, 2005].

2.3.1 Atomic level interaction

Fig. 2.4 shows the three main interactions of X-rays with matter relevant for bio-medical imaging, namely coherent scattering, incoherent scattering, and the photoelectric effect. These effects will be discussed in the following. Beside these interaction there are amongst others also pair production or interactions with the atom core, but as these are more prominent for higher energies and are thus not relevant for this thesis, they are not further discussed. Mathematically the interaction of X-rays with matter on the atomic level can be described by the atomic cross section, which is a measure of the probability that a specific interaction will occur. The total atomic cross section σ_{tot} is given by the sum over the atomic cross section of the single interactions

$$\sigma_{\text{tot}} = \sigma_{\text{coh}} + \sigma_{\text{incoh}} + \sigma_{\text{ph}}, \quad (2.4)$$

where σ_{coh} , σ_{incoh} , and σ_{ph} are the cross section of the coherent scattering, incoherent scattering and the photoelectric effect respectively [Willmott, 2011].

Coherent scattering

In coherent scattering, the electromagnetic field of the incident X-rays cause an electron to oscillate. The induced dipole oscillation is the reason for the re-emission of an electromagnetic wave. The energy and wavelength of the incoming wave does not change during the scattering process. Also, the electron state before and after scattering process stays the same.

Only the direction of propagation of the wave is different after the scattering process. The electronic cross section of coherent scattering can be calculated by using the definition of the scattering cross section and solving the equation of motion for the electron. The result is:

$$\sigma_{\text{e,coh}} = \frac{8\pi}{3} r_e^2 \frac{\omega^4}{(\omega^2 - \omega_r^2)^2 + (\gamma\omega)^2}, \quad (2.5)$$

with r_e the electron radius, ω the angular frequency of the wave, ω_r the angular resonance frequency of the electron, and γ is a result of the dissipative force term (it can be assumed $\frac{\gamma}{\omega} \ll 1$ [Attwood, 1999; Buzug, 2008]). Far from the resonance frequency of the electron, two cases can be distinguished: The first case, where $\omega^2 \ll \omega_r^2$ and $\gamma \ll \omega$, is the case of a tightly bound electron. Eq. (2.5) changes to

$$\sigma_{\text{e,R}} = \frac{8\pi}{3} r_e^2 \left(\frac{\omega}{\omega_r} \right)^4 \quad (2.6)$$

and is called electronic Rayleigh cross section. It was first described by Lord Rayleigh in 1899. The atomic Rayleigh cross section is approximately

$$\sigma_{\text{R}} \propto \frac{Z^2}{E^2} \quad (2.7)$$

with Z the atomic number [Attwood, 1999; Podgorsak, 2016]. The second case with $\omega^2 \gg \omega_r^2$ is the case of a loosely or quasi free electron and is called Thomson scattering. Eq. (2.5) changes to the electronic Thomson cross section

$$\sigma_{\text{e,Th}} = \frac{8\pi}{3} r_e^2 \quad (2.8)$$

and is independent of the energy [Attwood, 1999]. The atomic Thomson cross section is given by

$$\sigma_{\text{Th}} = Z\sigma_{\text{e,Th}}. \quad (2.9)$$

Incoherent scattering

Incoherent scattering is based on the Compton effect (cf. Fig. 2.4 b)). An incident photon with energy $h\nu$ (cf. Eq. (2.1)) interacts with a loosely bound electron, whose binding energy E_b is lower than the energy of the photon. During the scattering this (recoil) electron is ejected from the atom with a kinetic energy E_k . After the process, the wavelength λ_s of the scattered photon is lower than the wavelength λ_i of the incident photon. Furthermore, the direction of propagation of the scattered photon differs from the incident photon by the angle ϵ . The shift of the wavelength is given by

$$\Delta\lambda = \lambda_s - \lambda_i = \frac{h_p}{m_e c^2} (1 - \cos\epsilon) \quad (2.10)$$

For cross section for incoherent scattering can be approximated with the help of the Klein-Nishina formula which decreases with energy and

$$\sigma_{\text{incoh}}^{\text{KN}} \propto Z. \quad (2.11)$$

For lower energies (i.e. $E \rightarrow 0$) $\sigma_{\text{incoh}}^{\text{KN}}$ approximates σ_{Th} (cf. Eq. (2.9)). However, the actual incoherent scattering cross section decreases with the energy. Therefore, the Klein-Nishina approximation does not hold any more. [Attwood, 1999; Willmott, 2011; Podgorsak, 2016]

Photoelectric absorption

When a photon transfers its complete energy to an electron of the atom, it is called photoelectric absorption (cf. Fig. 2.4 c)). Therefore, the energy of the photon has to be larger than the binding energy of the electron. Afterwards, the (photo) electron has a kinetic energy E_k of the difference between the incident photon energy $h_p\nu$ and the binding energy E_b : $E_k = h_p\nu - E_b$. After the electron ejection, the vacant place in the shell can be filled with an electron from one of the outer shells. Either a photon will be emitted with the energy of the difference of the two shells (X-ray fluorescence) or an so called auger electron from the outer shell is emitted. Here, the binding energy of the electron is smaller than the excess energy remaining in the atom. The atomic cross section for the photoelectric effect is

$$\sigma_{\text{ph}} \propto \frac{Z^{4-5}}{E^3} \quad (2.12)$$

away from the absorption edges. [AlsNielsen, 2011; Podgorsak, 2016]

Atomic scattering factor

Related to the cross section and another way to express the interactions mathematically is the atomic scattering factor f (also called atomic form factor). It describes the total scattering amplitude of a atom as a function of the scattering vector \vec{Q} :

$$f(\vec{Q}) = \int \rho(\vec{r}) e^{i\vec{Q} \cdot \vec{r}} d\vec{r}, \quad (2.13)$$

with the electron number density ρ , \vec{r} the position vector, and i the imaginary unit. As the electron, at which the X-ray scatters, is normally bound to an atom, correction terms have to be added to the atomic scattering factor. The first correction term results from the damping of the oscillation in which the electron is forced by the X-ray wave. This reduces the real part of the scattering factor by the additional term f' . Close to the absorption edges in forward scattering the second correction term f'' is related to the cross section of the photoelectric effect by

$$f''(0) = \frac{\sigma_{\text{ph}}}{2r_e\lambda}. \quad (2.14)$$

As Eq. (2.13) is a complex function, the total atomic scattering factor can also be written as [AlsNielsen, 2011]

$$f_{\text{tot}} = f_1 + if_2 = f - f' + if'' . \quad (2.15)$$

2.3.2 Wave function and complex refractive index

A way to describe the interaction on macroscopic level is the complex refractive index n . It is related to the complex scattering factor via

$$n = 1 - \frac{r_e}{2\pi} \lambda^2 \sum_i N_i f_{\text{tot},i}(0), \quad (2.16)$$

where N_i is the number of atoms of type i per unit volume and $f_i(0)$ is the complex scattering factor in the forward direction of the i -th atom. Since f_{tot} is a complex number Eq. (2.16) can also be written as:

$$n = 1 - \delta + i\beta. \quad (2.17)$$

Here, δ is called the refractive index decrement and β the absorption index. To understand their effect, we will look at a X-ray wave propagation through space. For simplicity reasons only monochromatic plane waves moving in z -direction will be considered. Its wave function after time t at position z in vacuum is given by:

$$\Psi(z, t) = \Psi_0 \cdot e^{i(k_0 z - \omega t)}, \quad (2.18)$$

where Ψ_0 is the amplitude of the wave, $k_0 = 2\pi/\lambda_0$ the length of the wave vector in z -direction and $\omega = 2\pi c/\lambda_0$ the angular frequency. The complex refractive index n is connected to the wave vector via $\vec{k} = n\vec{k}_0$, where \vec{k}_0 is the wave vector in vacuum. So, Eq. (2.18) changes for a wave in material to:

$$\Psi(z, t) = \Psi_0 \cdot e^{i(kz - \omega t)} = \Psi_0 \cdot e^{i(nk_0 z - \omega t)}. \quad (2.19)$$

Inserting Eq. (2.17) in this equation leads to:

$$\Psi(z, t) = \underbrace{\Psi_0 \cdot e^{i(k_0 z - \omega t)}}_{\text{vacuum propagation}} \cdot \underbrace{e^{-i\delta k_0 z}}_{\text{phase-shift}} \cdot \underbrace{e^{-\beta k_0 z}}_{\text{decay}}. \quad (2.20)$$

Here, the second term on the right ($e^{-i\delta k_0 z}$) describes the phase-shift of the wave due to the material and the last term ($e^{-\beta k_0 z}$) describes the decay of the waves amplitude in the material. Both effects will be discussed in the following in more detail. [AlsNielsen, 2011; Willmott, 2011]

2.3.3 Attenuation

The last term in Eq. (2.20) expresses the decay of the wave when travelling through a material. As illustrated in Fig. 2.5 the amplitude of the wave declines while the wave passes through an object. How strong the wave declines depends on the absorption index β .

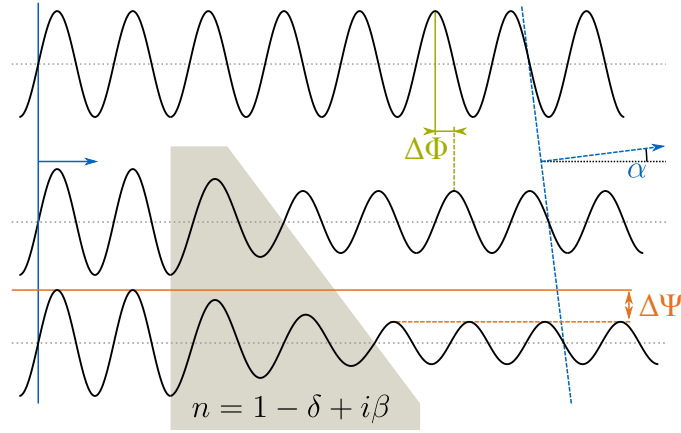


Figure 2.5: Attenuation and phase-shift of a wave in an object. The amplitude of the wave decays while travelling through the object. Also, the wavelength of the wave changes which leads to a phase-shift of a wave travelling through a object compared to one propagating in free space.

By comparing the complex parts of Eq. (2.16), Eq. (2.17), and Eq. (2.15) the connection between the absorption coefficient and the atomic scattering function can be determined to

$$\beta = \frac{r_0}{2\pi} \rho_a \lambda^2 f'', \quad (2.21)$$

with ρ_a the atomic number density. The intensity $I(z)$ of the X-rays behind an object of thickness z is given by the square of the absolute value of the wave function $\Psi(z, t)$:

$$I(z) = |\Psi(z, t)|^2 = \Psi_0^2 \cdot e^{-2\beta k_0 z} = I_0 \cdot e^{-2\beta k_0 z} = I_0 \cdot e^{-\mu z}, \quad (2.22)$$

with I_0 the intensity of the incoming wave and $\mu = \rho_a \sigma_{ph} = 2\beta k_0$ the absorption coefficient. Note, that $I(z)$ is not dependent on time anymore. This equality is also called Beer-Lambert law. Normally, the intensity behind an object is not of interest but rather the fraction of transmitted radiation T of the object. It is given by

$$T(E) = \frac{I(E)}{I_0(E)} \quad (2.23)$$

and depends on the X-ray energy. [Attwood, 1999; Willmott, 2011; AlsNielsen, 2011]

2.3.4 Phase-shift

Fig. 2.5 also depicts the effect of phase-shift. The wavelength in the object (grey shape) is increased compared to the vacuum wavelength. Thus, the phase of the wave travelling through an object (green dashed line) is shifted with respect to a wave propagating in vacuum (green solid line). This is described by the second term on the right of Eq. (2.20), where the exponents equal the phase-shift

$$\Delta\Phi = \delta k_0 z = \delta \frac{2\pi}{\lambda} z \quad (2.24)$$

of the wave when propagating through a material of thickness z compared to an undisturbed wave [Attwood, 1999].

Comparing the real part of Eq. (2.16) and Eq. (2.17) reveals the relation between the refractive index decrement and the atomic scattering factor. Far from the absorption edges, the sum $\sum_i N_i(f - f')_i(0) = \rho_e$ is the average density of electrons and therefore [Willmott, 2011]

$$\delta = \frac{\rho_e r_e \lambda^2}{2\pi}. \quad (2.25)$$

Usually, δ is in the order of 10^{-6} . As a consequence, the real part of n is little less than one for X-rays. This means that X-rays behave in some aspect different than visible light, where the refractive index is larger than one. E.g., in contrast to visible light, for X-rays the wavelength in a medium is larger than in vacuum and if entering from vacuum into a medium the X-rays will be refracted towards the normal of the interface layer.

If the object in the beam path is a wedge, an incoming plane wave is refracted after the object. The propagation direction of the outgoing plane wave is shifted by the angle α compared to the propagation direction of the incoming wave. For small phase gradients the refraction angle can be approximated to [Davis, 1995]

$$\alpha \approx \frac{1}{k} \frac{\partial \Phi(x)}{\partial x}. \quad (2.26)$$

If the object in the beam path is not a wedge but rather a porous material, every interface can be seen as a small wedge, so the X-ray beam experiences many phase-shifts with every partial wave refracted differently. Macroscopic, this can be described as scattering of the X-ray beam.

2.4 X-ray imaging

Image geometry

As conventional X-ray sources have an extended source spot and have a large divergence angle geometrical effects need to be considered when acquiring X-ray images. In a first approximation, the focal spot of the X-ray source can be assumed to be a point source with a diverging X-ray beam. Thus, objects are magnified on the detector or image plan. The magnification factor M can be calculated by

$$M = \frac{\overline{SD}}{\overline{SO}}, \quad (2.27)$$

where \overline{SD} is the source-detector-distance, and \overline{SO} is the source-object-distance. Fig. 2.6 shows the magnification of two objects (O_1 and O_2) of the same size and same source-detector-distance. The object O_1 is closer to the source and thus its image I_1 appears larger than the image I_2 of object O_2 . [Seibert, 2005]

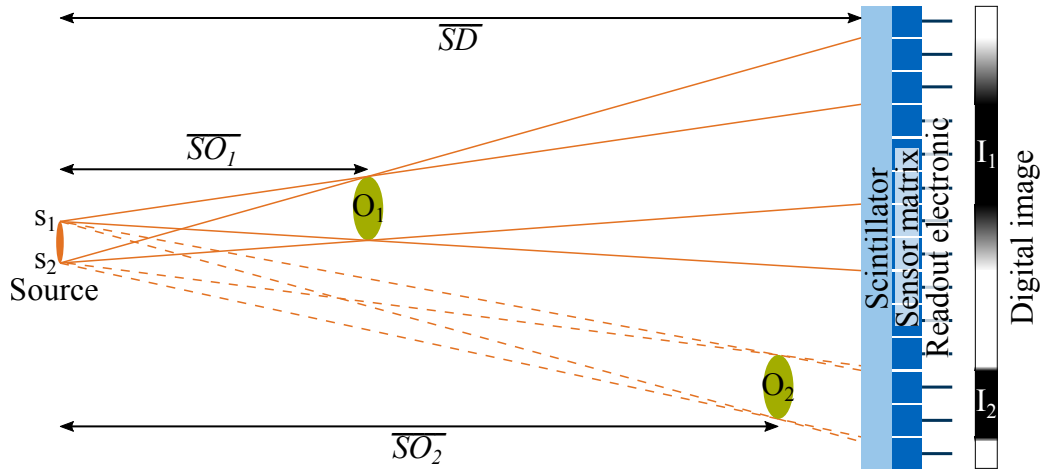


Figure 2.6: Image geometry and flat panel detector. O_1 and O_2 denote two objects in the beam path, while I_1 and I_2 label their corresponding images on the detector. The source can also be considered as several point sources (s_1 and s_2). Important distances for image geometry are the source-detector-distance (\overline{SD}) and the source-object-distance ($\overline{SO_1}$ and $\overline{SO_2}$). Image magnifications originate from the fact, that the X-ray beam is diverging. Thus, an object closer to the source is projected to a larger image than an object closer to the detector. Due to the extended source size the image of the object is blurred. Here again the effect is stronger, the closer the object is placed to the source. In blue on the right is a schematic of a flat panel detector shown. The X-rays are converted to visible light in a scintillator layer and converted to an electric signal in the sensor matrix.

In reality, the focal spot is not a point source but has a finite size. It can be viewed as an array of point sources, each emitting their own X-ray cone. As a result, the image of the object is blurred at its edges and a loss of resolution happens before the X-rays are detected. This effect can be seen in Fig. 2.6. From the edges of the source at point s_1 and s_2 rays travel to the upper corner of e.g. object O_1 . The X-rays reach the detector at different points, which results in blurred edges of the image I_1 . The closer the object is to the detector, the smaller is this geometrical blur as it can be seen by comparing the images I_1 and I_2 , where the edge gradient of I_2 is smaller as O_2 is closer to the detector.

Indirect conversion detectors

One of the first ways to detect X-rays were X-ray films. The film is covered with silver halide crystals. When illuminated with X-rays, silver ions are reduced, and silver crystals are formed. Excess silver halide crystals are removed and a blackening due to the silver crystals remain on the film, where it was exposed.

Nowadays, mostly flat panel detectors are used in radiography. A rough schematic of such detector is shown on the right and side of Fig. 2.6. It consists of a scintillator layer, often

CsI, which converts X-rays into visible light. The thinner the layer is the better is the spatial resolution, but the thicker the layer is the better is the quantum efficiency. Thus, a trade-off between spatial resolution and quantum efficiency has to be found. A sensor matrix is placed behind the scintillator layer. Consisting of amorphous silicon, it converts the visible light into an electrical signal. Around the sensor matrix is the readout and control electronics located. [Bille, 2002; Seibert, 2005; Dössel, 2016]

2.5 Dose calculations

Exposing material to ionising radiation like X-rays can lead to radiation damage. The severity of the radiation damage depends, among other things, on the dose deposited in the material. In biological material radiation exposure can lead to the death or malfunction of the cells, which can lead to diseases like cancer. Therefore, the applied dose is kept as low as possible for clinical imaging. The absorbed dose (AD) is the mean energy transferred to matter per mass and has the unit Gray (Gy). For indirect ionising radiation, like photon and neutron radiation, this transfer occurs in two steps. First the radiation releases charged particle (mainly electrons) inside the matter and transfers kinetic energy to the charged particles. This process is also described by the *KERMA* (kinetic energy released in matter). Then, the charged particles transfer kinetic energy to the material as they travel through it. Multiplying the absorbed dose AD with the exposed area a lead to the dose area product DAP:

$$DAP = AD \cdot a. \quad (2.28)$$

As different types of radiation have different effects on biological matter the equivalent dose (EqD) is introduced which takes the type of radiation into consideration:

$$EqD = w_r \cdot AD, \quad (2.29)$$

with w_r the radiation weighting factor (for X-rays: $w_r = 1$). The unit of the equivalent dose is Sv, to avoid confusing the equivalent dose with the absorbed dose. As some organs are more prone for radiation damage the effective dose (ED) also takes into account the organ which is exposed to ionising radiation and can be calculated with

$$ED = w_t \cdot EqD, \quad (2.30)$$

where w_t is the tissue weighting factor. As it is not straightforward to measure the absorbed dose, Wall et al. [Wall, 2011] listed conversion factors w_w for X-ray radiography to calculate the ED directly from the DAP [Wall, 2011]:

$$ED = w_w \cdot DAP. \quad (2.31)$$

3 Grating-based X-ray imaging

Besides the X-ray attenuation, which is measured by conventional X-ray imaging, wave-optical effects such as refraction and small-angle scatter of X-rays occur on interaction with matter. Grating-based X-ray imaging employs interferometric effects to detect phase-shifts and scattering of the X-rays induced by an object. Besides the attenuation and differential-phase signal also the dark-field signal can be retrieved with this method. The dark-field signal correlates to small angle scatter of X-rays on an object. As grating-based imaging requires a high transverse coherence of the X-ray source, the first experiments were performed at synchrotrons. Further developments made it possible to use conventional X-ray tubes.

3.1 Talbot effect

A grating interferometer is based on an effect discovered by Henry Talbot in 1836. Talbot placed a periodic structure in the beam path of visible light and observed, that after certain propagation distances behind the grating, so called Talbot distances, a self-image of the grating was created. He also noted, that the light source should have a "very small apparent diameter" [Talbot, 1836]. With other words, this effect can only be seen if the source emits rays with sufficient transverse coherence. [Talbot, 1836]

The Talbot distance depends only on the period p_1 of the grating and the wavelength of the light and can be calculated by

$$d_T = \frac{2p_1^2}{\lambda}. \quad (3.1)$$

Fig. 3.1 shows the interference pattern of a monochromatic Source behind an absorption grating, a π phase-shifting grating, and a $\pi/2$ phase-shifting grating. Also, for other distances than the Talbot distances an interference pattern with a high resemblance to the original wave front can be observed. In contrast to the Talbot distance, the periodicity of these patterns also depends on the shape of the grating. Taking a closer look at the interference patterns, it is visible that in Fig. 3.1 a) the period of the interference pattern parallel to the absorption grating corresponds to the period of the grating. Furthermore, maximal intensity contrast can be found at fractional Talbot distances of $0 \cdot d_T$, $\frac{1}{2}d_T$, and $1d_T$. Similar to the absorption grating, the $\pi/2$ phase-shifting grating generates an interference pattern, where the period of the intensity modulation parallel to the grating corresponds to the period of the grating. Maximal intensity contrast can be found at $\frac{1}{4}d_T$, and $\frac{3}{4}d_T$. For the π phase-shifting grating in Fig. 3.1 b) high intensity contrast are visible at more fractional Talbot distances, namely at

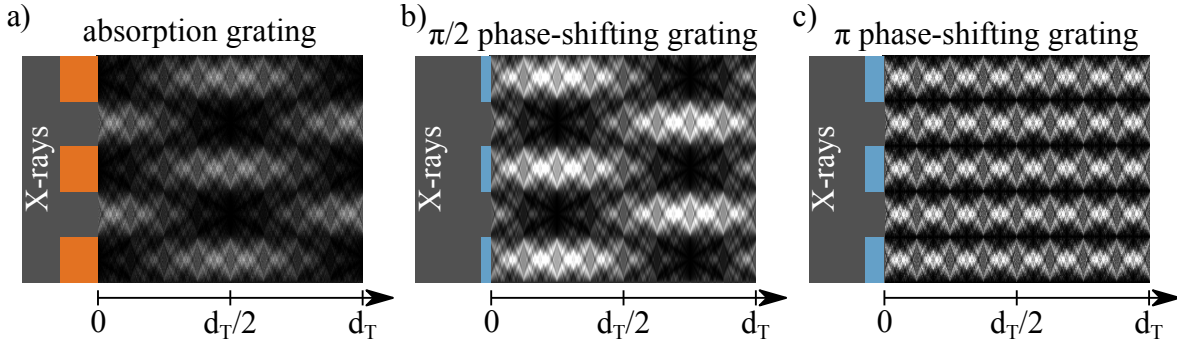


Figure 3.1: Talbot carpet of an absorption grating (a), a $\pi/2$ phase-shifting (b), and a π phase-shifting (c) grating. Depicted is the carpet for the full Talbot distance d_T , where the wave front repeats itself. At other distances an interference pattern with high resemblance to the one directly behind the grating is observable. Figure adapted from [Weitkamp, 2006].

$\frac{n}{16}d_T$ with n being an odd integer. Here, the period of the interference pattern parallel to the grating is half the period of the grating. [Weitkamp, 2006]

3.2 Talbot-Lau interferometer for incoherent sources

Grating based X-ray imaging exploits the Talbot effect by analysing changes of the interference pattern when a sample is placed in the beam path [Momose, 2003]. The period of the interference pattern is normally in the range of a few micrometre. As most detectors are not able to resolve the interference pattern directly an absorption grating is placed in front of the detector. To be able to use conventional laboratory sources, the Lau effect is exploited by placing a third grating in front of the source.

3.2.1 Reference grating

The grating imprinting a phase modulation to the X-ray wave front and thus creating the interference pattern is usually called reference grating or G_1 . Fig. 3.2 shows how this interference pattern is distorted when a sample (in green) is placed in the beam path. In orange the undisturbed interference pattern is shown and in blue the interference pattern modified by the sample. A purely attenuating object reduces the intensity of the pattern modulation (cf. Fig. 3.2 a)) but the phase of the pattern remains unchanged. If a phase wedge is placed in the beam path, the pattern will experience a phase-shift but amplitude and mean of the interference pattern do not change (cf. Fig. 3.2 b)). An object with many material interfaces scatters the X-rays. As a consequence, the amplitude of the interference pattern will be reduced due

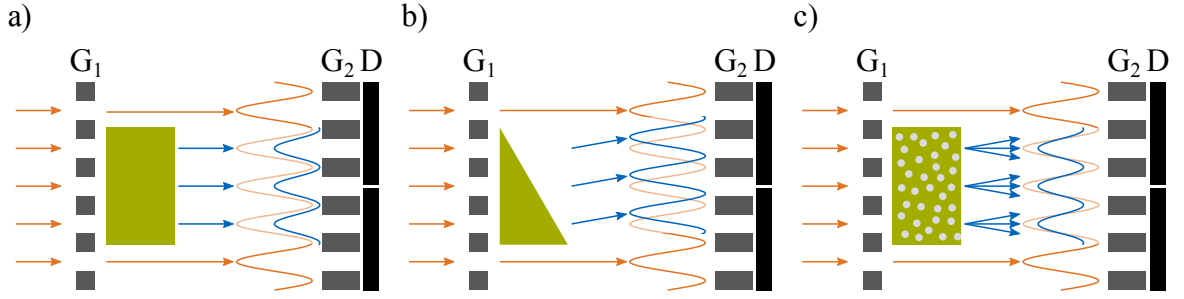


Figure 3.2: Effects of a sample (green shape) on the interference pattern in grating-based X-ray imaging. A purely attenuating object will reduce the mean of the interference pattern (a), while a purely phase-shifting object will shift the interference pattern parallel to the gratings (b). A scattering object reduces the amplitude but not the mean of the interference pattern (c). Figure adapted from [Jud, 2018].

to the object (cf. Fig.3.2c)). However, a real sample is not purely attenuating, phase-shifting or scattering, but a combination of these three effects. Thus, the amplitude, phase and mean of the interference pattern changes when a sample is placed in the beam path.

3.2.2 Analyser grating

As it can be seen in Fig. 3.1 the modulation period of the X-ray wave front is in the order of the grating period. The grating period of G_1 and thus the intensity modulation period is several micrometre up to some tens of micrometre assuming an laboratory setup with an X-ray energy of a few tens of keV and an fist fractional Talbot distance of 1 m. However, most conventional X-ray detectors have a pixel size around $100\text{ }\mu\text{m}$. Therefore, they are not able to resolve the intensity pattern directly. To overcome this limitation an absorbing grating, the so called analyser grating G_2 with a period that matches the interference pattern, is place right in front of the detector. By moving the grating over one period the interference pattern can be sampled (phase-stepping). The period of G_2 is directly proportional to the period of G_1 :

$$p_2 = M \frac{p_1}{m}, \quad (3.2)$$

where m is a factor depending on the grating type. For an absorption or a $\pi/2$ phase-shifting grating m equals one and for a π phase-shifting grating m equals 2 [Prade, 2017]. M is the magnification factor as defined in Eq. (2.27). Here, the source image distance \overline{SI} is between the source and G_2 and the source object distance \overline{SO} between the source and G_1 .

3.2.3 Source grating

As mentioned before, the Talbot effect requires sources with sufficient transverse coherence to observe the self-images of a grating. Synchrotron sources provide the required transverse

coherence as their source size is relatively small and the distance to the source is large compared to the interferometer length. However, the spot size of conventional laboratory sources is too large to provide enough coherence for the Talbot effect to be visible. Thus, a further effect is exploited to be able to use those sources in a Talbot-Lau interferometer. In 1948 Ernst Lau reported on his experiments with double grids. He placed two identical grids in a certain distance and observed a streak pattern, where all streaks have the same brightness. The two gratings were placed in such manner, that the path difference of rays from the same slit of the first grating, reaching two neighbouring slits of the second grating is equal to the wavelength of the rays. Thus, the rays shortly before the second grating are coherent [Lau, 1948; Clauser, 1992]. This effect is used in Talbot-Lau interferometry by placing a third grating, the so called 'source grating' or G_0 right in front of the source. This grating has to be an absorption grating to allow only narrow slits of X-rays to pass through. Thus, a slit of the grating acts as a line source. This single line source emits coherent enough rays to see the Talbot effect after the reference grating. The distance between slits has to be chosen in such a way that the self-images of G_1 created from the individual slits superimpose constructively in the G_2 plane. This is satisfied if the period of the source grating p_0 is given by

$$p_0 = p_2 \frac{l}{d}, \quad (3.3)$$

where l is the distance between the G_0 and G_1 and d the distance between G_1 and G_2 [Pfeiffer, 2006].

3.2.4 Visibility and angular sensitivity

A measure for the quality of the used gratings and how well they are aligned is the visibility. It is defined as

$$V \equiv \frac{I_{\max} - I_{\min}}{I_{\max} + I_{\min}}, \quad (3.4)$$

where I_{\min} and I_{\max} are the minimal and maximal intensities of the intensity modulation [Pfeiffer, 2008]. A measure for the scattering strength of a sample is obtained by comparing undisturbed and reduced visibility due to the sample. Normally a visibility of about 30 % is achieved in laboratory Talbot-Lau interferometer. Another important quantity of a Talbot-Lau interferometer is the angular sensitivity, which is a measure for the image signal dependent on the refractive angle of an object. It is defined as

$$S \equiv \frac{1}{2\pi} \frac{\Delta\varphi}{\alpha}, \quad (3.5)$$

with α the refractive angle and $\Delta\varphi$ the shift of the intensity modulation in a pixel due to the object. The higher the angular sensitivity the better is the detectability of the signal of objects with small refractive angles or of weak scattering objects. The angular sensitivity is dependent on the inter grating distances of the setup, the periods of the gratings, and the

position of the object within the setup. The angular sensitivity can also be expressed as

$$S = \left(\frac{1}{l} + \frac{1}{d} \right)^{-1} \frac{m}{p_1} \cdot \tilde{S}(\overline{OG_1}) \quad (3.6)$$

with the function

$$\tilde{S}(\overline{OG_1}) = \begin{cases} 1 - \frac{\overline{OG_1}}{l} & \text{if sample between } G_0 \text{ and } G_1 \\ 1 - \frac{\overline{OG_1}}{d} & \text{if sample between } G_1 \text{ and } G_2, \end{cases} \quad (3.7)$$

where $\overline{OG_1}$ is the distance between sample and G_1 . As it can be seen, the maximal angular sensitivity of a setup can be obtained for $\tilde{S}(\overline{OG_1}) = 1$, meaning at the G_1 . [Donath, 2009]

3.3 Signal extraction

To retrieve information about the attenuating, phase-shifting and scattering properties of the sample, the change of the interference pattern caused by the sample has to be determined e.g., by a phase-stepping or a moiré fringe scanning.

3.3.1 Phase-stepping

To obtain information on the attenuating, phase-shifting and scattering properties of a sample without a loss of information, one grating is moved perpendicular to the grating lines (cf. Fig. 3.3 a)). Thus, a (stepping) curve is recorded, representing the interference pattern. The shape of the stepping curve depends on the X-ray source, and the number and shape of the gratings. Mathematically the shape of the stepping curve is determined by convolutions of the grating's transmittance patterns and the source intensity distribution. Note, if a source grating is used, mathematically, its transmittance pattern replaces the source intensity distribution. Hence, three rectangular functions are convolved in case of three grating interferometer. This results in an intensity modulation which can be approximated by a sinusoidal function. Hence, the stepping curve can be approximated with a sinusoidal function depending on the step index η of the form

$$I_\eta = \tilde{A} \cdot \left[1 + V \cdot \cos(\phi_\eta + \varphi) \right], \quad (3.8)$$

with mean intensity \tilde{A} of the stepping curve, V the visibility, φ the phase of the stepping curve resulting from misalignment or initial relative grating position as well as objects in the beam path [Malecki, 2015]. For an equidistant stepping of H steps over one grating period the shift of the stepped grating can be calculated with $\phi_\eta = \eta \cdot \frac{2\pi}{H}$. This stepping curve is measured in every pixel over the field of view and might be different for each pixel, depending on the initial spatial intensity variation, and initial relative grating positions. To

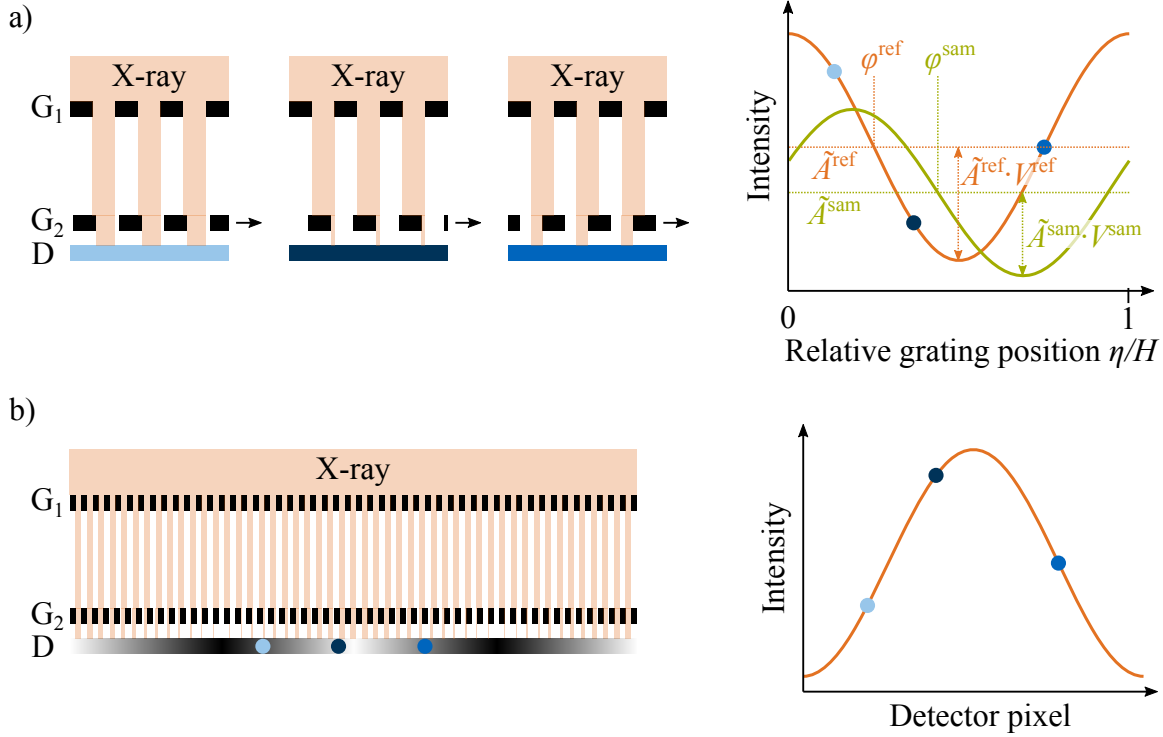


Figure 3.3: Schematic of the signal extraction. In the phase-stepping method (a) the intensity pattern is sampled by the movement of one of the gratings. Thus, a stepping curve as introduced in Eq. (3.8) is acquired. For the moiré fringe scanning approach (b) a mismatch of the gratings is introduced, resulting in a low frequency intensity modulation corresponding to the different relative grating positions.

retrieve image information from a Talbot(-Lau) interferometer the stepping curve has to be obtained once from a reference measurement without the sample (in the following indicated with the superscript ‘ref’), and once with the sample (in the following indicated with the superscript ‘sam’). The three modalities obtained by X-ray phase-contrast and dark-field imaging are the transmission

$$T = \frac{\tilde{A}^{\text{sam}}}{\tilde{A}^{\text{ref}}}, \quad (3.9)$$

the differential phase-shift

$$\Delta\varphi = \varphi^{\text{sam}} - \varphi^{\text{ref}}, \quad (3.10)$$

and the visibility reduction

$$\mathfrak{D} = \frac{V^{\text{sam}}}{V^{\text{ref}}}. \quad (3.11)$$

Note, that the transmission T is the same as it would be obtained from conventional radiography, also given in Eq. (2.23). Furthermore, the differential phase-shift of the intensity pattern is not the same as the phase-shift explained in section Sec. 2.3.4. The differential phase-shift $\Delta\varphi$ is related to the shift s of the intensity pattern by a sample in one pixel by [Willner, 2016]

$$s = \frac{p_2}{2\pi} \Delta\varphi \approx \alpha \cdot d. \quad (3.12)$$

In the clinics, images are often presented in the negative logarithmic form. The attenuation signal can be calculated by

$$A = -\ln T = -\ln \frac{\tilde{A}^{\text{sam}}}{\tilde{A}^{\text{ref}}}, \quad (3.13)$$

and dark-field signal by

$$D = -\ln \mathfrak{D} = -\ln \frac{V^{\text{sam}}}{V^{\text{ref}}}. \quad (3.14)$$

3.3.2 Moiré fringe scanning

An other method to retrieve the three modalities is based on the moiré effect. Here, due to a slight misalignment of G_1 and G_2 an intensity fringe pattern with a lower spatial frequency (moiré pattern) is visible at the detector. The misalignment can be achieved by either rotating one grating around the optical axis or by a slight mismatch of the grating periods. This is illustrated in Fig. 3.3 b) on the left side. In cone beam geometry this period mismatch can be achieved by shifting one grating along the optical axis and thus the projected period of both gratings are not identical anymore [Chabior, 2011]. Here, the period of G_2 is slightly smaller than the period of G_1 and at the detector a low frequency moiré fringe pattern is visibly. As the pattern is created by varying sampling of the intensity pattern a curve equivalent to a stepping curve can be obtained by observing at neighbouring pixels (cf. Fig. 3.3) if the pattern is sufficient regular. Placing an object in the beam path, the fringe pattern will be distorted. By moving the fringe pattern over the sample (e.g., by shifting the sample perpendicular to the pattern) different phases of the fringe pattern will be sampled. This curve can be treated as a stepping curve and by comparison with the undisturbed flat-field the three modalities can be extracted [Kottler, 2007].

3.4 Setups with a large field of view

For the before mentioned acquisition methods the maximal size of the sample is limited to the size of gratings particularly the size of G_2 . The length of a absorption gratings is typically in the range of a couple of centimetres. Therefore, other acquisition methods have to be utilised to acquire dark-field images of larger samples.

3.4.1 Grating fabrication

The gratings of Talbot-Lau interferometers have periods of several micrometre to achieve high sensitivities at relatively compact setup lengths (about 2 m) and high X-ray energies (50 keV to 80 keV). To achieve good image quality, a high structure uniformity is required over the entire grating area. A further constraint for absorption gratings is a low transmittance

behind the absorbing structures of the grating. Gold is a common material for absorption gratings, as it has good absorption properties and a high density. Nevertheless, absorption gratings usually have high aspect ratios, i.e., the ratio of structure width and height. One method to fabricate such gratings is the LIGA approach (German acronym for Lithographie, Galvanoformung, Abformung; English: lithography, electroplating, moulding). Here, a resist, an X-ray sensitive polymer, is coated onto a conductive substrate (e.g., graphite). Then, the structure of an X-ray absorbing mask is transferred into the resist by exposing the resist, placed directly behind the mask, with X-rays from a synchrotron source. After a post-exposure-bake and a chemically development of the resist only irradiated parts in case of a negative resist or non-irradiated parts in case of a positive resist remain on the substrate. In a last step, the voids are filled with gold by electroplating. The resist may be removed after electroplating. However, for gratings with high aspect ratio the resist remains often to stabilise the gold structure [Qin, 2010; Mohr, 2012]. With this method, gratings with an aspect ratio of up to 1:100 can be fabricated [Kenntner, 2012]. One major drawback of LIGA is that the size of the grating area is limited to the field of view of the synchrotron X-ray beam, which is normally between 5 cm and 7 cm. Other disadvantages are the high cost in fabrication, partly due to the synchrotron time needed, and that the outcome depends highly on the processing parameters.

Phase-shifting gratings do not have a demand for high aspect ratios. They can be produced with LIGA, where the aspect ratios are lower. Another method to produce phase gratings is deep reactive-ion etching (DRIE). Here, a combination of physical and chemical processes, like ion bombardment-enhanced desorption, ion induced damage, and spontaneous chemical etching, is used to etch structures in the material. In DRIE mainly silicon or silicon-based materials like glass are used as a work piece. [Tilli, 2010]

3.4.2 Scanning setups

As mentioned in Sec. 3.4.1 the diameter of absorption gratings is in the range of a couple of centimetres. If the projected size of the sample is larger than the (G_2) grating a trick has to be employed to image the whole sample. There are several possibilities: Firstly, several single gratings could be stitched together to cover the complete detector field of view. However, this is limited by difficulty in the production and the cost of the gratings. Secondly, images of only a part of the sample (however large the gratings are) are taken and the image of the complete sample is stitched together from the single images. An advantage of this method would be that the sample size is not limited as many images could be stitched together. This method was employed to image a complete pig [Hauke, 2018]. However, this method needs a long time for image acquisition, which increases with sample size. Another possibility is to build a scanning setup where gratings are stitched together to cover one length of the detector. For image acquisition a moiré fringe scanning, as described in Sec. 3.3.2, is performed. This method is less expensive than a full field grating as only a small strip of the detector has to be covered with gratings. Moreover, this method is relatively fast. However, artefacts can arise from motion blurring or interpolation. There are different ways to implement this

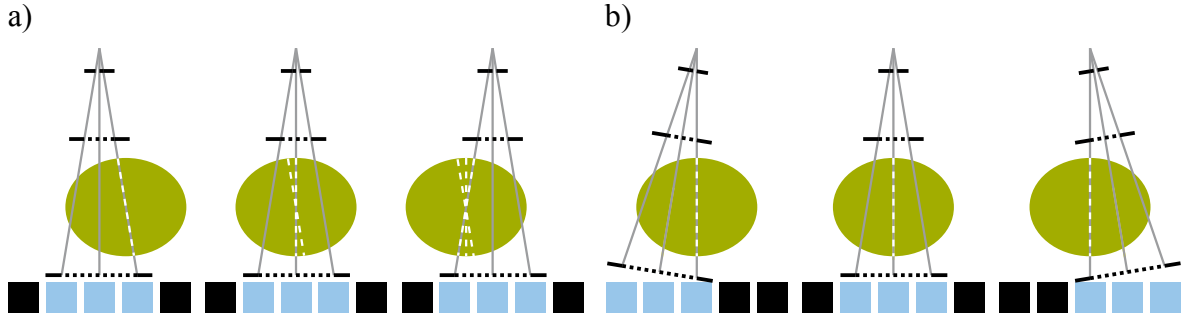


Figure 3.4: Beam path through a sample for different scanning approaches. In a) the interferometer and detector remain stationary, and the sample is moved through the exposed slot. Here the beam path through the sample depends on the relative position between the sample and interferometer. In b) the detector and sample remain stationary while the interferometer is moved. Therefore, the beam path through the sample is independent from the relative position between sample and interferometer.

approach. One method is that the interferometer, source, and detector is left stationary and the sample is moved over the fringe pattern (type A) [Kottler, 2007]. Another method is to leave sample and source stationary and move the fringe pattern over the sample by moving the interferometer, [Koehler, 2015; Gromann, 2017]. Two different ways of implementation of this method have been published: the detector is also moved with the interferometer (type B) [Koehler, 2015] or the detector is left stationary as well (type C) [Gromann, 2017]. All three acquisition types have several advantages and disadvantages. In all three acquisition types, the source emits an cone beam. This leads in type A to artefacts due to different projection angles of a sample. While the sample is moved over the grating slot/ through the X-ray beam, the angle the ray travels through a sample voxel will change depending on the position of the sample to the X-ray beam (cf. Fig. 3.4 a)). This can lead to a change in the intensity modulation, which is not a result of the moiré pattern, as the ray travels on a different path though the sample. This effect is more prominent by larger (i.e., higher) samples. This error can be reduced by reducing the opening angle of the X-ray beam, by either having a larger source- G_2 /detector distance or reducing the grating width. Another drawback from moving the sample is, that non-rigid samples might move due to the movement, and this results in artefacts. This problem will not occur in type B and C. Here, the path of the rays through the sample will not change during the scan as source and sample remain stationary (cf. Fig. 3.4 b)). However, the movement of the interferometer might lead to artefacts in type B and C due to vibration or small distortions during the scan. Furthermore, the size of the sample is not limited in type A in scan direction as it is in type B and C. Due to the stationary detector in type C this method is more expansive than type A and B as they require a smaller detector (in scan direction). On the other hand, the large detector has the advantage, that no resorting of the data is needed as one voxel is always projected the same detector pixel. In type A and B, a voxel is always projected to a different detector pixel so exact knowledge of the movement is required to resort corresponding data points. This might also lead to less spatial resolution as an interpolation is needed if the movement is not an integer of the

detector pixel size. In setups of type C such problem does not arise.

3.5 X-ray vector radiography

Most grating interferometers have one-dimensional gratings, i.e. the grating lamellae are oriented in one direction and do not cross each other as for example in a grid. Thus, the Talbot pattern only varies in one direction in the G_2 plane and the scattered X-rays due to a sample can only be measured in one direction. Parallel to the grating lamellae no change of phase and visibility can be detected. This causes no problem for isotropic scattering samples like powder or the alveoli structure in the lung. However, if the sample has an oriented microstructure like wood or bone, X-rays are scattered perpendicular to the microstructure. Therefore, the dark-field signal is dependent on the orientation of the sample to the grating lines. X-ray vector radiography (XVR) exploits this effect to gain additional information about the scattering substructure. XVR was first demonstrated by [Jensen, 2010a] taking images of a strawberry leaf. By taking several images of the sample at different orientations the scattering strength dependent on the orientation can be determined. This is demonstrated in Fig. 3.5 a). A sample consisting of a Eppendorf tube with water, a plastic rod filled with flower and two differently orientated plates of carbon fibres is imaged at different relative orientations to the grating lamellae. While the dark-field signal does not vary for different orientations, it depends strongly on the relative angle between structure orientation and grating lamellae orientation for the carbon fibres. The images are afterwards registered and the dark-field signal of a pixel varies in a sinusoidal form (cf. Fig. 3.5 b)):

$$D = \bar{D} \cdot [1 + D_A \cos(2(\Theta - \theta_s - \theta))], \quad (3.15)$$

where \bar{D} is the mean dark-field, D_A the degree of anisotropy, Θ the samples orientation around the optical axis, and θ the orientation of scattering structures. The angle θ_s is the angle between the direction of sensitivity (i.e., perpendicular to the grating lamellas) and the x-axis. The degree of anisotropy is a measure for how strong X-rays are scattered directional. The higher the degree of anisotropy, the more directed the scattering is, i.e., if the degree of anisotropy equals one, the X-rays are scattered in only one direction. In Fig. 3.5 c) the resulting images of the mean dark-field signal (left), the degree of anisotropy (middle), and the orientation of scattering structures (right) are shown. In the colour coded image of the orientation of scattering structures, the brightness of the colours corresponds to the degree of anisotropy. As expected, the water does not generate a dark-field signal, whereas the flour powder and the carbon fibre scatter the X-rays. The flour powder produces a much stronger dark-field signal than the carbon fibre plates. However, the degree of anisotropy of the carbon fibre plates is stronger than of the flour powder, which scatters isotropic. Therefore, no orientation of scattering structures could be determined for the flour powder. As the degree of anisotropy for the carbon fibre plates is not zero, an orientation of the scattering structures could be found: the fibres in the upper plate are oriented horizontally, while the ones in the lower plate run vertically. [Jud, 2018]

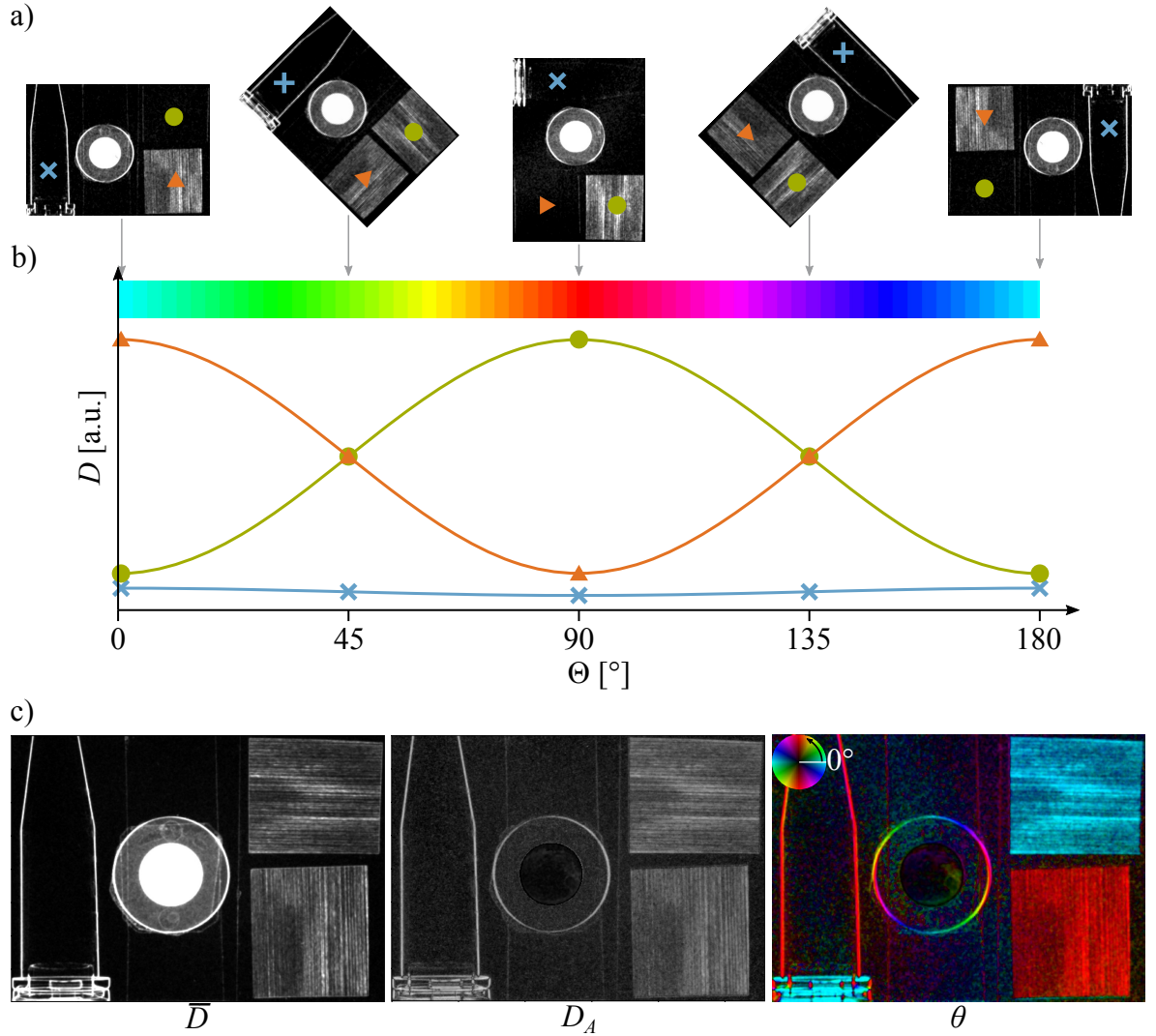


Figure 3.5: X-ray vector radiography (XVR). A phantom sample consisting of an reaction tube filled with water, a plastic rod filled with flour and two plates of carbon fibre was rotated around 180° (a). The reaction tube filled with water (blue x) and the plastic rod filled with flour scatter isotropic. Therefore, the dark-field signal remains unchanged for all rotation angles. The two carbon fibre plates (orange rectangle and green circle) have an oriented micro-structure and thus scatter mostly perpendicular to the fibre orientation. Hence, their dark-field signal changes from strong to barely visible dependent on the rotation angle. The complete courses of the rotation angle dependent dark-field signal for the reaction tube filled with water (blue x), and the two carbon fibre plates (orange rectangle and green circle) are shown in b). Analysing such courses for every pixel the mean dark-field signal \bar{D} , the degree of anisotropy D_A , and the orientation of scattering structures θ images can be reconstructed (c). Figure adapted from [Jud, 2018].

4 Body section imaging

Shortly after the discovery of X-rays many scientists from different countries developed apparatus to extract three-dimensional (3D) information from X-ray images. As the exchange between these scientists was limited, many quite similar methods were invented under many different names. The first imaging techniques used blurring of features outside a focal plane to enhance the detectability of features inside the focal plane [Webb, 1990; Littelton, 1996]. In the late 1950s a predecessor of modern computed tomography (CT) was developed by scientists from using an electrical machine for back projection [Tetelbaum, 1957; Korenblum, 1958]. The first CT scanner was developed by G. Hounsfield and A. M. Cormack in 1960s and 1970s [Cormack, 1963; Hounsfield, 1973]. Nowadays CT scanners are a widely used diagnostic tool in clinics and conventional tomography is almost only used in dental radiology.

4.1 Classical tomography

The first attempts to extract 3D data from X-ray imaging was stereo imaging. Here, a similar method to stereoscopy as used in photography was utilised. Two X-ray images are taken of the same object from two slightly different angles. By special viewing apparatuses a spatial impression of the image could be generated [Webb, 1990].

From the 1920s onward many scientists took interest in body section imaging. Similar methods to image a sharp plane inside an object were invented independently during the next two decades. One of those suggested methods was stratigraphy by A. Vallebona [Littelton, 1996]. He placed a source and detector film on a pendulum rotating around the object with the source above the object and the film below. The film was arranged perpendicular to the pendulum and did not change its orientation to the pendulum. During the acquisition, source and detector move on an arc leading to a blurring of features outside the rotation axis in the final image. As only features on the rotation axis or rotation point remain sharp in the image instead of a complete plane, this method was deemed useless for body section imaging. A similar method was proposed by G. Grossmann called tomography [Grossmann, 1935]. He also positioned source and detector film on a pendulum rotating around the object. But instead of a fixed orientation of the film to the pendulum, Grossmann arranged for the film to a fixed orientation to the object. Grossmann's tomography is depicted in Fig. 4.1 a). Three exemplary positions of the source (S1 - S3) and the corresponding detector film positions (D1 - D3) are shown. As it can be seen, points within the plane, in which the rotation point

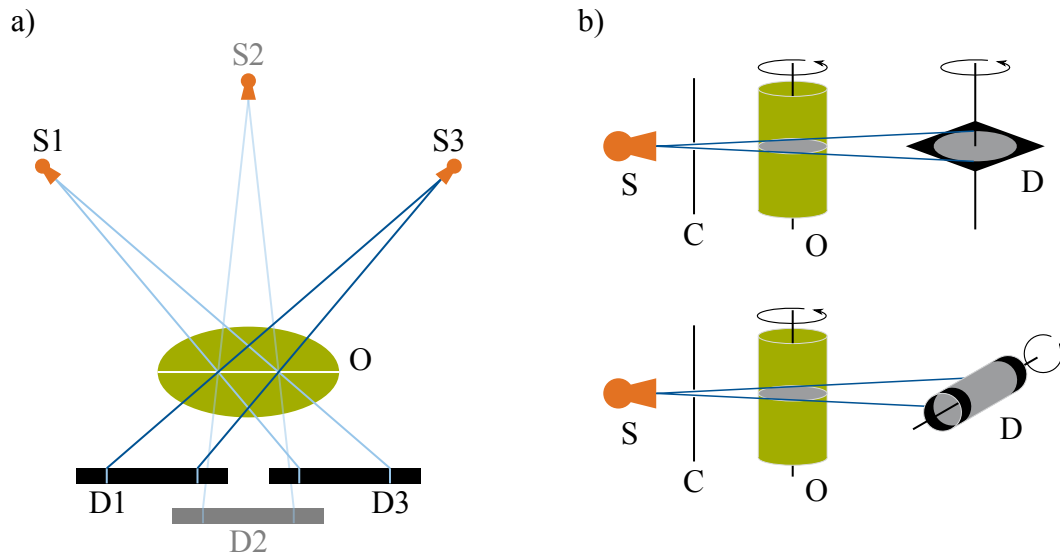


Figure 4.1: Two methods of body section imaging. In a) the schematic of tomography as proposed by Grossmann is depicted. The source (S) and detector (D) are mounted on a pendulum, rotating around the object (O). The position of rotation axis determines the focal plane. In b) a schematic of axial traverse tomography is shown. The source (S) and collimator (C) remain stationary during image acquisition. In the direct imaging method (top), the object (O) and X-ray film (D) rotate around parallel axes resulting in a slice image of the object without further processing. For the indirect imaging method, the X-ray film is rolled onto a cylinder, with its rotation axis perpendicular to the rotation axis of the object. Afterwards, the acquired sinogram is back projected to obtain the image slice. Figure adapted from [Webb, 1990].

is, are always projected to the same spot on the film, independent on the position of source and detector. For points outside this focal plane, this is not the case, leading to a blurring of features outside the focal plane. The vertical position of the focal plane can be adjusted by changing the point of rotation. Another method to generate body section images is planigraphy, developed amongst others by A. Bocage and B. Ziedses des Plantes [Ziedses des Plantes, 1932; Webb, 1990]. Here, source and detector film do not rotate around the object but move horizontally in opposite directions. Like in Grossmann's tomography points in the focal plane are projected to the same detector points and therefore remain sharp in the final image, whereas points outside the focal plane are blurred. The position of the focal plane can be adjusted by changing the velocity of the source and detector movements, e.g. if the source is faster than the detector, a plane close to the detector is in focus, whereas if the detector is faster a plane close to the source is in focus. A similar method to planigraphy was proposed by J. Keiffer [Webb, 1990]. In his apparatus, the laminograph, a source and detector film moved in horizontal direction, too. However, in contrast to planigraphy the detector film was not oriented parallel to its moving direction but tilted by a certain angle. As a result, other orientations of the focal plane in the object could be achieved as the focal plane is parallel to the detector film.

The basis of the just presented body section imaging methods is the relative movement of the source and detector film towards the sample. The path of the source can be either linear, circular, spiral or an arc during these acquisitions. The path the source follows during these acquisitions can either be linearly, circular, spiral or an arc. Here, features in the focal plane are always projected to the same point on the detector, whereas features in other planes are projected to different points on the detector. Thus, the focal plane appears sharp whereas the features in the remaining planes are blurred in the final image. Most of the invented body section imaging apparatuses were able to only record one section image at once. Therefore, to gather section images of a complete volume several acquisitions had to be performed which led to a high dose deposition in the sample. Furthermore, in early methods of body section imaging, features outside the focal plane are only blurred and not complete removed from the images.

This problem was solved with axial traverse tomography. Here, the X-ray source is positioned to a vertical sample in such a way, that the rays have a slight angle to the horizontal plane. Due to a collimator only a in vertical direction narrow beam passes through the sample. Two imaging methods were described: In the direct imaging method the X-ray film is arranged horizontally behind the sample (cf. Fig. 4.1 b) top). During the image acquisition the sample and the X-ray film are rotated around the vertical axis. The X-ray film thus records directly the imaged slice of the object. The second imaging method is indirect imaging. Here, the X-ray film is rolled onto a cylinder and positioned behind the sample with the axis of the cylinder being perpendicular to the X-ray beam direction and the vertical axis (cf Fig. 4.1 b) bottom). Thus, only a strip of the X-ray film is exposed at once. By rotating the sample around its vertical and the cylinder with the X-ray film around its long axis a sinogram is recorded on the X-ray film. The corresponding image slice can be obtained by back projection [Tetelbaum, 1957; Korenblum, 1958; Webb, 1990].

4.2 Tomosynthesis

A major disadvantage of early body section imaging is that only one focal plane is obtained per acquisition. As results a high dose is applied to the sample if several focal planes are recorded. This problem was overcome with the emergence of digital detectors and the invention of tomosynthesis. The principles of tomosynthesis are similar to those of classical tomography. The source is moved on linear or circular pathways around the sample while the detector often remains stationary. In contrast to early body section imaging techniques, in tomosynthesis many individual images are recorded at different relative positions of source, sample, and detector during one acquisition. Thus, it is possible to reconstruct multiple focal planes from one acquisition. One possible reconstruction method is the shift-and-add method. Here, the recorded images are shifted against each other in such a way that the focal plane is sharply imaged after the recorded images are added up. Other reconstruction methods are analytical reconstruction or iterative reconstruction as performed in CT imaging. However, due to the limited recorded angles filtering is used to reduce the artefacts

[Buzug, 2008]. The dose of a tomosynthesis acquisition is often similar or slightly higher than for single radiographic images [Niklason, 1997]. Nowadays, tomosynthesis is applied in mammography and dental radiology. [Park, 2007; Diekmann, 2011].

4.3 Computed tomography

A method for 3D imaging without an overlay of blurred structures outside the focal plane is computed tomography. Here, images of the sample are taken from every angle, by rotating source and detector around the sample. In a setup with a parallel beam geometry all detector pixel lines are independent from each other and a single detector line is used to reconstruct one slice of the sample. While rotating the sample each pixel line records a sinogram which can also be viewed as a series of Radon transforms. For the reconstruction the Fourier slice theorem can be used. It states that the one-dimensional Fourier transform of a projection taken under a certain angle equals the line-plot through the 2D Fourier transform of the object under the same angle. However, due to the rotation of the sample and the discrete measuring points, data density in the 2D Cartesian Fourier space is higher for low frequencies than for high frequencies. To reduce resulting artefacts, the data is filtered before the back transformation from the 2D Fourier space to the real space. [Buzug, 2008]

5 Large field of view Talbot-Lau interferometer

The ‘*linescanner*’ setup is a three grating Talbot-Lau interferometer. It is constructed to image large samples like the thorax of pigs or human bodies. As mentioned in Sec. 3.4.1, the fabrication of large gratings is challenging. Therefore, the setup is built as a scanning device to reduce the necessary grating area. The gratings, mounted on a frame (swing) pivoting around the focal spot of the source, are moved while the sample remains stationary throughout an image acquisition (confer type B described in Sec. 3.4.2). Over the years, the gratings and their configuration changed. In the beginning an asymmetric grating configuration was implemented. Currently, a symmetrical grating configuration is used in the setup. The setup is controlled via commands in the software package *spec* (Certified Scientific Software, Cambridge, MA, USA) or a graphical user interface provided by Philips. The setup in the asymmetric grating configuration was previously described in several publications, of which the most important are the dissertations of L. B. Gromann and F. De Marco [Gromann, 2017; De Marco, 2021].

5.1 Setup hardware

A schematic of the *linescanner* setup in its latest state can be seen in Fig. 5.1. Source and detector are commercially available products that remained the same over the course of this work. They are mounted at the ceiling and the floor the experimental hutch, respectively. As a result, the beam path is in vertical direction to enable imaging of samples in horizontal position. As this setup is not a commercially available setup but a self-constructed one, the complete frame supporting any component of the setup is constructed using mainly profiles and supporting elements from Bosch-Rethrox (Lohr am Main, Germany) and Linos (Qioptiq Photonics GmbH & Co. KG, Göttingen, Germany) systems. This also allows slight modification on the setup. To perform the scanning, the swing is attached to a motor. The sample is placed on the sample table which can be moved for convenience. For the motion of the swing and sample table two isel LES5 linear stages (isel Germany AG, Eichenzell, Germany) are used. The swing motor has a travel range of 540 mm and the sample table motor a range of 800 mm. Both are connected to an XPS-Q8 motion controller (Newport Corporation, Irvine, CA, USA).

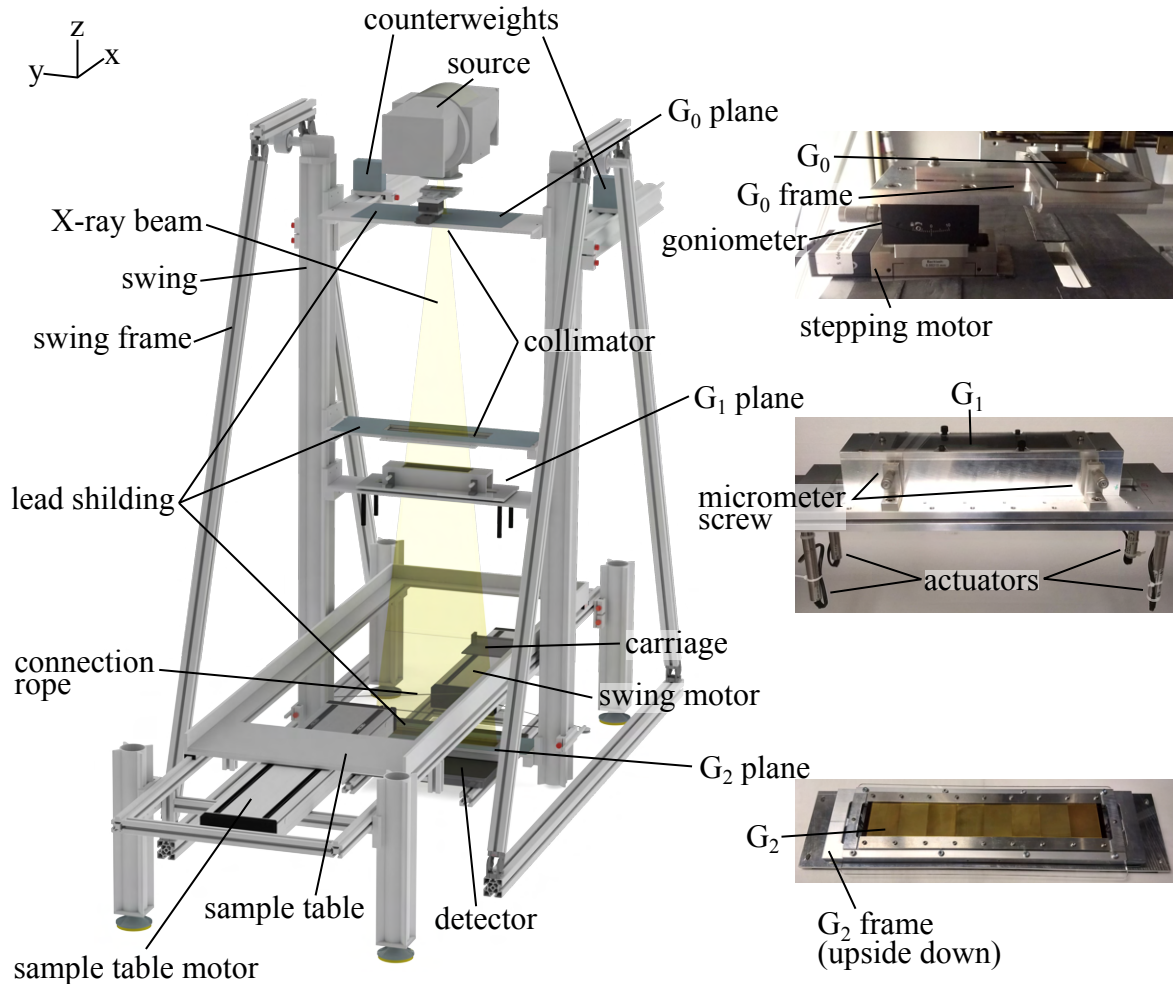


Figure 5.1: Schematic of the linescanner (left) and photos of the three grating planes (right). The source is placed at the ceiling of the experimental hutch, while the detector is located on the floor. The swing on which the grating planes are fixed rotates around the focal spot of the source and is moved by the swing motor. The G₀ is attached to the stepping motor and a goniometer. The G₁ can be moved in z-direction, and tilted around the x- and y-axis by actuators. It is clamped by micrometre screws. With these screws the grating can also be rotated around the z-axis and moved in x-direction. Close to the detector is the G₂, which cannot be moved after mounting. On the G₀ and G₂ grating planes a lead shielding is attached to reduce back scatter of the X-rays from the planes. With the collimator the X-ray beam can be shaped to the area of the gratings to reduce the dose deposition in the sample. The sample is placed on the sample table which can be moved by the sample table motor in x-direction.

5.1.1 X-ray source and detector

The X-ray source is an actively cooled tungsten rotating anode (MRC 200 0310 ROT-GS 1004, Philips Medical Systems, Hamburg, Germany). It can be operated between 40 kV and 125 kV with a tube current up to 1 A. The detector is a flat-panel detector (Pixium RF 4343, Trixell, Moirans, France) with a field of view of 43 cm \times 43 cm corresponding to 2874 \times 2840 pixels, each with a pixel size of 148 μ m \times 148 μ m. The active layer of the detector is a 600 μ m thick caesium iodide layer. A readout of 4 Hz can be achieved if the whole matrix is read out. To increase the readout speed and hence shorten the scanning time, a binning of 3 \times 3 pixels is used. The resulting pixels size is 444 μ m and a readout of 12 Hz. The tube is operated in a pulsed exposure mode, exposing only when the detector is able to record data. The software controlling the tube and detector is provided by Philips Medical Systems.

5.1.2 Swing components

The central part of the setup is the swing, used to carry and scan the gratings over the field of view. The swing is mounted on a frame (swing frame) so that the rotating axis of the swing goes through the focal spot of the source. Shortly below the rotation axis is a counterweight fixed to the swing to deflect the swing in negative x-direction. At the bottom of the swing, it is attached via a rope (connection rope) and a carriage to the swing motor. To illuminate the complete detector through the gratings, this motor pulls the swing in positive x-direction in a scanning motion. In the swing the grating planes and a collimator are mounted. Below the source the G_0 plane is located. The G_0 -frame is mounted on a high precision motor, the stepping motor, to be able to perform a phase-stepping. The stepping motor, a MFA-CC stage, is connected to a ESP-301 motion controller (both Newport Corporation, Irvine, CA, USA). Between the G_0 -frame and the stepping motor is a goniometer for adjustment of the G_0 around the y-Axis. Furthermore, the G_0 can also be adjusted by rotation mechanism around the z-axis incorporated in the G_0 frame. The stepping motor is mounted on the G_0 plane, which in turn is part of the swing. For the adjustment of G_1 , four actuators (TRA12PPD, Newport Corporation, Irvine, California, USA), connected to the XPS-Q8 motion controller, and four micrometre screws are available, allowing rotation and movement of the grating in all three axes. As the G_1 is the only grating that can be moved along and rotated around all axes, the micrometre screws and the actuators are used to modify the detected fringe pattern. Closest to the detector the G_2 plane with the G_2 , which is the only grating that cannot be moved once it is fixed in the frame, is placed. Additionally to the pre-collimation on the G_0 plane, a collimator is also placed above the G_1 in the swing. This collimator enables a more exact collimation and reduces Compton-scatter and the deposition of dose in the sample.

During the course of this work the gratings and their configuration changed. First, the gratings were arranged in an asymmetric configuration (configuration 1). Here, G_2 was not placed in a fractional Talbot distance, but it was rather placed so close to G_1 , an absorption

grating, that it was in the shadow of the reference grating. Therefore, the setup was more stable with respect to mechanical vibrations. To cover the whole width of the detector, G_1 and G_2 were stitched together from eight halved tiles of $5\text{ cm} \times 5\text{ cm}$ single gratings. The resulting detector image of the fringe pattern can be seen in Fig. 5.2 a). One can depict the projected stitching edges from the G_1 and G_2 by discontinuities of the moiré fringe pattern. At some stitching edges the gap between two neighbouring tiles is larger than one detector pixel. As a consequence, vertical lines with no visibility are present. In Fig. 5.2 d) and e) the mean intensity \tilde{A} and the mean visibility V along the slot width can be seen (green graph). The mean intensity drops to the border of the slot because of shadowing effects of the grating lamellae due to the cone beam. The mean visibility is around 0.3 and almost constant over the whole slot width. More details on the gratings can be found in Tab. 5.1. For a schematic of this grating configuration see dissertation of F. De Marco [De Marco, 2021]. Furthermore, the setup with this grating configuration has a rather low maximal sensitivity, although this is not necessarily a problem when measuring human or pig lungs, as their many air-tissue interfaces result in a strong dark-field signal.

Nevertheless, the grating configuration was changed to achieve a higher maximal sensitivity (configuration 2). Now the gratings were arranged in symmetric geometry. G_1 was replaced by an π -phase-shifting grating made out of one silicon wafer. As the interferometer has now a symmetric geometry and the former G_2 was also used in this configuration, the periods of G_1 and G_0 are now, like the period for G_2 , $10\text{ }\mu\text{m}$. Therefore, also a new G_0 was needed. Also, a new stepper motor was installed (MFA-PPD, Newport Corporation, Irvine, CA, USA). The detector image of the fringe pattern can be seen in Fig. 5.2 b). Comparing this image to the detector image of configuration 1, it is visible that less stitching edges are present as G_1 is now made from one piece. Mean intensity \tilde{A} and visibility V along the slot width are shown in Fig. 5.2 d) and c) (blue graph). Again, the visibility is almost constant at 0.3 over the whole slot width. However, the mean intensity drops lower than the mean intensity of configuration 1. Again, all grating parameters can be found in Tab. 5.1.

To enable a faster image acquisition, this configuration was later again changed and a wider G_2 was installed in the *linescanner* (configuration 3). A schematic of the *linescanner* and photographs of the gratings of this configuration is depicted in Fig. 5.1. As the inter grating distances and periods of the gratings did barely change, compared to configuration 2, both configurations (2 and 3) have similar sensitivities and correlation length. The G_2 consists now of 8 grating tiles each with a size of approximately $56\text{ mm} \times 75\text{ mm}$. Since shadowing effects increase with grating width, the two absorption gratings were bent according to the cone beam geometry to reduce this effect. Bending the reference grating was not deemed necessary as shadowing effects increase with higher aspect ratios and the G_1 has a four times smaller aspect ratio as the absorption gratings. The image of the detected fringe pattern is shown in Fig. 5.2 c). The grating tiles of the G_2 are slightly misaligned as visible on the different orientations of the fringe pattern of the single tiles. To prevent the G_0 , the grating with the smallest bending radius, from breaking during bending, a slightly too large bending radius was chosen. Therefore, shadowing effects are still present and mean intensity \tilde{A} along the slot width drops to both sides of the slot despite the bent gratings (cf. Fig. 5.2 d), orange graph). However, without bending of the gratings these effects would be even stronger. The

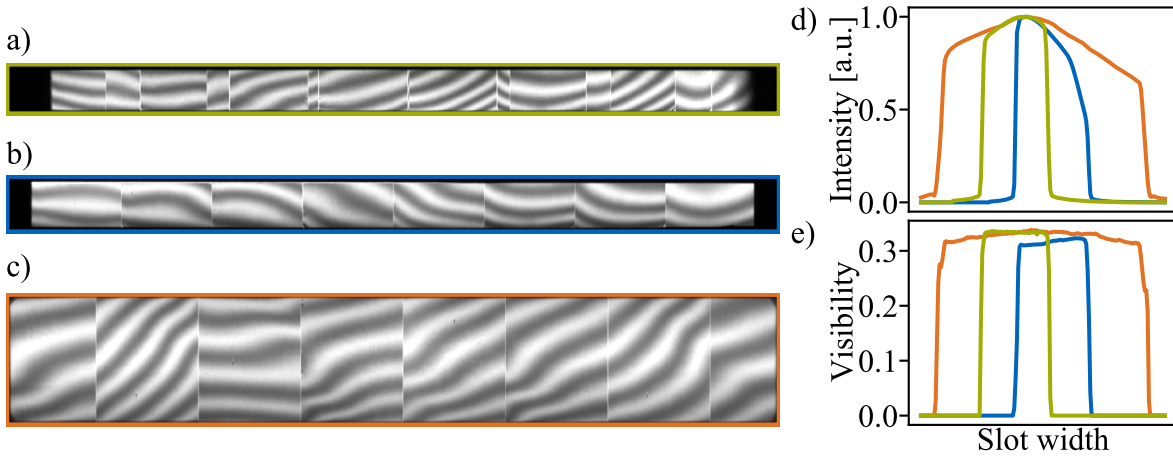


Figure 5.2: Fringe pattern of the asymmetric geometry (configuration 1) (a), symmetric geometry with small G_2 (configuration 2) (b), and symmetric geometry with wider G_2 (configuration 3) (c). In (d) and (e) the mean in horizontal direction of the intensity and visibility, respectively. Graphs correspond to the grating configuration where the colour of the graph and the box colour of sub-figure (a)-(c) are the same.

visibility V is, like at the other two configurations, almost constant at 0.3 over the whole slot width (cf. Fig. 5.2 e), orange graph). To reduce Compton scatter lead shielding was placed on the G_0 plane, collimator plane, and the G_2 plane. Furthermore, the collimators were exchanged, such that the collimated area can now be adjusted to the needed size. Again, further details on the grating parameters can be found in Tab. 5.1.

5.2 Data acquisition and processing

The user interaction with the setup is mainly via the *spec* software package (Certified Scientific Software, Cambridge, MA, USA) in a console or macros. With this the tube and detector settings as well as the motors can be controlled. For data processing packages of the python programming language are used.

5.2.1 System control and data acquisition

The X-ray system is controlled by a control software, provided by Philips Medical Systems DMC GmbH (Hamburg, Germany), running on a Windows 7 PC. This software controls and synchronises the detector and the generator, which in turn controls the X-ray source, to minimise dose in the sample. The control software sets exposure specific parameters like the exposure time, tube current, peak voltage, and number of shots, as well as detector specific parameters like gain settings, the field of view of the detector and binning settings. The

		configuration 1	configuration 2	configuration 3
G ₀	period	68.72 μm	10 μm	10 μm
	duty cycle	0.7	0.72	0.68
	height	240 μm	215 μm	205 μm
	material	Au	Au	Au
	substrate	Graphite	Si	Graphite
	area	50 mm \times 50 mm	50 mm \times 50 mm	30 mm \times 70 mm
	bending radius	∞	∞	20 – 30 cm
	manufacturer	Microworks	KIT	KIT
	method	LIGA	LIGA	LIGA
G ₁	period	8.73 μm	9.9 – 10 μm	
	duty cycle	0.50 – 0.58	0.6	
	height	150 – 180 μm	59.1 μm	
	material	Au	Si	
	substrate	Si	Si	
	area	8 \times 25 mm \times 50 mm	225 mm \times 60 mm	
	bending radius	∞	∞	
	manufacturer	Microworks	5microns	
	method	LIGA	DRIE	
G ₂	period	10 μm		10 μm
	duty cycle	0.5		0.55
	height	ca. 180 μm		200 μm
	material	Au		Au
	substrate	Si		Si
	area	8 \times 25 mm \times 50 mm		8 \times 56 mm \times 75 mm
	bending radius	∞		\approx 2 m
	manufacturer	KIT		KIT
	method	LIGA		LIGA
G ₀ – G ₁ distance		1599 mm	898 mm	919 mm
G ₁ – G ₂ distance		231 mm	890 mm	913 mm

Table 5.1: Grating parameters of the different configurations. An bending radius of ∞ implies that the grating is not bent. Grating manufacturer are indicated by Microworks (Microworks GmbH (Karlsruhe, Germany)), KIT (Micro and X-ray optics department at Institute of Microstructure Technology (IMT), Karlsruhe Institute of Technology (KIT, Karlsruhe, Germany)) and 5microns (5microns GmbH (Berlin, Germany)).

parameter for the exposure and detector is forwarded to the control software from either a graphical user interface running on the windows PC or the *spec* software package running on a Linux PC. The motion controller XPS-Q8 and ESP-301 transmit motion commands to the motors. The commands can originate either from a keypad (ESP) and an internet browser interface (XPS) or from commands in the *spec* programme.

There are two data acquisition modes. Firstly, the data can be acquired by a conventional phase-stepping. Here, the swing remains in the same position throughout the data acquisition, only the G_0 is moved with each step. As a result, only the collimated slot is imaged on the detector. The other acquisition mode is the fringe scan, imaging the complete field of view of the detector in a single acquisition. This is achieved by taking a series of images while the swing and thus the collimated slot is moving over the detector. The acquisition in pulsed mode starts as soon as the collimated slot reaches the detector. Every pulse generates an image on the detector which is written in a multi-frame binary file. Since the velocity of the swing and the pulse interval are constant, the distance between two consecutive imaged slots on the detector remains constant. When the swing reaches the other side of the detector the acquisition is finished. As for every pulse only a part of the detector is illuminated and contains information, the images are saved in a cropped mode, where the not illuminated part of the image is disregarded, to reduce used storage space.

5.2.2 Processing of the recorded data

The recorded data is processed using packages written in the *Python* programming language [De Marco, 2021]. Stepping data is processed by fitting the data to Eq. (3.8). As the fringe scan data in the saved form cannot be used for processing, in a first step the data needs to be resorted, as illustrated in Fig. 5.3. The cropping process is reversed, by adding zeros before and after the cropping boundaries. The resulting image stack is illustrated in Fig. 5.3 a). Here the τ -axis indicates the different position indices of the swing. Next, the mean is taken along the y -axis. The result is a 2D array with a bright, diagonal running bar, as depicted in Fig. 5.3 b). Then, a line is fitted to the top and bottom of the bar (orange lines in Fig. 5.3 b)). With this line, the distance between the bar and $\tau = 0$ can be calculated for each pixel column. Then, the column of the uncropped data is shifted by the corresponding distances (constant distance in y -direction) in negative τ -direction. Thus, the dependence on τ was replaced by a dependence on the relative position of the grating slot to a pixel (cf. Fig. 5.3 c)). In case of perfect gratings, it would be possible to calculate from that data set the transmission and dark-field image, as the intensity modulation is similar to a stepping curve. However, the gratings at the *linescanner* are not perfect and a more elaborate method is needed. To account for imperfections in the gratings a combination of *swing-scan* and stepping is performed for the flat-field acquisition. After each *swing-scan*, the G_0 grating is moved by a fraction of its period. This is repeated until a complete period of G_0 is sampled. The resulting data is not only dependent on the pixel positions x and y but also on the relative position j of the slot to a pixel and the G_0 displacement η . The resulting intensity modulation

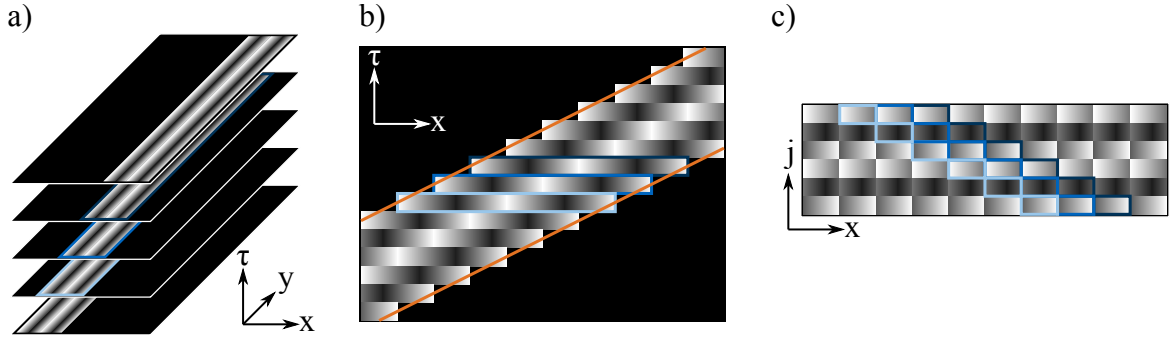


Figure 5.3: Data resorting for the fringe scan processing. a) First the cropping of the data is reversed, resulting in a 3D array where the illuminated slot has different y -positions for different τ . b) After taking the mean in y -direction, two lines are fitted to the resulting diagonal bright bar. From these lines the distance between $\tau = 0$ and the bar can be calculated for each pixel column. c) Each pixel column is shifted by this distance in negative τ -direction. The resulting array is now dependent on the relative position of the slot to a pixel j . Figure adapted from [De Marco, 2021].

is similar to Eq. (3.8):

$$I_{\eta j}^{\text{ref}} = \tilde{A}_j^{\text{ref}} \cdot \left[1 + V_j^{\text{ref}} \cdot \cos(\phi_\eta + \varphi_j^{\text{ref}}) \right], \quad (5.1)$$

where the mean intensity, the visibility and the phase are now dependent on the relative position of the slot to the pixel (j). As \tilde{A}_j^{ref} , V_j^{ref} , and φ_j^{ref} are independent of η they can be determined by a least square minimisation in terms of η .

The intensity for the sample scan cannot be described by the same equation as no stepping was performed for those measurements. The intensity of a sample scan can be expressed by inserting Eq. (3.9) to Eq. (3.11) into Eq. (3.8) and removing the stepping dependence parameter ϕ_η :

$$I_{j\text{sam}} = T \tilde{A}_j^{\text{ref}} \cdot \left[1 + \mathfrak{D} V_j^{\text{ref}} \cdot \cos(\varphi_j^{\text{ref}} + \Delta\varphi) \right]. \quad (5.2)$$

Here, the intensity of one pixel is dependent on the relative position of the slot to the pixel but not on η . The optimisation process can be simplified applying the identity $\cos(x + y) \equiv \cos(x)\cos(y) - \sin(x)\sin(y)$ and rearranging Eq. (5.2) to

$$I_j^{\text{sam}} = P_1 \tilde{A}_j^{\text{ref}} + P_2 \tilde{A}_j^{\text{ref}} V_j^{\text{ref}} \cos(\varphi_j^{\text{ref}}) - P_3 \tilde{A}_j^{\text{ref}} V_j^{\text{ref}} \sin(\varphi_j^{\text{ref}}), \quad (5.3)$$

with $P_1 = T$, $P_2 = T \mathfrak{D} \cos(\Delta\varphi)$, and $P_3 = T \mathfrak{D} \sin(\Delta\varphi)$. Least square minimisation of this function determines the parameters P_1 , P_2 , and P_3 . The transmission, dark-field and differential-phase can be calculated with $T = P_1$, $\mathfrak{D} = \frac{\sqrt{P_2^2 + P_3^2}}{P_1}$, and $\Delta\varphi = \arctan \frac{P_3}{P_2}$.

5.2.3 Post-processing

The processing python package contains several post-processing scripts. The two most relevant post-processing methods for this thesis are a beam hardening correction and a noise-

reduction for the dark-field images.

Beam hardening correction

The visibility of a Talbot-Lau interferometer depends on the energy of the X-rays, as the Talbot distances as well as the gratings absorption and phase-shifting abilities depend on the photon energy. Therefore, if polychromatic sources are used, the visibility depends on the X-ray spectrum. Attenuating objects change this spectrum and thus change the measured visibility. This may result in an apparent dark-field signal which does not originate from small-angle scatter. To rectify for this effect a correction method (beam hardening correction) is applied. The correction method is similar the one presented by [Pelzer, 2016]. Since the *linescanner* was built to measure the thorax region of humans and pigs, a beam hardening correction method to correct for apparent dark-field signal originating from soft and adipose tissue was implemented. As a phantom material polyoxymethylene (POM) is used, as it has a similar energy-depending absorption coefficient as soft and adipose tissue. Different thicknesses of the phantom material are measured to determine the transmission and apparent visibility reduction values for each height of phantom material. The measured points were fitted by power-law relationship By fitting the measured points to a power-law relationship, a function $\mathfrak{D}_{\text{POM}}^{\text{BH}}(T)$ is obtained for POM. This function represents the apparent visibility reduction depending on the transmission signal. This function can be used as a look up table for the falsely generated dark-field signal due to absorption by the sample. The corrected dark-field signal can be determined by:

$$\mathfrak{D}^{\text{corr}} = \frac{\mathfrak{D}}{\mathfrak{D}_{\text{POM}}^{\text{BH}}(T)} \quad (5.4)$$

Note that $\mathfrak{D}^{\text{BH}}(T)$ depends on the used X-ray spectrum and therefore has to be recorded at the same tube voltage as the sample measurement. Furthermore, if the absorption coefficient of POM differs too much from the absorption coefficient of the sample (e.g., bones) a different phantom material has to be chosen for reference. If several absorbing materials are present in a sample and the relative thicknesses are not known, further sample measurements (e.g., at different energies) have to be performed to correct for all absorbing materials.

Noise-reduction

Another effect arising in images of samples with highly attenuating materials is the induced noise in the images. The noise in transmission images depends on the detector dose, the noise in the dark-field image has an additional dependency on the visibility. [Revol, 2010; Chabior, 2011] Strong noise appears patchy and may impair the visual image impression. To enhance the visual image impression a low-pass filter can be applied to the dark-field images. However, applying a low-pass filter to the image has the disadvantage of the loss of image resolution. Therefore, a trade-off between resolution and image noise had to be found.

First, a 5×1 median filter was applied to reduce the appearance of lines originating from the grating gaps. Then a 3×3 binomial filter was applied to reduce the patchiness of the image.

6 Tube voltage optimisation in X-ray dark-field human chest imaging

With the construction of a large-field-of-view setup it is now possible to acquire dark-field images of large samples like the human thorax in a couple of seconds. This was an important step of translating X-ray dark-field imaging into the clinics. An important aspect for all X-ray imaging techniques in the clinics is to obtain the best possible diagnostic images at a dose as low as reasonably achievable. For conventional radiography well established protocols exist and optimal imaging parameters, e.g., tube voltage, tube current and exposure time, was widely examined during the last decades. In the following a closer look on the optimal tube voltage will be taken. For attenuation based chest imaging best results were achieved at tube voltages of 120 to 130 kV, whereas the optimal tube voltage for bone imaging is 70 to 80 kV [Muhogora, 2012; Ekpo, 2014]. As X-ray dark-field chest radiography is a new imaging technique, the value of the optimal tube voltage is an important parameter for future studies. However, for the image quality of a dark-field image not only the detector dose is an important parameter but also a high dark-field signal strength and a high setup sensitivity. As it can be seen in Eq. (2.25) the refractive index decrement is proportional to the inverse square of the photon energy and as a result the dark-field signal decreases at least as rapidly. The sensitivity depends on one hand on the placing of the sample in the setup, on the other hand on setup specific parameters such as the grating periods and intergrating distances. To generate X-ray dark-field images with high contrast at high tube voltages either small grating periods or large intergrating distances are required. Producing strongly absorbing gratings with a small periods is challenging, whereas long intergrating distances are limited by special and technical constraints. Therefore, a reasonable compromise between image quality and tube voltage has to be found, and the findings are presented here.

The findings in this chapter were published in the studies *Optimization of tube voltage in X-ray dark-field chest radiography* and *Correlation of image parameter and tube voltage in X-ray dark-field chest radiography: results of the first human in-vivo scanner* both by A. P. Sauter, J. Andrejewski et al. ([Sauter, 2019], [Sauter, 2021]). Figures and text passage in this section may appear identically to the publications. My primary contribution in both studies were the quantitative evaluation as well as the physical and technical sections of the manuscript.

Tube voltage [kV]	60	70	80	90	100	110	120
Visibility [%]	36 ± 4	29 ± 3	22 ± 3	19 ± 2	18 ± 2	18 ± 2	18 ± 2
Tube current [mA]	600	360	450	400	360	327	300
DAP [μGym^2]	42	36	61	72	83	94	102

Table 6.1: Image acquisition parameter at examined tube voltages. Visibility is given as the mean and standard deviation of the complete field of view. Dose area product (DAP) was measured 16 cm above sample table.

6.1 Tube voltage optimisation at the *linescanner*

The following study was performed on the *linescanner*, the pre-clinical prototype for X-ray dark-field thorax imaging. X-ray dark-field and attenuation images at different tube voltages were acquired of the thorax of a deceased human body. The images were evaluated in a reader study in terms of signal strength and image quality. Furthermore, a quantitative evaluation of the dark-field signal was performed.

6.1.1 Materials and Methodes

Imaging setup

For the study we acquired X-ray dark-field and attenuation thorax radiographs at tube voltages ranging from 60 kV to 120 kV in 10 kV intervals. The setup used in this study was the *linescanner* in the configuration 1 (cf. Sec. 5.1). The total time of the measurement was 40 min. The data were acquired in a moiré fringe scanning procedure and the resulting dark-field and attenuation images were calculated using Eq. (5.1) to Eq. (5.3) and Eq. (3.13) and Eq. (3.14). Furthermore, the dark-field signal was corrected for beam-hardening effects according to Eq. (5.4). Furthermore, the dark-field images were lowpass filtered with a 2D gaussian kernel ($\sigma = 3.2$ px). Image acquisition parameters can be found in Tab. 6.1.

Human body

The measurements were performed on a body of a 64-year-old male 48 h post-mortem in supine anteroposterior position. The body weighed 69 kg and was 169 cm in height. The lung was ventilated by an anaesthesia machine (Fabius Tiro, Drägerwerk AG & Co. KGaA, Lübeck, Germany) with 25 mbar during the measurements. The experiments were conducted according to the Declaration of Helsinki and approved by the institutional review board (Ethikkommission der Ludwig-Maximilians-Universität München, Pettenkoferstr. 8a, 80336 München, project number 14-13).

Reader Study

The study was performed independently by three blinded readers. All readers are familiar with dark-field images, as they participated in previous studies. Nevertheless, the readers received training previous to the study by presenting them dark-field images with low, moderate, and high signal strength.

In total, two reading sessions were conducted: In the first session, each image was rated individually and in the second session a joint reading of images of one type (i.e., dark-field and attenuation) was performed. In each reading, signal strength and image quality were rated on a six-point scale.

The point scale for the dark-field signal strength was as follows: 0 - no signal; 1 - low signal; 2 - low-moderate signal; 3 - moderate signal; 4 - moderate-high signal; 5 - high signal. For attenuation images the levels were: 0 - complete consolidation with no lung visible (e.g., effusion); 1 - consolidation (e.g., lobar pneumonia); 2 - between 1 and 3; 3 - ground glass; 4 - between 3 and 5; 5 - normal lung. The score was rated for six zones: both left and right lung were divided in upper, middle, and lower zone (cf. Fig. 6.5 middle). The windowing of the images was fixed for the evaluation of the signal strength to avoid influences of individual windowing.

The point scale for the image quality was identical for attenuation and dark-field images: 1 - not diagnostic; 2 - sufficient; 3 - satisfactory; 4 - good; 5 - very good; 6 - excellent. Here, the score was only rated for the right and left lung (cf. Fig. 6.5 middle). Furthermore, for the evaluation of the image quality the windowing was alterable by the readers to obtain an individually optimal image impression.

Statistical analysis

Statistical analysis was performed with the computer programmes SPSS (International Business Machines Corporation (IBM), USA), Excel 2016 (Microsoft Corporation, USA), and Prism 7 (GraphPad Software Inc, USA). Inter-reader agreement and agreement between two reading sessions were calculated with Spearman's ρ . No agreement is indicated by values < 0 . Values of 0 – 0.20 indicate a slight, 0.21 – 0.40 a fair, 0.41 – 0.60 a moderate, 0.61 – 0.80 a substantial, and 0.81 – 1 an almost perfect agreement.

Quantitative evaluation of the dark-field signal

For quantitative evaluation seven region of interest (ROIs) were selected. In each lung zone, one ROI was placed and the seventh ROI was placed in the vicinity of the lung to determine background signal level. Each ROI had a size of 30 px \times 30 px, which correlates to 11 mm \times 11 mm in the sample plain. The position of the ROIs in the lung were selected

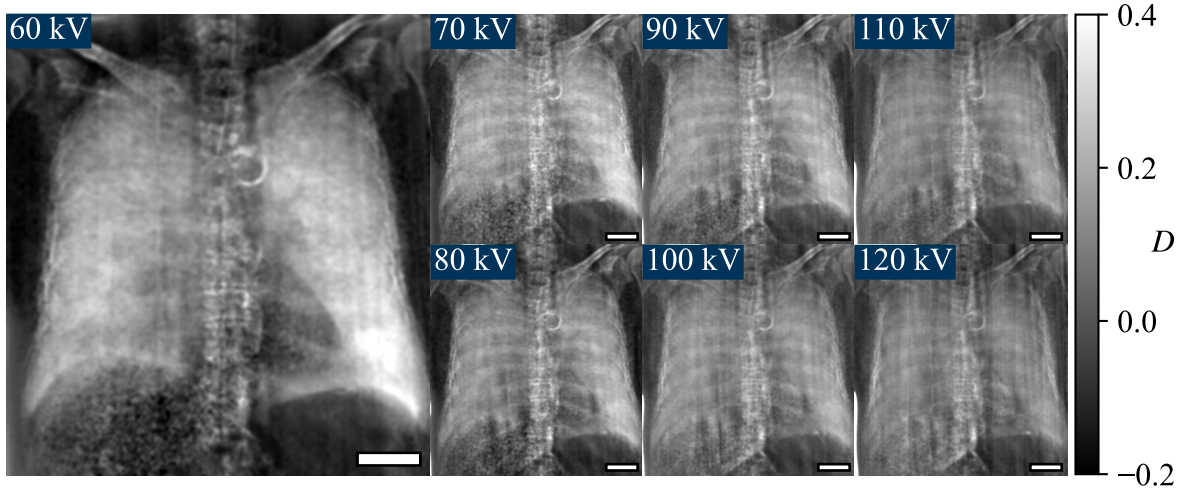


Figure 6.1: Dark-field images of a human thorax at the examined tube voltages. Same window and level are applied for all images. The scale bar in the lower right corner has the size $5\text{ cm} \times 1\text{ cm}$. The dark-field signal is found to be the highest at 60 kV of all examined tube voltages. Image quality decreases for higher tube voltages. As the result of an infiltrate a lower signal is present in the lower right lung.

such that no parts of ribs were in the ROI. As the images were taken consecutively without moving the body and movement due to ventilation in ROI was negligible, each ROI consist of the same anatomical region for all measured images. For each ROI r the mean $\mathfrak{M}_{r,U}$ and standard deviation $\Sigma_{r,U}$ were calculated for every tube voltage $U = 60, 70, \dots, 120\text{ kV}$:

$$\mathfrak{M}_{r,U} = \langle D(U) \rangle_r, \quad \Sigma_{r,U} = \sqrt{\text{Var}_r[D(U)]} \quad (r = a, \dots, g). \quad (6.1)$$

The dark-field contrast C (i.e., the difference of the mean of a ROI in the lung and the mean of the ROI in the background) and its standard deviation (i.e., error bars in Fig. 6.5) were calculated using:

$$C_{r,U} = \mathfrak{M}_{r,U} - \mathfrak{M}_{g,U}, \quad \Sigma_{r,U}^{(C)} = \sqrt{\Sigma_{r,U}^2 + \Sigma_{g,U}^2} \quad (r = a, \dots, f). \quad (6.2)$$

6.1.2 Results

Dark-field and attenuation images at all examined tube voltages are displayed in Fig. 6.1 and Fig. 6.2. Images are displayed in posterior anterior view, i.e., right lung is depicted on the left side and vice versa. Examination of the lung by a coroner suggested an infiltrate in the lower right lung.

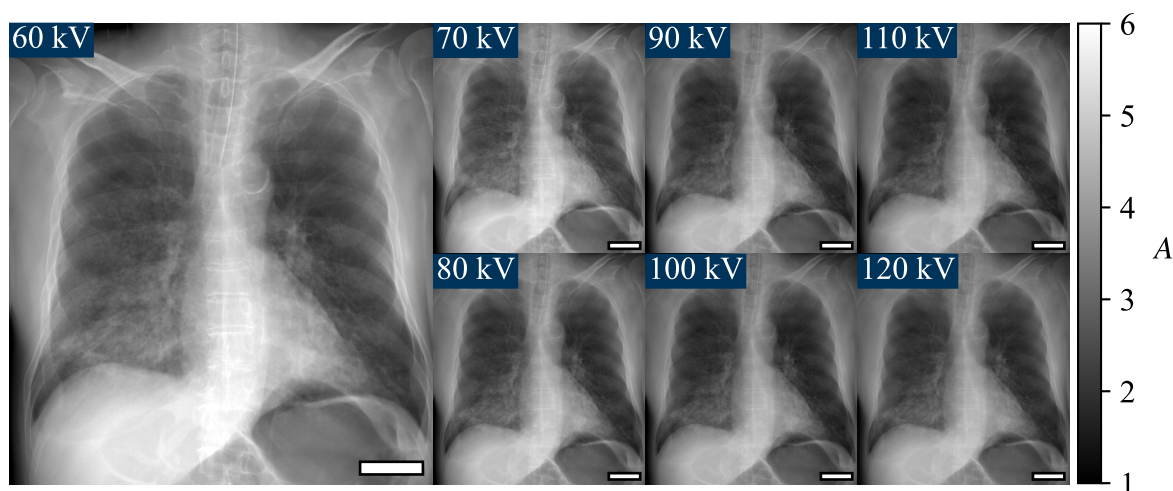


Figure 6.2: Attenuation radiographs of a human thorax at the examined tube voltages. All images are shown with the same windowing. The scale bar in the lower right corner has the size 5 cm × 1 cm. Signal strength and image quality barely changes for different tube voltages.

Reader study

The median of signal strength score in attenuation is constant in each lung zone at each tube voltage (see Fig. 6.3 bottom and Tab. A.2). Only the upper zone of the right lung exhibits a higher median signal strength score (by one point) at 120 kV than at lower tube voltages. The left lung exhibits a higher signal strength score in all lung zones than the right lung. In both lungs the upper zones have a higher score than the lower zone. This is in agreement with the autopsy findings, as a possible infiltrate was found in the lower right lung.

Signal strength score of dark-field images decreases in all zones for higher tube voltages (see Fig. 6.3 top and Tab. A.2). Highest overall signal strength was found in the lower zone of the left lung. In the left lung, the signal strength score decreases from lower to upper zone. Furthermore, the signal strength score of the upper and middle zone of the right lung are similar to the score of corresponding zones in the left lung. However, the signal strength score of the lower zone of the right lung is lower as the signal strength score to the lower zone of the left lung. This again correlates to the findings of the infiltrate.

The median image quality score for attenuation images is constant over all tube voltages. For higher tube voltages the score tends to be higher (cf. Fig. 6.4 right sides error bars). For dark-field images the median image quality score is almost constant up to 90 kV and decreases for higher energies.

Substantial to almost perfect inter-reader agreement in signal strength and image quality was found regarding attenuation images (cf. Tab. 6.2. Regarding the dark-field images, inter-reader agreement was substantial in signal strength and fair to substantial in image quality. The agreement between ‘grouped’ and ‘individual’ reading sessions was almost perfect to

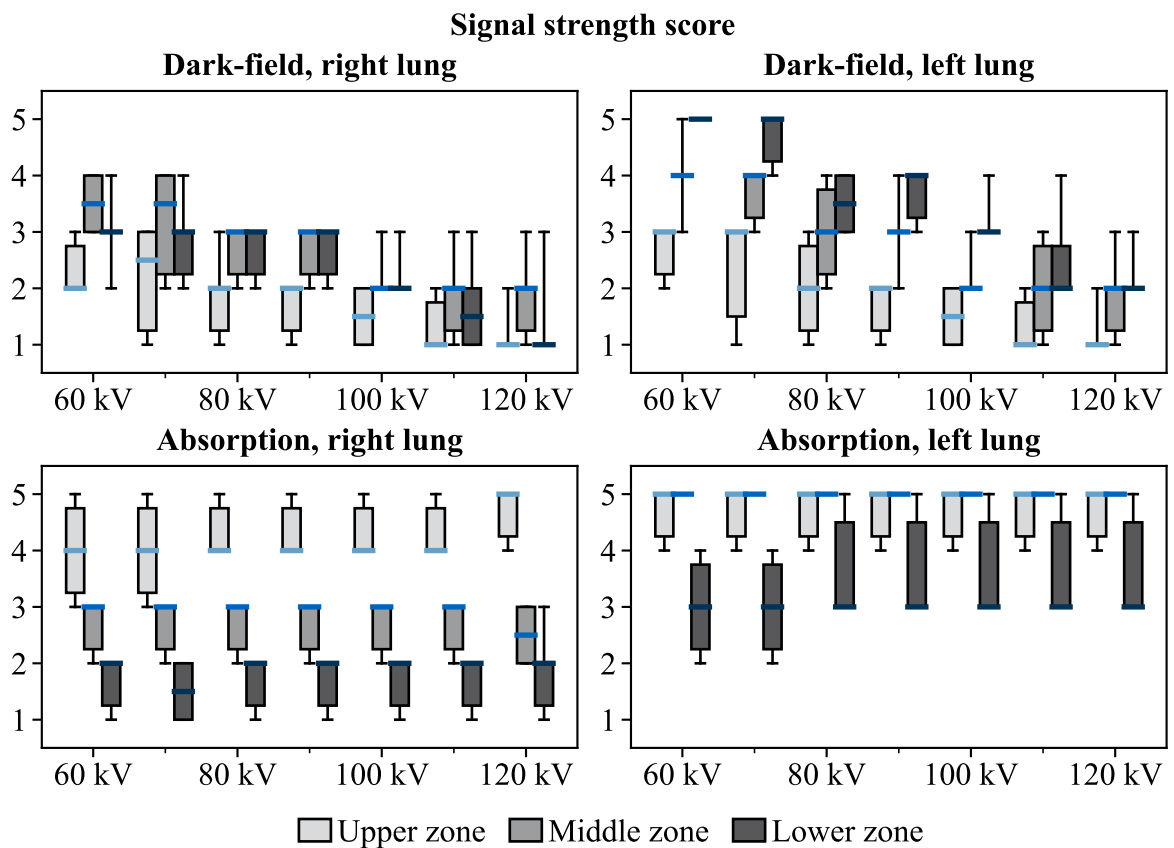


Figure 6.3: Signal strength score (median and range) of dark-field (top row) and attenuation (bottom row) images. Signal strength score is almost constant at all tube voltages in attenuation images. In dark-field images, the signal strength score decreases toward higher tube voltages. In the left lung the dark-field signal strength score increases from upper to lower zone. The dark-field signal strength score of the lower right lung is lower than the score of the lower left lung. This correlates with the findings of an infiltrate in the lower right lung.

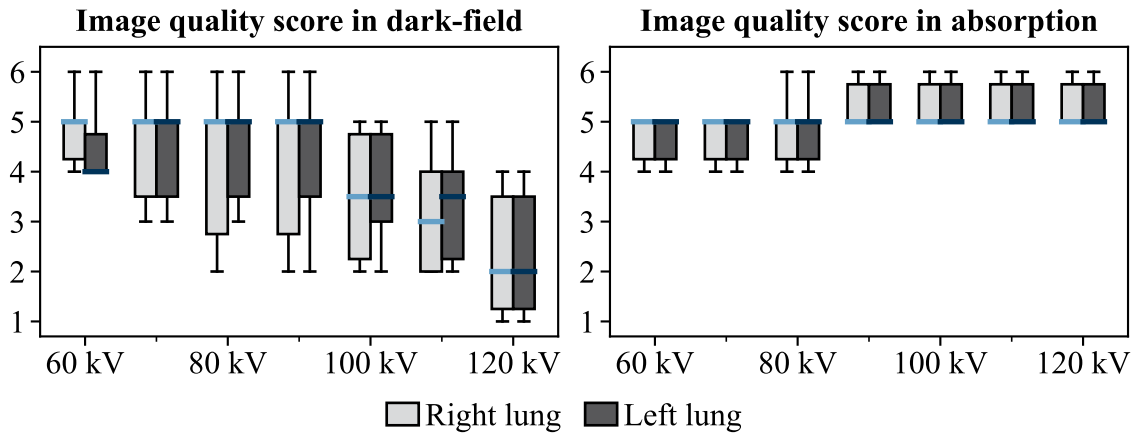


Figure 6.4: Image quality score of dark-field (right) and attenuation (left) images for right and left lung at the examined tube voltages. Image quality score is constant in attenuation images. In dark-field images, the score decreases towards higher tube voltages

	Signal strength		Image quality	
	Dark-field	Attenuation	Dark-field	Attenuation
Inter-reader agreement (combined from both reading sessions)				
Readers 1 and 2	0.755	0.623	0.498	N/A
Readers 1 and 3	0.754	0.674	0.310	0.861
Readers 2 and 3	0.658	0.918	0.677	N/A
Reader agreement between the two reading sessions				
Intra-reader 1	0.814	0.999	0.473	1.000
Reader 2	0.952	0.980	0.882	N/A
Reader 3	0.945	1.000	0.823	0.730

Table 6.2: Inter-reader agreement and intra-reader agreement between the two reading sessions. Agreement was calculated with Spearman's ρ . Values of 0.21-0.40 were considered as fair, 0.41-0.60 as moderate 0.61-0.80 as substantial, and 0.81-1 as almost perfect. Undefined values of Spearman's ρ due to zero variance in the score are denoted with N/A.

perfect regarding attenuation images and dark-field images in both signal strength and image quality. Only one reader had substantial agreement in image quality regarding attenuation radiographs and one in image quality regarding dark-field images. In Tab. 6.2 N/A denotes undefined values for Spearman's ρ , which could not be calculate due to zero variance in the score.

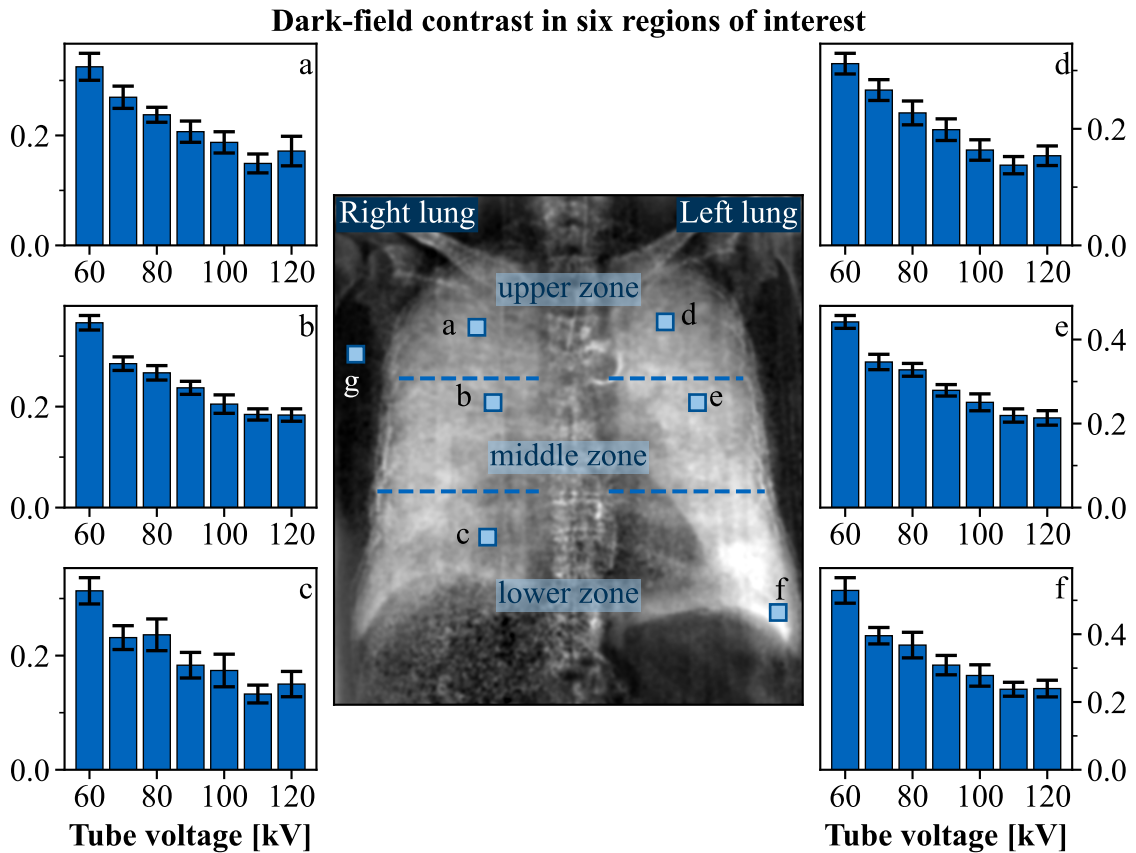


Figure 6.5: Dark-field contrast in six ROIs (a-f) with respect to a ROI in the background (g). The letter in the graphs correspond to the ROI of the same letter. In the central image (acquired with 60 kV) the position of each ROI, each a 30×30 pixel square, is highlighted and the six lung zones assumed in the reader study are indicated.

Quantitative evaluation of dark-field contrast

In Fig. 6.5 the result of the quantitative evaluation is shown. For all lung zones the contrast decreases towards higher tube voltages. In ROIs a, c, and d a slight deviation from this trend is visible. Furthermore, the quantitative evaluations provide similar findings as the reader study: The highest contrast was found in the lower left lung and it decreases toward the upper zones. However, the right lung produces a lower contrast than the left lung, as here an infiltrate is present.

6.1.3 Discussion

In all ROIs highest contrast was found at 60 kV by the quantitative analysis of lung dark-field contrast. Even though the ventilation pressure was kept constant at 25 mbar, a slight expansion of the lung was observed during the measurements. This expansion may have resulted in slight deviations from the decreasing tendency of the contrast towards higher tube voltages. One exception of this tendency is a slight contrast increase in ROIs a, c, and d. The findings of the reader study show similar results as the quantitative evaluation with highest dark-field signal strength and image quality score at 60 kV to 70 kV.

During an examination by the coroner infiltrates were identified in the right lung, particularly in the lower zone. This infiltrate is visible in the dark-field images as the subjective and objective evaluation identified a reduced dark-field signal and contrast in the lower zone of the right lung, compared to the lower zone of the left lung. In the healthy left lung, the dark-field signal strength and contrast increase from the upper zone towards the lower zone. This finding is hardly surprising, considering that the lung is thinner in the upper part and therefore less air-tissue interfaces are irradiated by the corresponding X-ray beam path. A weaker dark-field signal strength in the lower right lung was found in the subjective evaluation, reflecting the clinical findings of the infiltrate.

For thicker samples it is difficult to obtain both acceptable attenuation and good dark-field radiographs. At high X-ray energies the visibility decreases, resulting in a weak dark-field signal from the lung for high-energy X-ray spectra. At low X-ray energies a low patient dose is associated with a low detector dose and therefore increase noise. As the maximum tube current of the source and therefore the maximum entrance surface dose (ESD) decreases for lower tube voltages, the lowest examined tube voltage was 60 kV. Despite these limitations, higher dose has to be applied to the patient as the attenuation increases at lower X-ray energies. However, with X-ray sources achieving acceptable ESD values at lower tube voltages, dark-field thorax imaging might be feasible. The upper limit of the examined tube voltages of 120 kV was restricted by the maximum acceleration voltage of 120 kV of the source. As the dark-field signal decreases with the energy we expect the downward trend of the signal strength and image quality with increasing energy to continue for energies above 120 kV. Furthermore, in clinical routine chest X-ray radiographs are recorded at 120 to 125 kV. Therefore, we believe a further increase of acceleration voltage to be unnecessary.

The constraints for determining optimal tube voltage are not uniquely defined. The most obvious approach would be to apply equal estimates for effective dose (ED) at every tube voltage setting. For radiography, ED can be estimated from dose-area product (DAP). However, the conversion factor between the two is dependent on tube voltage, and conversion factors for thorax radiography are, to our knowledge, not tabulated for most X-ray energies used here. It may be beneficial for future studies to estimate these factors from Monte-Carlo simulations on anthropomorphic phantoms. In this work, estimated ESD values increase with tube voltage (cf. Tab. 6.1), but increasing attenuation implies that a greater fraction of this dose is deposited in the body at lower X-ray energies.

Grating based X-ray dark-field imaging yields besides the dark-field image a perfectly registered attenuation image. Therefore, it is reasonable not only to use both images combined for diagnostics, e.g., to register structures in the dark-field image to anatomical structures but also to avoid taking another image at a conventional setup and exposing the patient to more radiation. Albeit the typically used tube voltage in conventional thoracic X-ray radiography is higher than the tube voltages deemed optimal in this study for dark-field imaging. Even though signal strength and image quality seem not to favour any tube voltage in this study, long-term clinical experience and multiple studies designate optimal tube voltage for attenuation images to be 120 kV to 130 kV [Muhogora, 2012; Ekpo, 2014]. Our setup differs from a clinical X-ray radiographic system in the additional filtering due to the gold gratings and a reduction of the amount of detected Compton scatter.

With the current state of technology different possibilities to unite X-ray dark-field imaging with classical radiography exists: one possibility would be to record the dark-field images at low energies and a separate attenuation image on a clinical radiography system with higher energies. Then, the attenuation image from the dark-field setup is only used to correlate findings in the dark-field image with anatomical structures. Moreover, the low energy attenuation image may provide similar diagnostic value to high energy attenuation images, so that it can be included in the examination and no separate attenuation image at higher voltages is needed. However, if the high energy attenuation image is not able to show the lung disease (e.g., early-stage emphysema or fibrosis) only the dark-field image may be sufficient. Furthermore, dark-field images at higher tube voltages may be acceptable despite the related loss of image quality when the attenuation images have a diagnostic quality. The choice which of the options to use depends on the additional diagnostic value of the dark-field images, whether an additional patient dose is justified if more images are taken, whether a conventional X-ray image adds to the diagnostic value, and whether the low energy attenuation image recorded with the dark-field setup has enough diagnostic value to replace the conventional image.

Our study has several limitations. The study is based on images of a cadaver instead of a living human. Performing the study on a living human was not reasonable due to the exposure to high doses. The dark-field signal strength of the cadaver was probably lower than for living humans as decomposition of the lung tissue already started when measuring the cadaver, reducing scattering air-tissue interfaces. Furthermore, the dark-field signal strength in the lung depends not only on the energy but also on the number of air-tissue interfaces, which in turn depends on patients age and health. These variations in the amount of scattering material will modify dark-field signal strength, but not their trend as a function of X-ray energy. The examined body had a normal weight with a Body-Mass-Index of 24.2 kg/m². However, the dose efficiency will likely decrease for more obese patients, as it is the case for other X-ray imaging methods [Yanch, 2009]. A possible dependence of the optimal tube voltage on the body weight has yet to be examined. In this study the optimal tube voltage was only determined for the lung regions. Nevertheless, other organs produce also a dark-field signal (e.g., the bones). There, the optimal tube voltage for imaging of osseous structures may be different from the one of the lung region. Therefore, the optimal tube voltage has to be determined for other regions in the body or applications if dark-field imaging is used in

future studies.

Signal levels and quality scores show more variation for the dark-field images compared to the attenuation images. Although all readers were experienced in dark-field imaging (cf. Sec. 6.1.2) they had naturally more experience in attenuation imaging. As a result, the inter-reader and intra-reader agreement values are lower in dark-field imaging compared to attenuation imaging. However, the values for inter- and intra-reader agreement are still high. Therefore, it seems appropriate to only have three readers for this study as there is also a high correlation. The dark-field images are rated reliably regardless of the reading session (individual or grouped reading).

Setup specific parameters such as grating material, period, and inter-grating distances also influence the value for the optimal tube voltage. The setup used in this study is an unconventional asymmetric setup with three absorption gratings. Here, the visibility spectrum is broader than the spectrum of a conventional Talbot-Lau interferometer with similar setup specific parameters. Especially the visibility for lower energies is higher in our setup. Therefore, the dependency of image quality on tube voltage might differ in another setup. Stronger dark-field signal strength for higher energies can be achieved by increasing the setup's sensitivity, which in turn can be increased by decreasing the grating period or increasing the length of the setup. However, the production of gratings with smaller periods but similar heights is difficult due to manufacturing challenges. An increase of the setup length is limited as X-ray dark-field setups used for medical purposes are required to fit into a clinical examination room. Furthermore, mechanical instabilities might increase with increasing setup length resulting in more artefacts.

To conclude, considering the results of the quantitative and subjective grading of the signal strengths and the subjective grading of the image quality, the optimal tube voltage for X-ray dark-field radiography of the human chest seems to be 60 kV to 70 kV at the used setup. Furthermore, the high attenuation image quality scores at all tube voltages indicate the possibility to use the attenuation images taken at these low tube voltages, for additional atomical structure information.

6.2 Tube voltage optimisation at the *patientscanner*

As mentioned before the optimal tube voltage might also differ for different setups. With the completion of an X-ray dark-field prototype setup for clinical thorax imaging studies (in the following called '*patientscanner*') the optimal tube voltage for X-ray dark-field thorax imaging is determined for this setup, as here a large study on patients is to be performed. The biggest difference between the *patientscanner* and the *linescanner* is the orientation of the X-ray beam and the geometry of the interferometer. Since the orientation of the X-ray beam in thorax images is horizontally to allow imaging of the patient in a upright position,

the orientation of the X-ray beam in the *patientscanner* was also chosen to be in horizontal direction. Furthermore, the gratings are arranged in an almost symmetrically configuration. For further information on the *patientscanner* see [Willer, 2018; Frank, 2021; Gassert, 2021]

6.2.1 Materials and Methodes

Image acquisition

The *patientscanner* is a clinical prototype for X-ray dark-field thoracic imaging. The source, an MRC 200 0508 ROT GS (Philips Medical Systems, Hamburg, Germany), and the detector, a Pixium FE 4343 F (Triexell, Moirans, France), are standard clinical X-ray radiography components. The setup is a three grating interferometer with a phase grating as G_1 . The patient (sample) is standing (placed) between the G_1 and G_2 . The effective field of view in the sample plane is $37\text{ cm} \times 37\text{ cm}$. Similar to the *linescanner*, the gratings do not cover the complete detector area, therefore, the interferometer is moved in vertical direction to be able to image the complete field of view. The extraction of dark-field and attenuation images is similar to the method described in Sec. 5.2.2. Furthermore, the attenuation images are processed with a similar algorithm as conventional radiographs employing histogram equalisation and structural enhancement.

The study was performed on a Multipurpose Chest Phantom N1 ‘Lungman’ (Kyoto Kagaku, Kyoto, Japan). It is a standard phantom for thoracic radiography. However, the original lung inserts do not generate a dark-field signal, therefore these inserts were removed and the voids were filled with cotton wool. Furthermore, the bone material used in the phantom produces a stronger dark-field signal compared to real bones.

Images were acquired with tube voltages ranging from 50 kV to 120 kV in 10 kV steps and one image at the maximal tube voltage of 125 kV. The tube current was chosen to achieve a constant dose area product of $30\text{ }\mu\text{Gym}^2$ for all images.

Reader study

The same three blinded readers as the for the previous study (cf. Sec. 6.1) evaluated attenuation and dark-field images. Although all readers have experience with X-ray dark-field imaging and have participated in previous studies, they received training to familiarise with images of the phantom, as it was not used in previous studies.

Each reader performed two reading sessions with at least two weeks in between each session. In all sessions, all images within one modality were shown simultaneously for a better comparability and to be able to identify small differences. Same window and level were applied for all images in one modality, independent of tube voltage. In each session the signal strength and image quality were evaluated for dark-field images and attenuation images on

a six-point scale. The point scale was the same as in the previous study: the point scale for the dark-field signal strength ranges from no signal (1) to high signal (6) and for attenuation signal strength in ranges from complete consolidation with no lung visible (1) to normal lung (6). The point scale for image quality was identical for dark-field and attenuation images, ranging from not diagnostic (1) to excellent (6) (in detail: 1: not diagnostic, 2: sufficient, 3: satisfactory, 4: good, 5: very good, 6: excellent). The scores were taken in six zones of the lung: both left and right lung were divided in upper, middle, and lower zone.

Statistical analysis

Statistical analysis was performed with the packages `numpy` [Harris, 2020] and `scipy` [Virtanen, 2020] of the programming language `python`. Inter- and intra-reader correlations were calculated with Spearman's ρ . No agreement is indicated by values < 0 . Values of $0 - 0.20$ indicate a slight, $0.21 - 0.40$ a fair, $0.41 - 0.60$ a moderate, $0.61 - 0.80$ a substantial, and $0.81 - 1$ an almost perfect agreement.

Quantitative evaluation of dark-field signal

For quantitative evaluation six ROIs, one in each lung zone, and one ROI in the vicinity of the lung were selected. Each ROI has a size of 30×30 px, corresponding to $12 \text{ mm} \times 12 \text{ mm}$ in the sample plane. The size and position of each ROI was chosen in such a way to exclude the ribs. As the images were taken continuously, without moving the sample in between two images, each ROI consist of the same region for all measured images. For each ROI the mean $\mathfrak{M}_{r,U}$, standard deviation $\Sigma_{r,U}$, and contrast C was calculated for every tube voltage $U = 60, 70, \dots, 120 \text{ kV}$ as in Eq. (6.1) and Eq. (6.2). The contrast to noise ratio CNR was calculated using:

$$CNR_{i,U} = \frac{C_{i,U}}{\Sigma_{i,U}^{(C)}}; \quad (i = a, \dots, f). \quad (6.3)$$

6.2.2 Results

The dark-field and attenuation images are shown in Fig. 6.6 and Fig. 6.7. These images were the basis on which the readers scored the signal strength and image quality. The signal strength scores are depicted in Fig. 6.8 a) and b). The score is represented as the median (orange bar), the 25th and 75th percentile (light blue box), and the minimal and maximal value (error bars). The signal strength of the dark-field was scored highest with a median score of 6 for a tube voltage of 50 kV. Towards higher tube voltages the median signal strength score for dark-field decreases to a score of 2 at 125 kV. In the attenuation images a reverse trend is visible: The lowest median signal strength score of 4 was assigned to images taken at 50 kV and 60 kV. Towards higher energies the median signal strength score increases

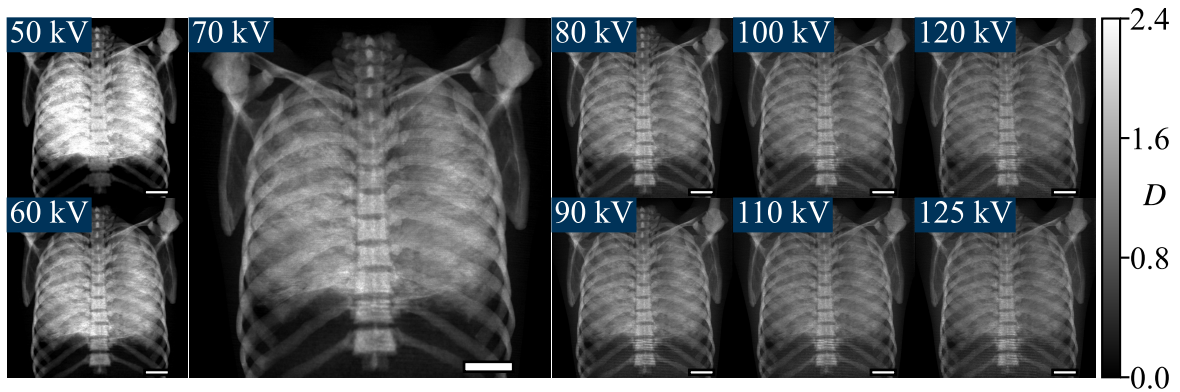


Figure 6.6: Dark-field images of the thorax phantom at the examined tube voltages. All images are shown in the same windowing. The scale bar in the lower right corner has the size $5\text{ cm} \times 1\text{ cm}$. The dark-field signal is found to be highest at the lower tube voltages. Image quality decreased towards higher tube voltages.

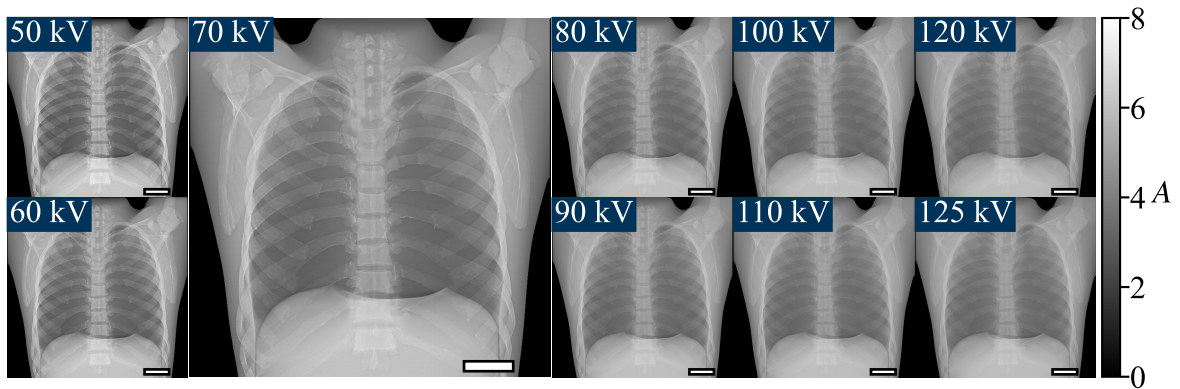


Figure 6.7: Attenuation radiographs of the thorax phantom at the examined tube voltages. All images are shown in the same windowing. The scale bar in the lower right corner has the size $5\text{ cm} \times 1\text{ cm}$.

to a value of 6 at 110 kV to 125 kV. The results of the reader study concerning the image quality is depicted in Fig. 6.8 c) and d). The same representation as for the signal strength score is used. Highest median image quality score for the dark-field images is achieved at tube voltages of 50 kV, 70 kV, and 80 kV. The score decreases towards higher energies to a minimum score of five. However, the lowest scores assigned in the images taken at 70 kV and 80 kV is five, whereas the lowest score in the image taken at 50 kV is three. For the attenuation images, the best image quality was achieved in the images taken at 110 kV and 120 kV. Here, all readers assigned a score of six to all lung zones. The lowest median score of 4.5 was assigned to the image taken at 50 kV.

In Tab. 6.3 the inter-reader agreement and the agreement between the two reading sessions of one reader is shown. The agreement between two reading sessions is almost perfect for all readers for the signal strength of both modalities. Also, the inter-reader agreement of the scored signal strengths of the dark-field is almost perfect between all readers. The agreement

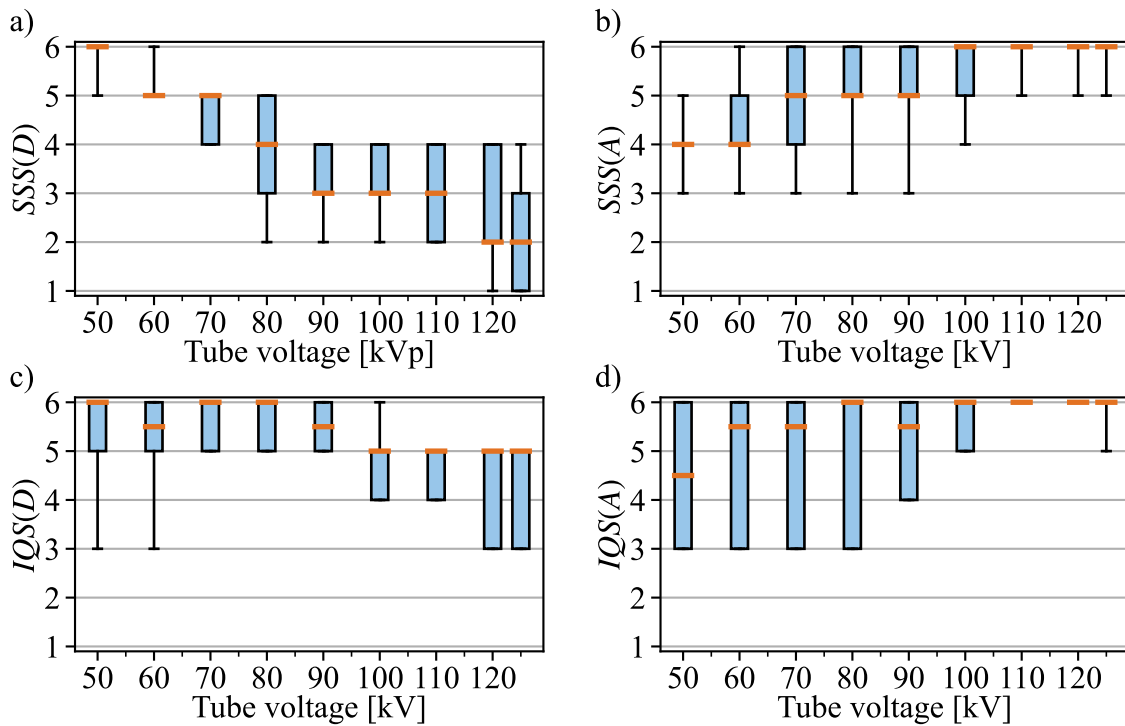


Figure 6.8: Signal strength score (SSS) (dark-field a and attenuation b) and image quality score (IQS) (dark-field c and attenuation d) at the examined tube voltages. The scores are represented as median (orange bar), 25th and 75th percentile (light blue box), and minimal and maximal value (error bars). In attenuation images, a slight increase of the signal strength score towards higher tube voltages is visible. Signal strength score decreases distinctly towards higher tube voltages in dark-field images. A slight increase of the image quality score is visible for attenuation images. In dark-field images, the signal strength score has a maximum at tube voltages of 70 kV to 80 kV.

	Signal strength		Image quality	
	Dark-field	Attenuation	Dark-field	Attenuation
Inter-reader agreement (combined from both reading sessions)				
Readers 1 and 2	0.885	0.710	0.625	0.659
Readers 1 and 3	0.810	0.884	0.582	0.564
Readers 2 and 3	0.882	0.592	0.605	0.498
Agreement between the two reading sessions				
Reader 1	0.869	0.889	0.852	1.000
Reader 2	1.000	0.885	0.741	0.494
Reader 3	0.996	N/A	0.560	1.000

Table 6.3: Inter-reader agreement and agreement between two reading sessions. Agreement was calculated with Spearman's rho. Values of 0.21-0.40 were considered as fair, 0.41-0.60 as moderate 0.61-0.80 as substantial, and 0.81-1 as almost perfect. Values for the signal strength of the attenuation images are missing for the 2nd reading of the 3rd reader, therefore, an agreement between the two reading sessions could here not be determined and is indicated with N/A.

between the reader on the signal strength score for the attenuation images is moderate to almost perfect. The inter-reader agreement for image quality was moderate to substantial in both image modalities. A moderate to almost perfect agreement between two reading sessions were found for the image quality of all modalities.

Fig. 6.9 shows mean contrast and mean CNR of the quantitative evaluation for different tube voltages. The highest mean contrast was found for a tube voltage of 50 kV. Towards higher tube voltages the mean contrast decreases. Highest mean CNR was achieved in the image taken with a tube voltage of 70 kV.

6.2.3 Discussion

In the current study dark-field and attenuation images of a lung phantom at different tube voltages but constant dose area product was acquired. Quantitative evaluation showed highest dark-field contrast for images taken with a tube voltage of 50 kV. Also, in subjective evaluation the highest dark-field signal strength score was awarded to the image taken at tube voltages of 50 kV. As the dark-field signal decreases with energy, highest dark-field contrast and signal strength score at low tube voltages is an expected result. Despite the lower signal strength score and contrast, highest dark-field image quality score and CNR was found in the images taken with tube voltages of 70 kV to 80 kV.

The results for the attenuation images are the opposite of those for the dark-field images. Highest image quality score in the attenuation images was found for high tube voltages of 100 kV to 125 kV. However, high median image quality scores of 5.5 to 6 was awarded to images taken at tube voltages of 60 kV to 80 kV. Also, at these tube voltages a high median

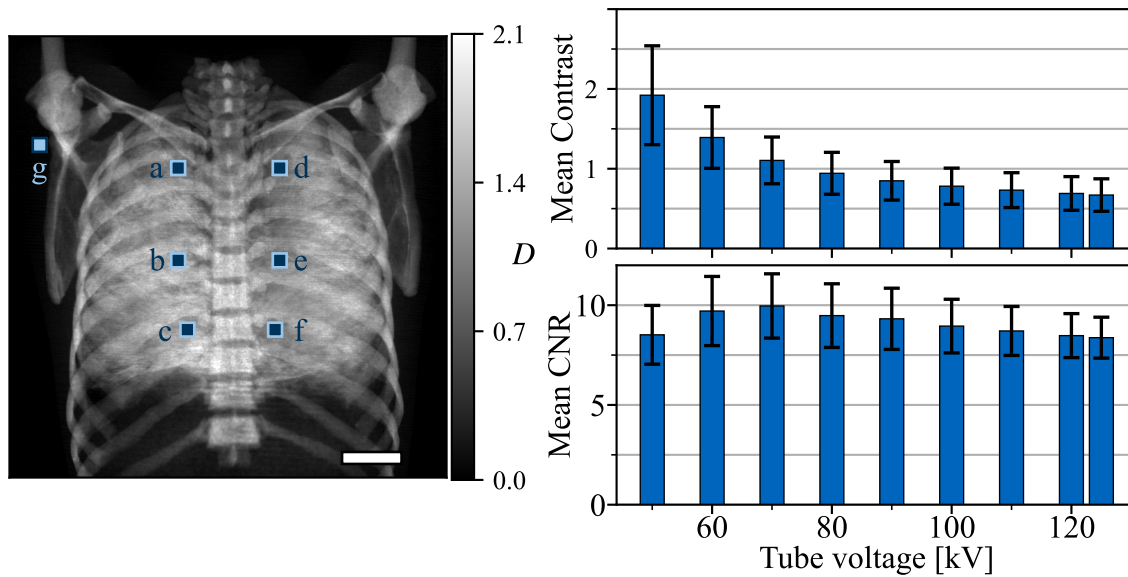


Figure 6.9: Mean dark-field contrast (top, right) over the six ROIs within the lung (a-f) with respect to the ROI in the background (g) and the mean CNR (bottom, right). The positions of the ROIs are indicated in the image on the left. The mean contrast decreases towards higher tube voltages. The highest CNR is achieved at tube voltages of 60 kV to 70 kV.

signal strength score of five was found.

The range of tube voltages to acquire images with good image quality in the attenuation and dark-field modality is narrow. As studies have shown, for conventional thorax imaging higher tube voltages are favourable [Muhogora, 2012; Ekpo, 2014]. However, for dark-field imaging lower tube voltages are needed to achieve a high signal and good image quality. Combining all results of this study a tube voltage of 70 kV seems to provide the best combination of dark-field and attenuation images at the same time. Thus, this tube voltage enables the evaluation of both image modalities at the same time.

Performing the current study as an in-vivo study is not feasible as it would result in a increased dose that is not justified for the patient. Furthermore, the beam travels though the patient in horizontal direction, making it not possible to perform the studies on deceased human bodies as they would not remain in an upright position.

This study as some limitations, which will be addressed in the following. Dark-field imaging is not yet an established imaging technique in clinical routine. This could lead to a misinterpretation from the readers of the dark-field images. However, all readers are familiar with dark-field imaging and have participated in numerous other studies. Furthermore, an overall good inter-reader agreement and agreement between reading sessions were achieved. Moreover, the result of the subjective and objective analysis provided similar results. Therefore, we are convinced that the results of the reader study are reliable. Although the used

phantom is a standard phantom for conventional radiography and thus delivers similar attenuation images as a real human thorax, this is not the case for the dark-field images. The used phantom was a standardised lung phantom for conventional radiography. However, the originally present artificial lung tissue did not deliver a dark-field signal. Finding a suitable dark-field phantom material for the lung is difficult. Such a material should have the same microstructural shape and size, and the same electron density. However, even an ex-vivo lung does not resemble an in-vivo lung perfectly, as it starts to decompose and thus the microstructure of the lung is changed. As the main interest in this study was on the relative change of the dark-field signal with respect to different tube voltages and not the absolute dark-field signal strengths, it is sufficient for this study to use cotton wool as a phantom material. To reduce the influence of features from the cotton wool, only uncorrelated noise of the images was used for the CNR analysis. This uncorrelated noise corresponds not necessarily to the intrinsic image noise. However, it is a very good approximation. Furthermore, the bone-material of the phantom does generate an increased dark-field signal than real bones. To reduce the effect of the dark-field signal of bone substitutes on the quantitative evaluation, the bony structures were excluded from the ROIs. The image quality and CNR might be influenced by the amount of fat in the thorax region. The ‘Lungman’ phantom models a person with a body mass index of 23 kg/m^2 . Additional fat in the thorax region absorbs lower energy X-rays stronger than higher energy X-rays, resulting in increased noise at lower energies. This might shift highest image quality score and CNR towards higher energies. Furthermore, the dark-field signal not only depends on the material and tube voltage but also on setup specific parameters, like grating periods and inter-grating distances. As mentioned before, higher setup sensitivities and thus higher dark-field signals can be achieved by increasing the setup length or decreasing the grating period. As discussed before, decreasing the grating period is hampered by manufacturing challenges and increasing the setup length is not feasible as the setup has to fit in a clinical examination room.

In conclusion, the current study suggested an optimal tube voltage of 70 kV to 80 kV for dark-field thorax imaging at the used setup. As the used setup is a clinical prototype for dark-field thorax imaging and further studies on in-vivo human thoraxes will be performed, the current study is an important result to optimise the image acquisition and dose for the patients.

6.3 Summary

The aim of the two studies was to find the optimal tube voltage for dark-field thorax imaging. Therefore, a series of dark-field images at different tube voltages was taken at two different setups. At the *linescanner* X-ray images of the thorax of a human cadaver were taken, while at the *patientscanner* X-ray images of a lung phantom were taken. Both setups are prototype X-ray chest setups, with a different arrangement of the gratings. The *linescanner* was arranged in an asymmetric geometry with three absorption gratings. The body was imaged while lying on the back, as the X-ray beam travels in vertical direction. The *patientscanner*

has an almost symmetric geometry with a phase grating as the modulation grating. Here, the patient is standing in an upright position during the measurement, as in conventional X-ray thorax imaging.

Highest dark-field signal strength and contrast was found in both studies at the images acquired at the lowest measured tube voltages, i.e., 60 kV in the study at the *linescanner* and 50 kV in the study at the *patientscanner*. According to the subjective evaluation highest image quality was achieved in images taken at 60 kV to 70 kV and at 70 kV to 80 kV at the *linescanner* and *patientscanner*, respectively. At both setups the highest CNR in the dark-field images was measured in the image taken at 70 kV. From these results we can conclude that dark-field thorax images should be taken at low tube voltages of 60 kV to 80 kV to achieve a best possible image. Nevertheless, highest signal strength and image quality in the attenuation images were found in both studies in images taken at high tube voltages. This is in accordance with previous studies, where the optimal tube voltage for conventional X-ray chest radiography was found to be 120 kV to 130 kV [Muhogora, 2012; Ekpo, 2014]. However, in both here preformed studies the signal strength score for high tube voltages is only one to two points higher than at tube voltages of 60 kV to 80 kV. The difference in image quality score is even lower, with the score for high energies being 0.5 to 1 points higher than for the low energies. Therefore, the attenuation image can be used for correlating findings in the dark-field images with anatomical structures.

7 Whole-body X-ray dark-field radiography of a human cadaver

Many applications for dark-field imaging were found as part of basic research, non-destructive testing, and medical diagnostics [Donath, 2009; Prade, 2015; Braig, 2018]. In medical X-ray dark-field imaging, the lung is of special interest as it generates a strong scattering signal due to the many air-tissue interfaces of the alveoli [Bech, 2013]. Many small animal studies on the structural change of the lung parenchyma due to pulmonary diseases were conducted, assessing significant potential of X-ray dark-field imaging for the detection of structural pulmonary diseases [Schleede, 2012; Meinel, 2014; Yaroshenko, 2015; Hellbach, 2016; Scherer, 2017; Umkehrer, 2020]. With the development of the *linescanner*, X-ray dark-field thorax imaging of larger animals and human bodies are possible [Gromann, 2017; Willer, 2018]. Besides the lung, also the internal structure of the bones or micro-calcification in the breast generate a dark-field signal [Baum, 2015; Eggl, 2015]. A study presenting full body X-ray dark-field and attenuation images of an euthanized pig, found strong dark-field signal in the lung as well as in some skeleton structures [Hauke, 2018]. In the following study, attenuation and dark-field images covering the majority of a human body are presented. Signal strength of both radiography modalities in different body regions are discussed as well as the detectability of anomalies. Furthermore, the effect of beam hardening and small angle scattering on the dark-field signal is examined.

The findings in this chapter were published in *Whole-body x-ray dark-field radiography of a human cadaver* [Andrejewski, 2021a]. Figures and text passage in this chapter may appear identical to the publication. My primary contribution to this study was performing the beam hardening measurements and data analysis.

7.1 Methods

7.1.1 Imaging setup

The used setup for the following study is the *linescanner* in configuration 1 (cf. Sec. 5.1). Attenuation and dark-field images were calculated using Eq. (5.1) to (5.3) and Eq. (3.13) to (3.14). To correct for beam hardening effects on the dark-field signal the correction method of Sec. 5.2.3 was used. In the object plane, 10 cm above the sample table, an effective field of view of 35 cm × 35 cm was achieved. Six individual scans were combined to form the radiographs of the whole human body, leading to a total imaged area of 177 cm × 30 cm in

the patient plane. To acquire those images, the body was placed on the motorised sample table. The scan range was selected by adjusting the table position before each scan. As the range of the table was not enough to measure the whole human body, the body had to be rotated by 180° between the scans of the upper and lower body.

7.1.2 Human cadaver and dose estimation

The radiographs for the whole-body images were acquired four days post mortem from a 62-year-old female body, with a weight of 49 kg and a height of 162 cm. The lungs were ventilated with a respirator (Fabius Tiro, Drägerwerk AG & Co. KGaA, Lübeck, Germany) with a constant pressure of 18 mbar. The experiment was conducted according to the declaration of Helsinki and was approved by the institutional review board (Ethikkommission der Ludwig-Maximilians-Universität München, Pettenkoferstr. 8a, 80336 Munich, Germany).

The ED was calculated using Eq. (2.31) and conversion factors given in [Wall, 2011]. Therefore, the DAP was estimated from incident air KERMA, measured with a PTW NOMEX dosimeter (PTW, Freiburg, Germany), and the area of the organs.

7.1.3 Beam hardening measurements

For the investigation of the beam hardening effect on the dark-field signal, dark-field and attenuation signals for different heights of phantom materials, neoprene, aluminium, and POM, and an ex-situ pig lung from a local butcher were measured. The measured heights of the phantom material were: 1, 2, 4, 8, and 16 mm of aluminium, 3, 5, 7, 9, and 11 cm of POM, and 1, 2, 3, 4 cm of neoprene. The attenuation and dark-field signal of the phantom material were calculated for each height from the mean signal in a ROI of 22 mm × 47 mm. The ex-situ pig lung was ventilated with a pressure of 25 mbar and depicted in a 2D histogram, where the brightness of the colour correlates with the number of pixels having the corresponding combination of attenuation and dark-field values.

7.2 Results

The full-body attenuation and corrected dark-field images are shown in Fig. 7.1. These images were combined from six individual scans. In Fig. 7.2 and 7.3 attenuation, corrected dark-field and CT images of the hip and thigh region are shown. The windowing in the attenuation and corrected dark-field images is narrower compared to Fig. 7.1 to highlight features in these regions.

A rough estimation of the ED for different organs is shown in Tab. 7.1. For comparison,

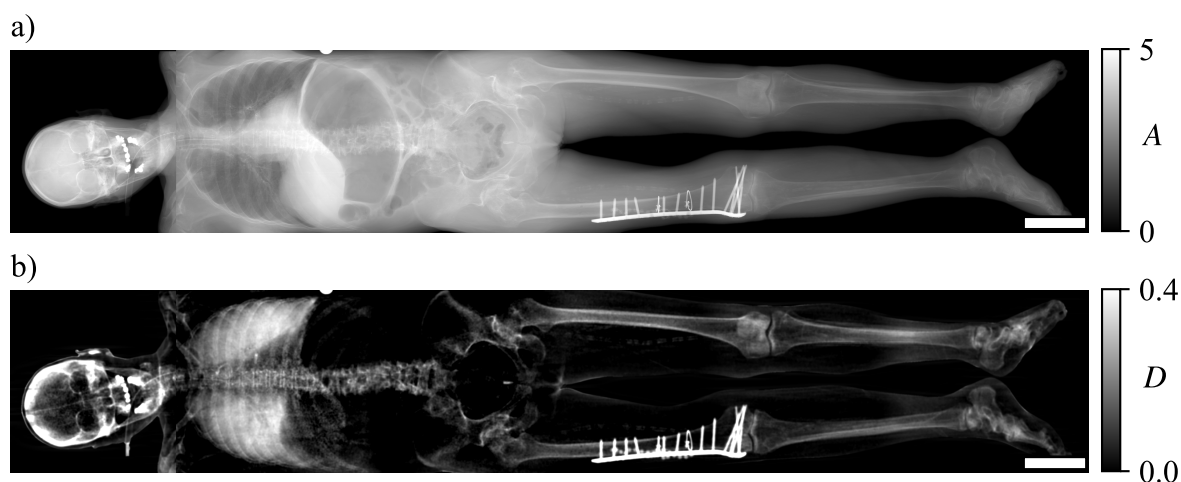


Figure 7.1: Attenuation (a) and dark-field (b) radiographs of the human body excluding the arms. The scale bar in the lower right corner has the size $10\text{ cm} \times 2\text{ cm}$. Images were taken in recumbent anteroposterior position with the right side of the body displayed on the left side of the image. A correction for beam hardening effects on the dark-field images was applied.

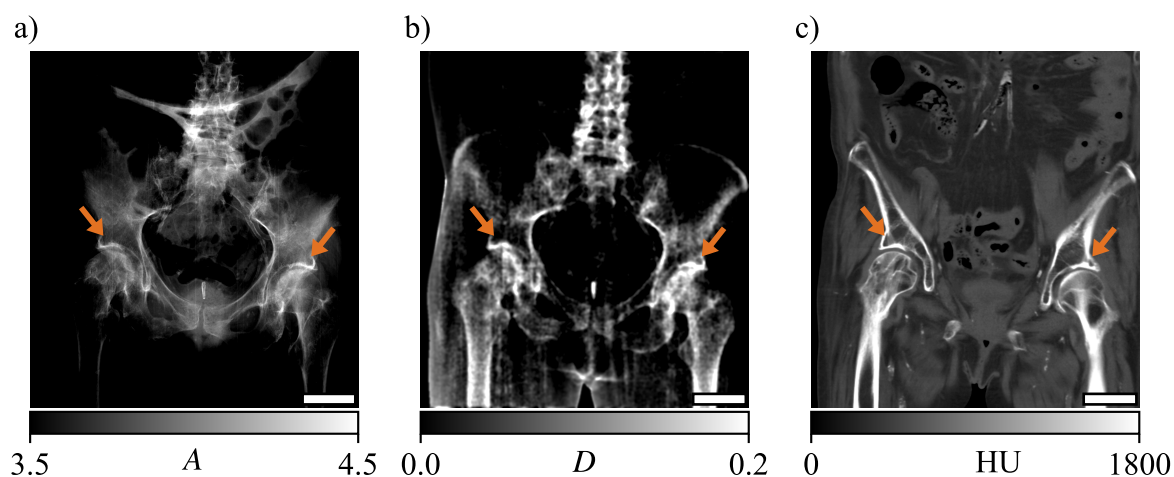


Figure 7.2: Attenuation (a), dark-field radiographs (b) and coronal CT slice (c) of the pelvic region. The scale bar in the lower right corner has the size $5\text{ cm} \times 1\text{ cm}$. An area with subchondral sclerosis as a cause of bilateral osteoarthritis of the hips are marked with orange arrows. In these areas, an increased signal in both radiographic modalities is present. The signal in the attenuation image originates from a thickening of the bone structure. The dark-field signal is caused by beam hardening effects as well as increased small-angle scatter.

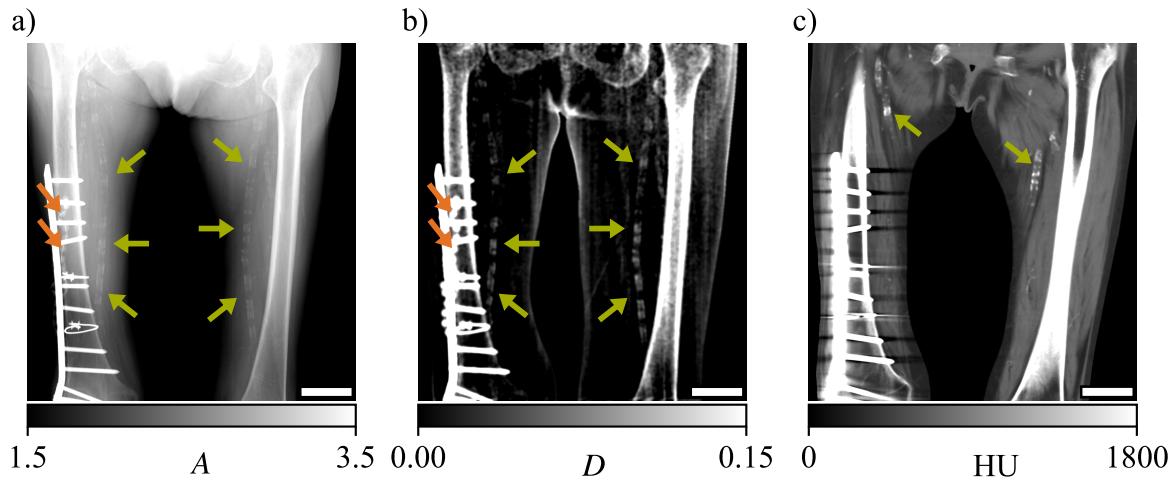


Figure 7.3: Attenuation (a), dark-field radiographs (b) and coronal CT slice of the upper legs. The scale bar in the lower right corner has the size $5\text{ cm} \times 1\text{ cm}$. In all three modalities, the metal screws and plate on the right femur, a fixation of an old fracture, are visible. The antibiotic bead chain, visible in both radiographic modalities, is indicated by the orange arrows. The green arrows indicate calcifications within the superficial femoral arteries.

Organ	ED [mSv]	typical ED [mSv]	ED/typical ED
Head, AP	0.034	0.033	1.03
Chest, PA	0.268	0.014	19.14
Abdomen, AP	0.30	0.43	0.70
Pelvis, AP	0.22	0.28	0.79
Femur, AP	0.051	0.011	4.64
Knee, AP	0.0040	0.0001	40.00
Feet, oblique	0.0024	0.0001	24.00

Table 7.1: Effective dose estimation of different organs, as well as their typical effective dose values.

reference values as given in [Wall, 2011] of the ED are also listed as well as the ratio of the calculated ED in the study to the reference ED. In our study, the ED in the chest, knee, and feet region was substantially higher compared to the reference values. The ED of the head, abdomen, and pelvis region was comparable to the reference ED.

The attenuation image shows a high transparency of the inflated lung. Furthermore, the lung also exhibits a strong dark-field signal with the highest signal in the lower lobe of the right lung. However, in the abdominal region, a high transparency in the attenuation images but barely any signal in the dark-field images is shown. Osseous structures are visible in both attenuation and dark-field images. An increased signal can be found in both attenuation as well as dark-field in the hip joints (see Fig. 7.2). Here, anatomical change due to osteoarthritis are present. In the right leg, the result of an osteosynthesis following a fracture in the right

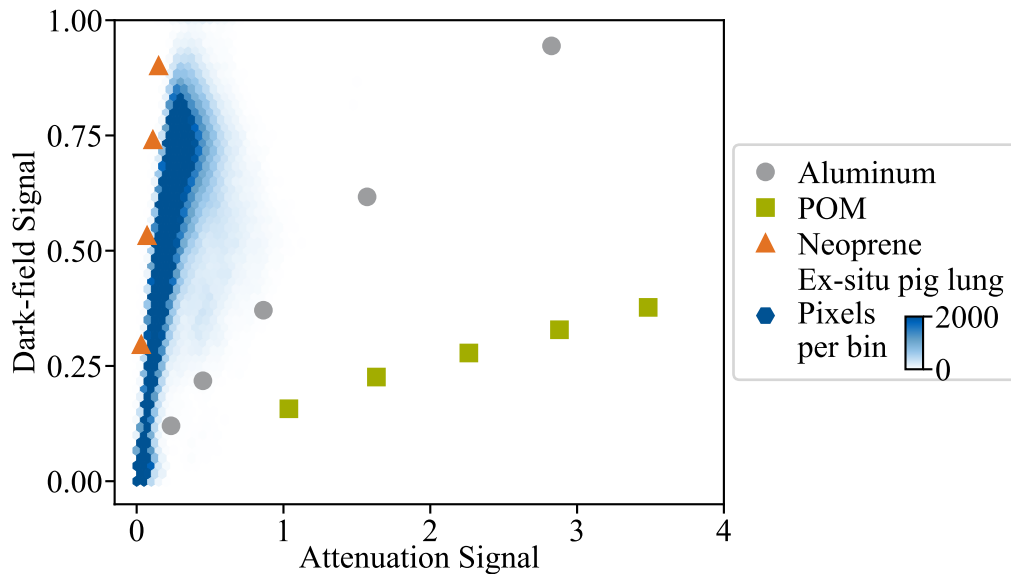


Figure 7.4: Effect of beam hardening and small-angle scatter on the X-ray dark-field signal. Measured were 1, 2, 4, 6, and 16 mm of aluminium, 2, 5, 7, 9, and 11 cm of POM, 1, 2, 3, and 4 cm of neoprene and an ex-situ pig lung. An apparent dark-field signal was generated by beam hardening in the measurements with POM and aluminium, although no scattering object was in the beam path. Aluminium and POM exhibit similar spectral attenuation properties as bone and soft tissue, respectively. The strong dark-field signal in the bones in [figs. 7.1, 7.2, and 7.3](#) despite a POM-based beam hardening correction, can be explained by the large discrepancy of the two curves here.

femur is visible (see [Fig. 7.3](#)). The fracture itself is no longer visible, which is consistent with findings from CT images, where a complete healing of the bones is visible. However, the metal screws and plate, inserted for the healing process, are visible in all three modalities. Furthermore, an antibiotic bead chain, still in-situ, can be clearly identified in the dark-field images. With respect to the vascular skeletal system, calcification of the femoral arteries in both upper legs can be detected in the attenuation, dark-field, and CT images.

In [Fig. 7.4](#), the uncorrected dark-field signal is plotted against the corresponding attenuation signal for each measured phantom material. A stronger increase of the (uncorrected) dark-field signal as a function of the attenuation signal is found for neoprene and the lung compared to POM and aluminium. The dark-field signal of POM as a function of attenuation signal increases the least of all measured materials. For POM and aluminium, the dark-field signal increases as a function of attenuation signal although both materials do not produce small-angle scatter. This increase is stronger for aluminium than for POM.

7.3 Discussion and conclusion

This study shows, to our best knowledge, the first X-ray dark-field images of a whole human body. Findings of attenuation, dark-field and CT images were compared. Dark-field signal was found in the lungs, bones, in the femoral arteries due to calcification, implants, and foreign bodies. Of all these regions the lungs produce the strongest dark-field signal.

In some organs, the ED is higher than the reference ED in the corresponding organ. Typically, only one organ/region of the body is examined in a radiograph. Therefore, imaging parameters like the tube voltage and tube current can be chosen to generate images with optimal image quality at lowest patient dose. In this study, imaging parameters were kept constant for all images/regions in the body. The tube voltage has to be selected, so that enough photons reach the detector behind the more absorbing body parts, like abdomen and head. In these regions, the ED in this study is similar to reference ED. As a consequence, the ED in less absorbing body regions is higher.

The findings in the lung region concerning the dark-field signal strength is similar to previously published studies with large animals and human cadavers [[Gromann, 2017](#); [Hauke, 2018](#); [Willer, 2018](#)]. The dark-field signal in the lung originates from many air-tissue interfaces of the alveoli in the lung parenchyma. The dark-field signal of the lung is certainly lower here than it would be in living humans. The body deceased four days prior to the image acquisition and a decomposition process already started. The lung started to collapse and the partially fluid filled alveoli destroyed the air-tissue interfaces and therefore the dark-field signal.

In contrast to the lung, barely any air-tissue interfaces or other interfaces with strong electron density change exists in the abdominal region. Therefore, little dark-field signal was detected here. However, this region exhibits a strong transparency in the attenuation image. This is due to a previously wrong intubation of the endotracheal tube for the ventilation.

The bead chain is composed of a spongy material, which acts as a substrate for the antibiotic agent. This spongy material has many interfaces of material and air and therefore generates a relatively strong dark-field signal.

Calcification is an accumulation of calcium salt and is a common disease of the arteries especially with cardiovascular risk factors. Furthermore, atherosclerosis can lead to stenosis resulting in a hypoperfusion of the affected anatomical region. This can lead, depending on the affected arteries, to coronary artery disease or peripheral artery disease. In previous studies, it was shown that micro-calcifications in the breast can be detected in X-ray dark-field images and an improvement for early breast cancer detection was achieved [[Scherer, 2016](#); [Rauch, 2020](#)]. In this study, we were able to see calcifications of the arteries in the dark-field images. However, whether dark-field imaging can improve the diagnostic value for detecting calcifications has to be determined in further studies.

Osseous structures are visible in the dark-field as well as the attenuation images. Espe-

cially areas with increased calcium content can be clearly depicted. These are, for example, subchondral sclerosis due to osteoarthritis in the hip and knee.

As it was shown in Fig. 7.4, even no-scattering materials like POM and aluminium can cause a dark-field signal. The interferometric visibility depends on grating periods and inter-grating distances as well as the spectrum of the X-ray beam. In configuration of the *lines-canner* used for this study, high visibilities for photon energies up to 40 kV were achieved. From that energy onward the visibility decreases. When measuring with energy-integrating detectors, the average visibility is calculated from the detector signal of energy-dependent visibility weighted with the detected signal from each photon energy [Yashiro, 2015]. Thus, the visibility is affected when X-rays are attenuated, especially in this case as the low energies are more attenuated than high energies. Therefore, the visibility also decreases when the X-rays are attenuated and non-scattering but strongly absorbing materials can decrease the visibility. The dark-field signal generated in this way cannot be distinguished from the real dark-field signal due to small-angle scattering. To account for such an effect, a correction method might be applied. This was done in the present study to eliminate dark-field signal due to beam hardening in soft and adipose tissue. However, as this visibility reduction is a spectral effect, the correction method only works properly if the reference material has similar spectral attenuation properties as the sample material. As soft and adipose tissue have very different spectral attenuating properties than bone, the correction method failed to properly estimate the dark-field signal due to beam hardening in the bones and a residual signal remains there. It has been shown that bones generate a real dark-field signal [Baum, 2015; Eggl, 2015]. However, the signal of the lung is much stronger than in the bones. The sensitivity in the setups measuring the bones were higher than in the setup used in this study. Therefore, the scattering signal of the bone were good visible. We assume that the dark-field signal of the bones in this study mainly results from beam hardening effects.

The main limitation of this study is that only one human body is imaged. However, this study is a proof-of-principle and was not meant to be an in-depth study. To estimate the gain of information of dark-field imaging for other organs than the lung (here many studies were already conducted) further studies need to be conducted. Furthermore, the whole-body images were acquired stitching six images together and not from one image. Also, the body had to be repositioned during the image acquisitions as the sample table could not be moved in a sufficient range. This is of course not practical for clinical imaging. However, another image acquisition procedure, where the sample and not the interferometer is moved was proposed by Seifert et al. [Seifert, 2019]. With this image acquisition, it might be possible to acquire the whole-body image with one acquisition without repositioning the sample. This image acquisition has also problems, which are discussed in Sec. 3.4.2. Lastly, the beam hardening correction was only conducted for soft and adipose tissue. Both materials have similar spectral attenuation properties and could be sampled with the same phantom material (i.e. POM). However, the spectral attenuation properties is different for bone, so the effects of beam hardening at bone could not be corrected with POM. Furthermore, in a human body not only one but several absorbing materials are present, which all have different spectral attenuation properties. As the composition of the sample of all absorbing materials is in general not known and varies over the field of view, it is not sufficient to record another

correction curve with a different phantom material. A possible solution to correct for several absorbing materials could be dual-energy imaging to calculate spectral maps of cross-section functions. Thus, make a beam hardening correction of the dark-field signal possible for more than one material. For each additional material to be corrected, another measurement of the sample is required.

To conclude, with the dark-field images of a human body, an overview over the dark-field signal strength of different organs of the human body was given. However, before dark-field imaging can be included into the clinical routine, further studies will have to be conducted. In addition to lung imaging, bone imaging and the possibility of diagnosing calcification could be of particular interest

8 Image acquisition with a moving sample

Until now, the images in this thesis have been acquired by moving the interferometer to cover the whole field of view of the detector (cf. Sec. 5.2; henceforth referred to as ‘*swing-scan*’). However, the interference pattern of a Talbot-Lau interferometer is very sensitive to small movements within the interferometer, for example the change of distances between the gratings and a torsion or tilting of the gratings. Since in configuration 1 (cf. Sec. 5.1), the G_2 is in the shadow of the absorbing G_1 , its interference pattern is less sensitive to such small movements than the interference pattern of configuration 2 and 3, where the G_2 is placed in a fractional Talbot-distance from G_1 . Moving the interferometer in a *swing-scan* without changing unintentionally the relative positions of the gratings is very difficult to achieve and artefacts might occur in the final images. Therefore, it might be beneficial to use an image acquisition method, where the interferometer is not moved and unintended relative movement between the gratings is minimised. Such a method might be, to move the sample instead of the interferometer [Kottler, 2007; Seifert, 2019]. Besides the stationary interferometer, a further advantage of this method might be that large or long samples can be imaged in one acquisition. This eliminates the necessity of stitching images together as it was done in Chap. 7. Stitching images together might lead to artefacts due to the different path of the X-ray cone beam through the sample at two different sides of the detector or due to the repositioning of the sample between separate images. To have the possibility to choose between the two different image acquisition methods, the image acquisition with a moving sample was implemented at the *linescanner* setup.

8.1 Acquisition of data

As mentioned before, the sample is moved in this acquisition method (henceforth referred to as ‘*table-scan*’). Therefore, the sample is placed on the motorised sample table, which is moved linearly during the acquisition. Like in the *swing-scan*, the source and detector remain stationary. Furthermore, the swing comprising the interferometer also remains stationary throughout the acquisition. After acceleration of the sample table, when it reaches the desired velocity, the exposure starts and the table travels with constant velocity. At the end of the pre-set scan range, the exposure stops, the sample table decelerates, and the data is saved. As it was not possible to extract the exact position of the sample table for every exposure, a constant velocity of the table after acceleration was assumed. Since the same detector area is exposed during the acquisition of the sample and the table is assumed to be homogeneous, it is sufficient to record a single stepping data set as flat field, without moving the sample

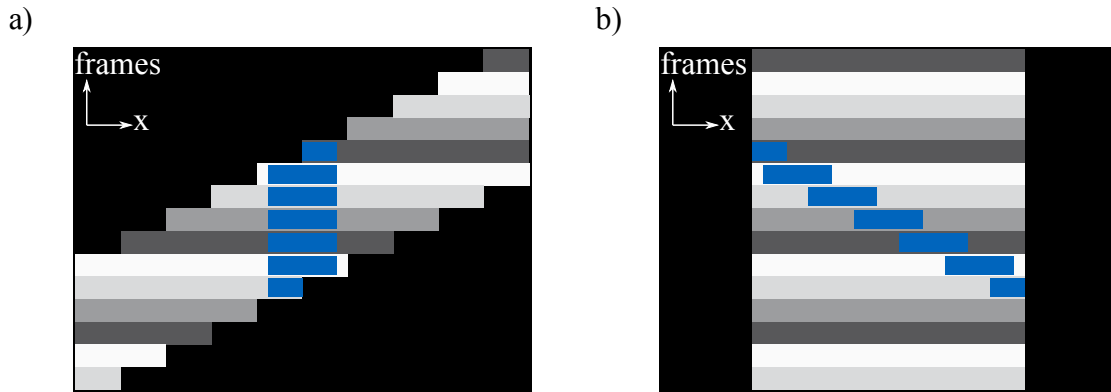


Figure 8.1: Depiction of the acquired data of a swing-scan (a) and a table-scan (b). While the sample stays stationary and exposed area moves over the detector in the swing-scan, the shadow of the sample moves through the stationary illuminated area on the detector in the table-scan.

table. A comparison of the acquired data is shown in Fig. 8.1. In Fig. 8.1 a), the image data of the *swing-scan* is depicted. Here, the sample remains at the same detector position during the scan, while the exposed area moves over the detector. For the data of the *table-scan*, depicted in Fig. 8.1 b), this is the other way round. The swing remains at the same detector position, while the shadow of the sample moves over the detector in x-direction. To achieve a similar data set to a *swing-scan* acquisition, the *table-scan* data has to be rearranged, so that the sample remains in the same x- and y-position for every frame.

8.2 Adaptation of processing

Since a different acquisition method is used, the processing also needed to be changed. The processing for the *swing-scan* was adapted for the *table-scan*. The processing for the *swing-scan* was implemented and improved by F. De Marco [De Marco, 2021] in his PhD thesis. An overview of the processing is summarised in Sec. 5.2 and an in depth description in [De Marco, 2021].

As the most difficult part of the processing is the retrieval of the mean intensity, visibility, and differential-phase, the data for the *table-scan* was resorted and rearranged to be as close as possible to the *swing-scan* data set. The workflow of the *table-scan* processing is depicted in Fig. 8.2. First, the flat-field and sample data is loaded. Since the illuminated area on the detector has the same detector pixel coordinates for every frame, a reverting of the cropped data, like in the *swing-scan* processing, is in theory not necessary. However, while saving a detector image, the cropping boundaries are calculated for every frame. Thus, they are not necessarily the same for every frame, even when the swing is not moved between to frames. This results in non-constant x-coordinates of the illuminated area in the single frames. To correct for this, the cropping is reverted after the data is loaded. To reduce occupied memory

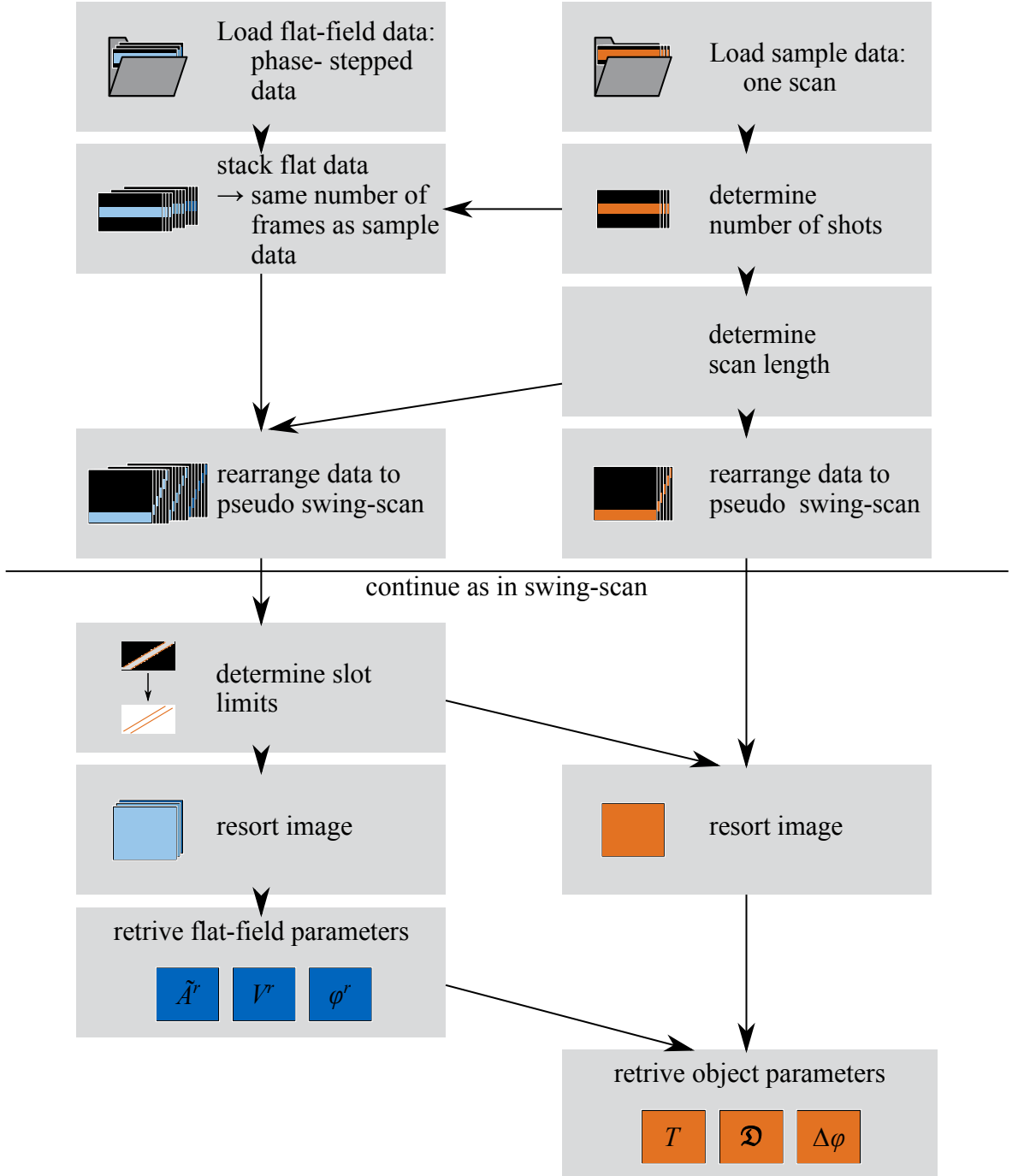


Figure 8.2: Workflow of the table-scan processing. The more computational complicated steps, as the image resorting and retrieval of the image parameters, remain the same as in the swing-scan processing (bottom half of the diagram). The new part (top half of the diagram) is a resorting of the data to achieve a similar input image as in the swing-scan. Figure adapted from [De Marco, 2021].

space and to speed up computation steps, the data is then cropped again, but this time with the same parameters for each frame. Now, the illuminated area in the frames have the same pixel coordinates, whereas in the *swing-scan* processing, x-coordinate of the illuminated area in the frame changes. Furthermore, the flat-field data of the *table-scan* consists only of one stepping data set for one table position. To imitate a flat-field with a scanned table, for each step, the same flat-field frame is stacked, so that the data of one step has the same number of frames as the sample data.

From the metadata of the sample data, the scan length, i.e., the distance the table travelled during the image acquisition, is extracted. The x-coordinate of the beginning of each frame is calculated with

$$x_i = i \cdot \frac{\text{scan length}}{\text{effective pixel size}} \cdot \frac{1}{\text{number of sample frames}}, \quad (8.1)$$

where i is a integer from 0 to number of sample frames. Those rearranged data sets are now similar to a data set of the *swing-scan*. The only difference is the number of frames and the number of pixels in x-axis. This has only an effect on the image size but not on the processing algorithm itself. Therefore, the processing of the *swing-scan* is now used to extract the image parameters: First, the limits of the exposed area are determined and then, the images are resorted. Afterwards, mean intensity, visibility, and phase of the flat-field as well as the transmission, visibility reduction, and differential-phase of the sample data is determined (for a more information see Sec. 5.2 and [De Marco, 2021]).

8.3 Samples taken with the *table-scan* acquisition

In the following, a few examples of images acquired with the *table-scan* acquisition will be presented. The first object is a phantom of POM and neoprene. A 3 cm high POM rod and a 2 cm thick neoprene slap are positioned diagonal: One end of the materials were placed on a 14 cm high POM cuboid and the other end on the sample table, where a 3 cm POM slab was placed (cf. Fig. 8.3 a)). The scan-range was 28 cm, the tube voltage 60 kV and tube current 150 mA. Furthermore, no correction for beam-hardening effects in the dark-field signal was applied. In Fig. 8.3 b), c), and d), the attenuation, dark-field and differential-phase images of the acquisition are shown, respectively. As expected, the POM parts generate a high attenuation signal, whereas the neoprene slap absorbs less X-rays. However, the two flatter POM slaps produce a low dark-field signal. As POM does not have a microstructure on which the X-rays scatter, it is assumed that the high dark-field signal generated by the 14 cm high POM cuboid is due to beam-hardening effects. Furthermore, the neoprene slap produces also a strong dark-field signal, as expected. This signal is not constant over the whole slap, but a slight gradient in vertical direction is present, with a dark-field signal of approximately 1.2 at the top and 0.8 at the bottom of the slap. The dark-field signal is not only depending on samples microstructure but also on the setup and its sensitivity. In turn, the sensitivity of a setup is not only dependent on the setup's geometry, but also on the placement of the sample within the setup. As one end of the slap is closer to the G_1 grating then the other, the

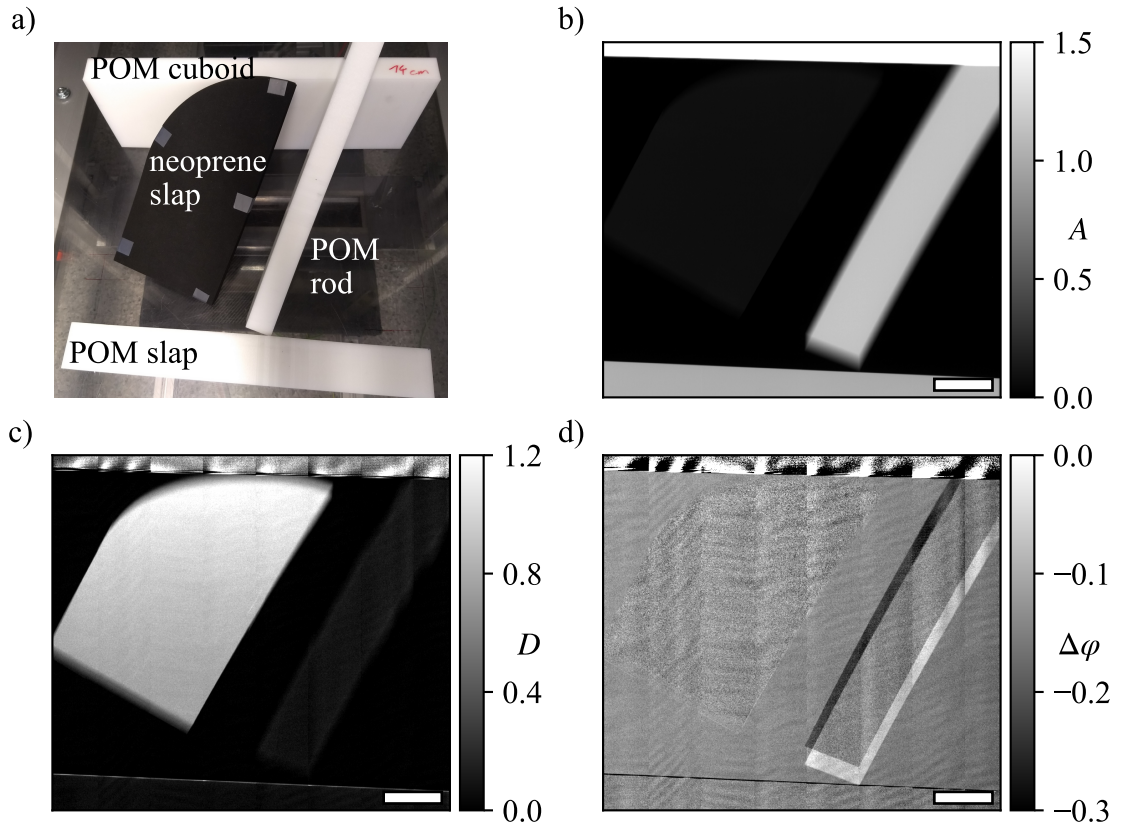


Figure 8.3: Photograph of the phantom (a), as well as attenuation (b), dark-field (c) and differential-phase (d) images of phantom material acquired with the *table-scan* method. The scale bar in the lower right corner has the size $5\text{ cm} \times 1\text{ cm}$. The phantom consist of a 2 cm thick neoprene slap and a 3 cm high POM rod, which were positioned diagonally, a 14 cm high POM cuboid, and a 3 cm thick POM slap. In the attenuation image only the POM objects are good visible. In the dark-field image the neoprene slap and the 14 cm high POM cuboid are visible. The signal from the neoprene slap originates from small angle scatter whereas the signal form the POM cuboid is generated due to beam hardening effects. In the differential-phase image the edges of the POM rod as well as phase wrapping artefacts visible.

sensitivity with which the parts of the slap are probed differs, therefore also the dark-field changes. In the differential-phase image the edges of the POM rod are clearly visible. The noise signal of the POM cuboid can be explained by a poor statistic, as most of the X-rays are absorbed. Furthermore, phase wrapping artefacts are visible.

Another sample, showing the increased field of the *table-scan*, is the sports equipment shown in fig 8.4 a). Here, a wooden baseball bat (Louisville Slugger Chicago IL, USA), a baseball (Wilson, Chicago IL, USA), and an oar blade (Concept2, Inc Morrisville, VT, USA) were radiographed. The baseball consists of yarn wound around a cork and rubber core, and is covered with leather. The oar blade consists of a polymeric foam between plastic, reinforced

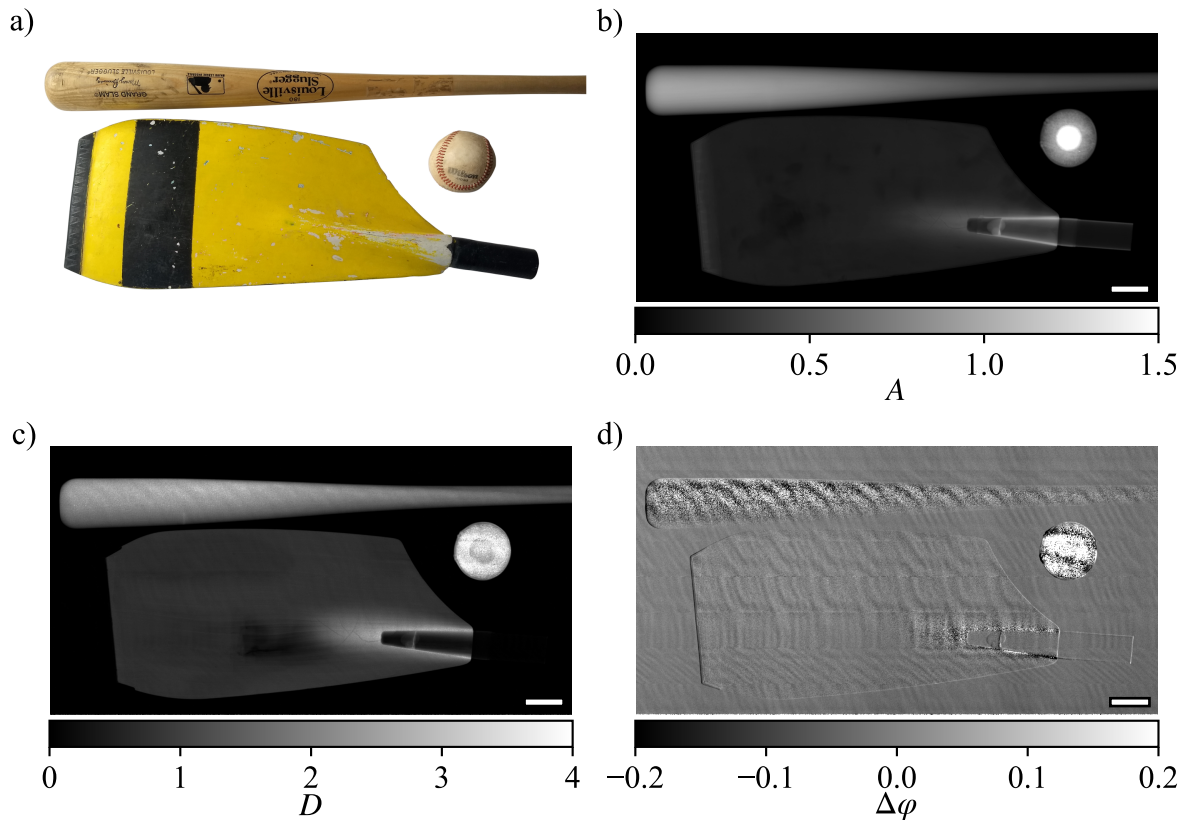


Figure 8.4: Photograph a), attenuation b), dark-field c), and differential-phase d) images of a baseball bat, a baseball and an oar blade. The scale bar in the lower right corner has the size $5\text{ cm} \times 1\text{ cm}$. As the baseball bat is a wooden bat it produces a signal in both the attenuation and dark-field image. Ball consists of a rubber core surrounded by yarn. The core generates a stronger attenuation signal than the yarn, which also produces a strong dark-field signal. The oar blade is a polymer foam between carbon fibre and fibre glass laminates, generating both attenuation and dark-field signal. In the differential phase image, the outlines of the objects are visible as well as phase wrapping artefacts.

with carbon fibre and fibreglass. The shaft also consists of carbon fibre. The scan range was 65 cm limited by the total travel range of the table. The length for the acceleration and deceleration of the table had to be subtracted from the total travel range of the table. Furthermore, the scan range is reduced by two times the width of the exposed area due to undersampling in the beginning and the end of the scan. The total scan time for the sample scan was approximately 30 s, while the acquisition of the flat-field data took 15 s. The tube voltage was set to 60 kV and the tube current to 200 mA. In the attenuation image (cf. Fig. 8.4 b)), all three objects are clearly visible. The cork and rubber core of the baseball is distinguishable from the yarn in the outer part of the ball. Furthermore, the connection between shaft and blade in the oar are clearly visible. Both the baseball bat and baseball generate a strong dark-field signal (cf. Fig. 8.4 c)). The wood from the bat was oriented with the wood fibre running along the scan direction and therefore perpendicular to the scatter sensitive direction. However, in

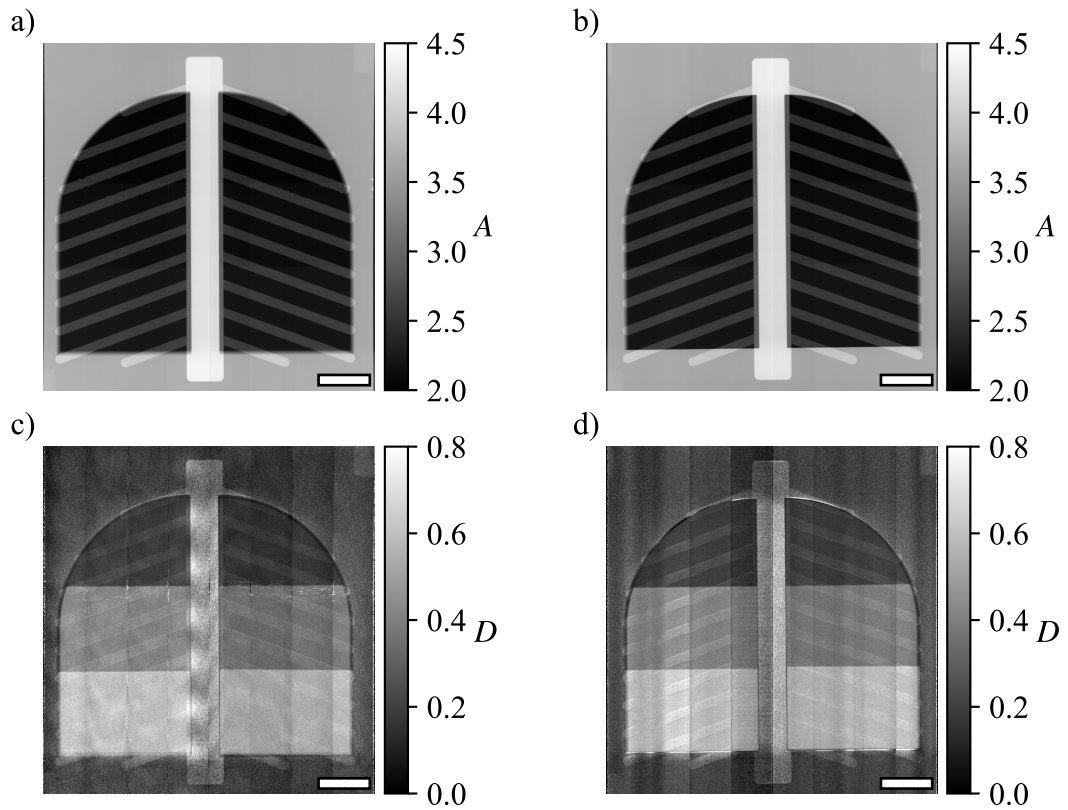


Figure 8.5: X-ray attenuation (a and b) and dark-field (c and d) images of a thorax phantom taken with the swing-scan (left) and table-scan method (right), respectively. The scale bar in the lower right corner has the size $5\text{ cm} \times 1\text{ cm}$. The attenuation images look similar. The dark-field signal strength of both modalities is also alike. However, a variation of the single is visible over the grating tiles in the dark-field image taken with the table-scan. This is not the case for the dark-field images taken with the swing-scan.

radial direction medullary rays are present in the wood, generating a dark-field signal. As no beam-hardening correction was performed on the images, part of the dark-field signal of the bat might originate from the change of spectrum due to attenuation. The very strong dark-field signal from the baseball originates mainly from the thick layer of yarn around the core. The dark-field signal of the oar blade originates from the carbon fibre and fibre glass in the laminate and the polymeric foam. Around the connection location of the shaft, a stronger dark-field signal is visible. Here, the blade is thicker and therefore, more material scattering the X-rays is present. In the centre of the blade, a spot with less dark-field signal is visible. This might indicate an imperfection or destruction of the polymeric foam and laminate. In the differential-phase image (cf. Fig. 8.4 d)), the outlines of the objects are visible. Furthermore, the strong dark-field signal especially in the baseball but also in the baseball bat leads to a destruction of the interference pattern and therefore, leads to a random phase signal.

The last sample is a basic thorax phantom for X-ray dark-field radiography. Here, the human thorax was modelled using POM as a substitute for soft tissue and fat, aluminium was used

as phantom material for bone and the lung was substituted with neoprene foam. In the centre of the thorax phantom, a 1 cm thick aluminium bar represents the backbone of the thorax. The 0.5 cm thick aluminium rods branching off from the bar represent the ribs. This bone phantom is surrounded by a 1 cm thick POM slab. For the lung region, a lung shape was cut out of 1 cm thick POM slabs and filled with different heights of neoprene. Five more 1 cm thick POM slabs were added to represent the fat and soft tissue in the thorax region. To be able to compare the *table-scan* with the *swing-scan*, the thorax phantom was imaged with both acquisition methods with the same acquisition parameters: The tube voltage was 60 kV and the tube current 600 mA. In Fig. 8.5, a comparison of the attenuation (a) and (b) and the dark-field (c) and (d) images of the thorax phantom taken with the *swing-* and the *table-scan* are shown, respectively. The transmission images are quite identical with similar signal strengths. The parts representing the bones and shoulder have a high attenuation signal, whereas more X-ray reach the detector behind the lung-region. Also, the dark-field images look similar at a first glance. The dark-field signal of the shoulder and bone regions is due to beam-hardening effects, as here no scattering material is present in the beam path. In the lung region, the dark-field signal strength increases with increasing neoprene thickness. In the image of the *table-scan* method, a change of dark-field signal over the grating tiles is visible. In the image of the *swing-scan* such change of the background dark-field signal is not visible. Here, the signal is more constant over the different grating tiles. Even though similar dark-field to the *swing-scan* acquisition can be acquired with the *table-scan* acquisition, artefacts occur which will be addressed in the following section.

8.4 Problems with the *table-scan* acquisition

Looking at all presented transmission images of the *table-scan* acquisition, no apparent artefacts were visible. Also, similar transmission images can be acquired with the *table-* and the *swing-scan*. Even though with the *table-scan* method, good dark-field images can be generated, there are still some artefacts in these images. As mentioned before, in Fig. 8.5 d) a change of the dark-field signal over the grating tiles is visible. Although, the visibility is not constant over the whole exposed area, this should not influence the dark-field signal as the flat-field should correct for such a change of the visibility. As this effect is only visible in the image with the thorax phantom, where a lot of absorbing material is in the beam path, this suggests that these changes of dark-field signal over the grating tiles might be due to beam hardening effects.

Another artefact is visible in Fig. 8.6 a). Here, the dark-field image of Fig. 8.3 is depicted again in a narrower windowing to make the background signal better visible. Here, the dark-field background signal is not homogeneous but has a periodic artefact resembling the fringes. Even though, the swing was not moved during acquisition, it was not fixed in a rigid frame. Therefore, vibrations of the interferometer might be possible during the acquisitions and might cause these artefacts. These artefacts are also visible in the differential-phase images shown in Sec. 8.3.

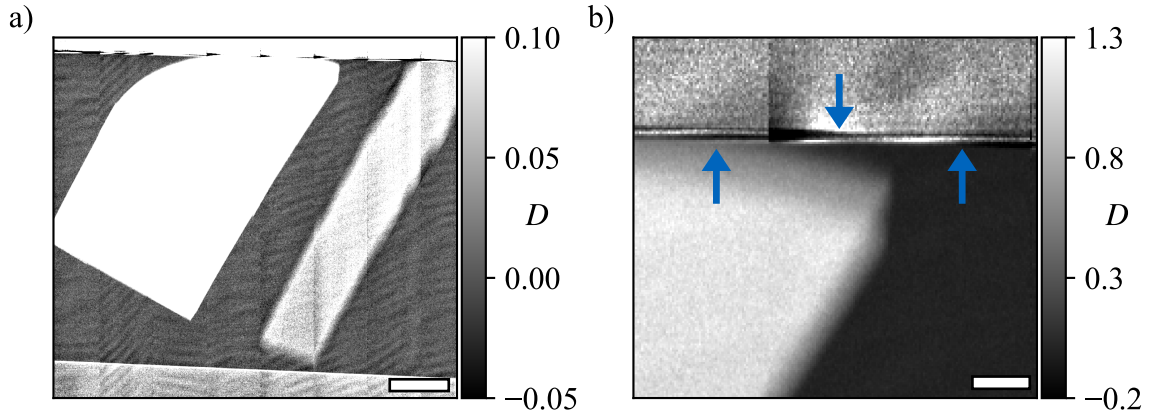


Figure 8.6: X-ray dark-field images of the phantom material (cf. Fig. 8.3) in a different windowing (a) and in a selected ROI (b). The scale bar in the lower right corner has the size $5\text{ cm} \times 1\text{ cm}$ and $10\text{ mm} \times 2\text{ mm}$ for (a) and (b), respectively. Artefacts occurring in images taken with the table-scan are visible. In (a) a relatively narrow windowing was chosen to make the periodically artefacts in the background better visible. In (b) the edge of the POM cuboid (indicated by the blue arrows) is enlarged, making the artefacts in the edge due to the different X-ray paths through the sample because of the cone beam.

As mentioned in Sec. 3.4, the *table-scan* acquisition method has a major drawback to a *swing-scan* method: Namely, that the X-rays do not travel a sample voxel in the same way during the acquisition. This effect is especially dominant for thicker samples with sharp edges as it can be seen in Fig. 8.6 b). While the sample travels through the cone beam, a feature that is high above the sample table is imaged onto different detector pixels than a feature lying directly under the upper feature. Hence, only one of the features (e.g., the lower feature) can be resorted to the same pixel in the x-coordinate in the image stack, the other feature (e.g., the upper feature) appears then in several pixels in the x-coordinate for different shots. In the processed transmission image, this leads to a blurring of the upper feature. Furthermore, after the resorting, the information obtained from imaging the upper feature with different moiré fringe phases are projected to different pixels and superimposed with the information of other features underneath. Thus, the stepping curve does not have a sinusoidal form anymore, which leads to artefacts at the edges. This effect depends also on the width of the illuminated area. The narrower the exposed area, the smaller the beam divergence. Hence, artefacts due to different paths of the X-ray beam through the sample decrease.

All in all, the *table-scan* method is usable to acquire dark-field images. This was to be expected, since such an acquisition scheme has already been presented [Kottler, 2007; Seifert, 2019]. However, the images still exhibit some artefacts, which need to be examined in greater detail to be able to reduce them. The artefacts on sharp edges could be reduced by reducing the width of the illuminated area and thus reduce the divergence of the effective beam. Furthermore, to reduce the periodic artefacts in the background it

might be sufficient to fix the interferometer in a rigid frame. However, if then still those artefacts occur, closer look at vibrations within the setup has to be taken. Nevertheless, the *table-scan* method has some advantages over the *swing-scan* method. Every movement within the setup (e.g., interferometer movement or sample movement) causes vibrations. If the gratings period is smaller than the effective pixels size of the detector, vibrations of the interferometer have a greater influence on the image quality than vibrations of the sample. As only the sample but not the interferometer is moved during the *table-scan* acquisition artefacts due to vibrations can be reduced. Furthermore, the image size is not limited by the detector size but by the movement range of the sample table. It is easier to increase the sample table movement range than the detector size, making an increase of the image size simpler.

9 X-ray vector radiography at the *linescanner*

As mentioned in Sec. 3.5, most X-ray dark-field imaging setups record the scattering ability of a probe only in one direction, i.e., perpendicular to the grating lamellas. However, by rotating the sample or the interferometer around the optical axis of such a setup, the two-dimensional scattering abilities of the sample can be calculated in the so-called X-ray vector radiography (XVR). Thus, it is possible to obtain information about the orientation of a sample's sub-pixel microstructure. One of the first acquired XVR-images show a strawberry leaf, a chicken bone, polypropylene fibres, and a human tooth [Jensen, 2010a; Jensen, 2010b]. Moreover, for laboratory X-ray sources a sinusoidal dependency of the dark-field signal on the orientation of the probe to the grating was proposed. A full period of the sine is achieved if the sample is rotated by 180° . From this dependency the mean dark-field signal, the degree of anisotropy and the orientation of scattering structures can be derived [Revol, 2012; Malecki, 2013]. The clinical potential of this method was shown by the analysis of the XVR-images of bone samples [Potdevin, 2012; Schaff, 2014; Baum, 2015; Eggl, 2015]. All these studies examined relatively small samples, with a size of a few cubic centimetres. A larger sample imaged with XVR was a human cadaver hand [Jud, 2017]. However, the field of view was smaller than the hand and therefore the dark-field images had to be stitched together from several images of parts of the hand. Performing XVR-imaging with a larger field of view comes with some complications. A laboratory setup with larger field of view requires a large opening angle of the X-ray beam. The further a voxel of the object is away from the optical axis of the setup, the more oblique travels the X-ray beam through the sample. If the rotation axis of the object is not similar to the optical axis of the setup, this can lead to artefacts as the projection of the object varies for different rotation angles. This can also be an issue for setups with a small field of view. However, this problem is more pronounced for setups with larger opening angles or a larger distance between optical axis and rotation axis. Furthermore, the large field of view of the *linescanner* is generated by the eight grating tiles, stitched together. It was not possible to assemble the tiles without any stitching gap between them. Therefore, because of these gaps, strips with a width of one or two pixel exist where the visibility equals zero and thus also the dark-field signal in those stripes are zero. When rotating the sample, the area with no visibility is moved across different locations of the sample. This leads to small artefacts in the images after retrieval of the XVR modalities. Here, XVR-imaging of large samples on a setup with a large field of view are presented as a proof of principle and the aforementioned problems will be addressed.

9.1 Materials and methods

To demonstrate XVR-imaging with a large field of view, a rotation stage (PRS-200 Precision Rotation Stage, PI, Karlsruhe, Germany) was integrated in the setup with configuration 3. The inner diameter of the rotation stage was 12 cm. Movements of the rotation stage were controlled with commands in *spec*. As wood generates a good XVR-signal it was chosen as a material for proof of principle measurements [Malecki, 2013; Malecki, 2014]. A 12 cm × 3.5 cm × 1.7 cm piece of spruce wood was imaged with a tube voltage of 60 kV and a current of 150 mA. The sample was placed 29.5 cm above the sample table. Images were taken for a whole rotation of the sample around the optical axis (z-axis) in 30° steps. For each rotation angle images were acquired with the *table-scan* method (cf. Chap. 8). After image registration and retrieval of the image modalities (attenuation and dark-field), the mean attenuation image \bar{A} was calculating by taking the mean of all attenuation images. Furthermore, the mean dark-field image \bar{D} , the degree of anisotropy D_A and the orientation of scattering structures θ were determined according to Eq. (3.15).

In addition, the femur of a calf was examined, representing a more relevant clinical sample. The sample was placed 30 cm above the sample table, the tube voltage was 60 kV. As the femur is denser than the wood a higher tube current (400 mA) than for the wood sample was used for imaging. Here, the bone was imaged for a whole ration around the optical axis, in 10° steps, as the dark-field signal of bone is weaker than of wood a higher sampling rate was chosen to increase statistics. Again, the mean attenuation \bar{A} , the mean dark-field image \bar{D} , the degree of anisotropy D_A and the orientation of scattering structures θ were calculated as before. Furthermore, a beam hardening correction as described in Sec. 5.2.3 was performed. However, POM was not used as a reference material but aluminium, as it has similar spectral attenuation properties as bone.

The images for both samples were taken using the *table-scan* acquisition method. As both samples did not have a great height, artefacts due to different beam path through the sample are not expected.

9.2 XVR images of a wood sample

In Fig. 9.1 the XVR-images of the strip of wood are shown. In the attenuation image (cf. Fig. 9.1 a)), thin bright vertically running lines appear, corresponding to the growth rings of the wood. Between the growth rings a slight decrease of the attenuation signal is visible. Furthermore, two bright spots, one on the top middle and one on the lower left side of the sample, are visible. The position of the spots corresponds with two knots in the wood. The knots also produce a strong dark-field signal (cf. Fig. 9.1 b)). However, the growth rings are not as clearly visible as in the attenuation image. Between the knots runs a vertical line with a strong dark-field signal. Looking at the sample, the core of the wood is partly visible. The highest degree of anisotropy is present in the part of the wood where the dark-field signal is

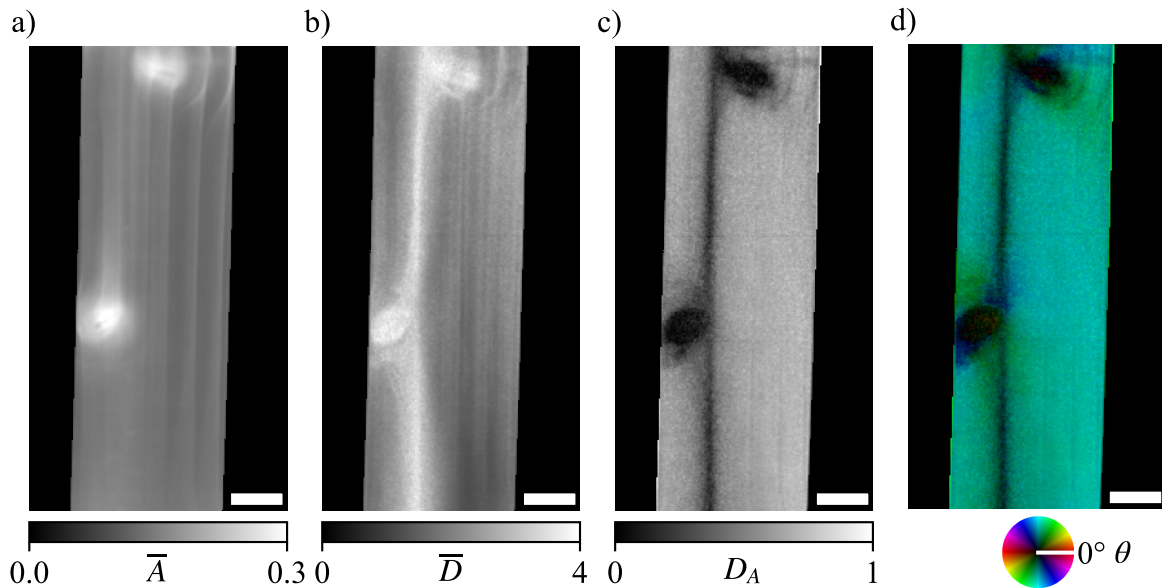


Figure 9.1: Mean attenuation (a), mean dark-field (b), degree of anisotropy (c), and orientation of scattering structure (d) images of a wooden bar. The scale bar in the lower right corner has the size 15 mm \times 4 mm. In the attenuation image the growth rings and knots are clearly visible. The growth ring and the core are also clearly visible in the mean dark-field, but not in the degree of anisotropy and orientation of scattering structure images. The colour of most of the wood in the orientation of scattering structure image indicates a scattering structure running parallel to the core.

low (cf. Fig. 9.1 c)). The two knots and the core scatter the X-rays isotropic in all directions. Therefore, the knots and the core are depicted as almost black in the colour coded image of the orientation of the scattering structures. Most of the rest of the wood is depicted in cyan colour indicating a vertical course of the scattering structures (cf. Fig. 9.1 d)).

The microscopic structure of wood consists of fibres running from the roots to the tree parallel to the core. The dark-field signal is mainly generated due to these fibres. As most of the wood is coded in cyan colour, the fibres are running parallel to the long axis of the sample. This implies that the long axis of the wood is parallel to the core of the tree from which the wood was cut out. Due to the different growth periods of the tree per year the wood is not homogeneous in radial direction, but growth rings are formed. Even within the growing periods the state of the wood changes. Early wood, growing in spring, is softer and more porous than late wood, growing in late summer and autumn [Desch, 1996]. The clearly visible growth rings in the attenuation image corresponds to the denser late wood rather than early wood. Also, due to the change of porosity the growth rings are visible in the dark-field image. However, the direction of the fibres does not change during the growth and therefore the growth rings are not visible in the degree of anisotropy and the direction of scattering structures images. Another distinct feature in the wood sample is the knots, visible in all four image modalities. As the newer layers of wood are added to the outside of the tree

trunk, branches connected to the trunk are gradually incorporated in the tree trunk during the growth. These branches within the tree are called knots. The knots appear as bright spot in the attenuation image, indicating on the material being here denser than in the rest of the wood. Furthermore, the knots also generate a stronger dark-field signal than the surrounding wood. The isotropic scatter direction of the knots might be due to the orientation of the fibres in the knots being perpendicular to the fibres of the wood (i.e., perpendicular to the image plane). While new layers of wood are added to the tree trunk they grow around the existing branch/knot and therefore change the direction of the fibres. This is visible in the image of the orientation of scattering structures. Here the colour around the knots changes to a more bluish and greenish colour compared to the cyan colour of the rest of the wood. The core of the wood is not visible in the attenuation images. However, it is clearly visible in the dark-field image. Furthermore, the core scatters isotropic like the knots. In contrast to the knots, there are not likely any fibres running perpendicular to the image plane. Therefore, it can be conducted that within the core a more crystalline and less fibre-like structure is present.

9.3 XVR images of a calf femur

In Fig. 9.2 a) a photograph of the calf femur on top of the rotation stage is shown. As the bone was larger than the inner diameter of the rotation stage, only the diaphysis of the bone was imaged. The attenuation image (cf. Fig. 9.2 b)) exhibits a strong signal at the rim of the bone and a lower signal in the middle of the bone. Similar to the attenuation image, the highest dark-field signal was found at the rim of the bone (cf. Fig. 9.2 c)). Barely any signal is present in the middle of the bone. The degree of anisotropy is also strongest at rim of the bone with mean values of the two ROIs being $\mathfrak{M}(\text{ROI}_{\text{orange}}) = 0.41 \pm 0.08$ for the orange coloured ROI and $\mathfrak{M}(\text{ROI}_{\text{green}}) = 0.29 \pm 0.03$ for the green coloured ROI (cf. Fig. 9.2 d)). The scattering direction follows the length of the bone. However, the degree of anisotropy is in the centre of the bone patchier than at the rim of the bone. Furthermore, streak artefacts are visible as dark radial lines in both images (cf. Fig. 9.2 d) and e)).

The femur belongs to the group of long bones. In the middle of the diaphysis, the shaft of the bone, is the medullary cavity with the yellow bone marrow. The cavity is surrounded by the compact or cortical bone. The cortical bone consists of cylindrical osteons, lying parallel to the long axis of the bone, with a diameter of 100 μm to 400 μm . In the middle of each osteon is a Haversian canal with blood vessels. Even though the main orientation of the osteons is along the long axis of the bone, cross connections to the Haversian canal exist, so called Volkmanns canals [Standring, 2015; Aumüller, 2020]. At the rim of the projected bone, the X-rays pass through more cortical bone than in the middle, where it also passes through the yellow bone marrow. However, the cortical bone is denser than the yellow bone marrow. As a result, the attenuation signal is higher at the rim of the bone. A similar result is seen in the dark-field image. Only here the signal originates from the fibre-like osteons, which are present in the cortical bone but not in the medullary cavity. Therefore, a higher dark-field signal is visible at the rim of the projected bone than in the middle. As

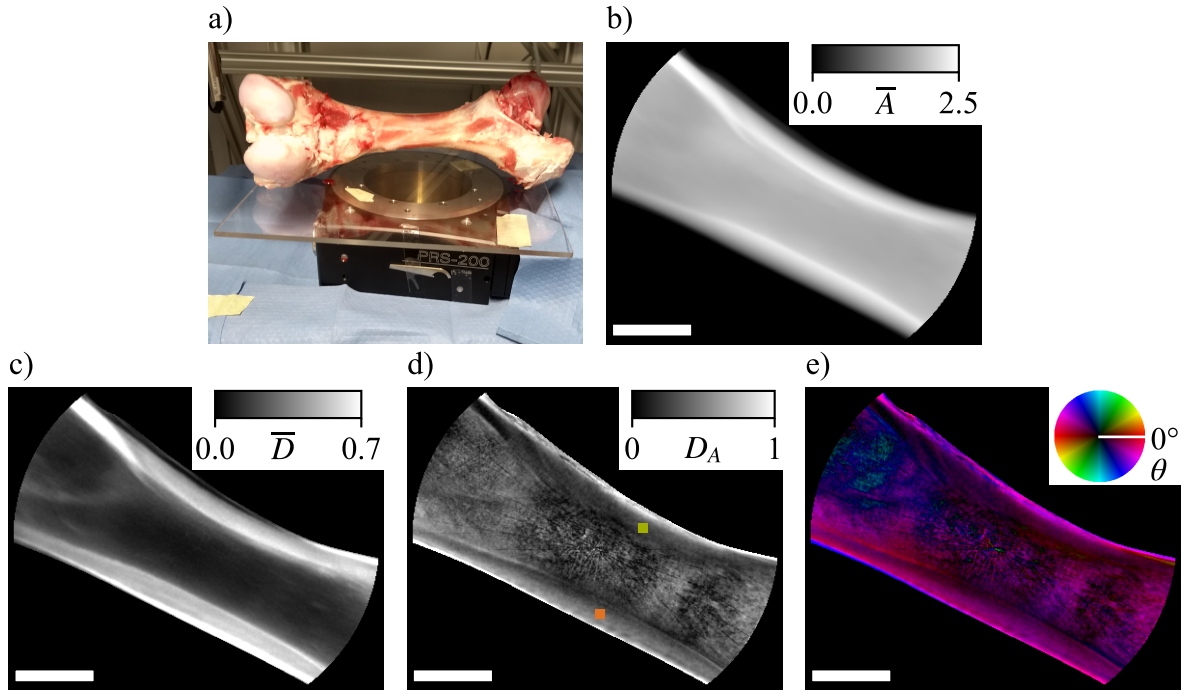


Figure 9.2: Photograph (a), mean attenuation (b), mean dark-field (c), degree of anisotropy (d), and orientation of scattering structure images (e) of a calf femur. The scale bar in the lower right corner has the size 30 mm \times 5 mm. The rim of the bone generates a strong attenuation and dark-field signal. The degree of anisotropy in this region is $\mathfrak{M}(\text{ROI}_{\text{orange}}) = 0.41 \pm 0.08$ and $\mathfrak{M}(\text{ROI}_{\text{green}}) = 0.29 \pm 0.03$. The orientation of scattering structures is along the long axis of the bone.

the dark-field signal is not only dependent on the imaged object but also on the sensitivity of the setup, comparing the dark-field signal of two different setups is not trivial. However, since the degree of anisotropy is the ratio of the mean dark-field signal and the amplitude of the change of dark-field signal, the sensitivity of the setup is not expected to influence the degree of anisotropy and it can be easily compared between samples measured at different setups. The degree of anisotropy found in the diaphysis of a human hand were between 0.25 and 0.41 [Jud, 2017; Jud, 2018]. These values are consistent with the degree of anisotropy values found in the here presented bone. The patchiness of the degree of anisotropy in the middle of the bone may result from the weak dark-field signal. Smaller changes of the signal, due to noise, have here a greater impact on the degree of anisotropy than for areas with a greater mean dark-field signal. Furthermore, the orientation of scattering structures, here the osteons, is along the long axis of the bone. This coincides with the description of bones in literature and previous XVR-measurements of bones, where the same orientation was found [Jud, 2017; Jud, 2018]. The radial streak artefacts likely originate from the gaps between grating tiles with no visibility signal. As at these points the dark-field signal is almost zero, the sinusoidal dark-field variation is for one rotation angle almost zero. Therefore, the fit is incorrect leading to a lower degree of anisotropy signal.

9.4 Conclusion

The here presented images show that XVR-imaging is possible for a three-grating setup with a polychromatic source and larger objects. The field of view in the images was limited by the opening of the rotation stage. The results regarding the orientation of scattering structure and degree of anisotropy are in concordance with literature and previous studies. Due to the gaps between grating tiles, streak-like artefacts are visible in the degree of anisotropy and orientation of scattering structures images. To reduce these artefacts the lines due to the gap have to be removed from the dark-field images. A simple approach would be finding the position of these lines in the dark-field image, e.g., by high-pass filtering the dark-field image or thresholding the transmission image. Then, an interpolation between neighbouring pixels of the line can be applied. Further, more elaborate information for the removal of these lines can be found in the dissertation of F. De Marco [De Marco, 2021].

The rotation stage was loosely placed on the sample table of the *linescanner*. No great care was taken to place the rotation stage in such a way that the rotation axis of the sample is identical to the optical axis of the setup. Even though the position of the rotation stage was not optimal, no artefact due the off-axis rotation of the sample was visible in the XVR-images. However, the samples were relatively flat. Therefore, the effect of an image acquisition with off-axis rotation for higher sample needs to be examined in further experiments.

In the here presented study, the feasibility of XVR-imaging with a large-field-of-view setup is demonstrated, achieving the next step for a translation of XVR-imaging to the clinics. However, the promising results from previous studies at small field of view setups have to be reproduced at a setup with a large field of view in future studies.

10 Retrieval of 3D information in X-ray dark-field imaging with a large-field-of-view setup

Three-dimensional X-ray images can be produced with CT or tomosynthesis. Whereas CT has the benefit of delivering accurate reconstructed image slices without overlay artefacts, tomosynthesis provides 3D information at lower dose and lower cost than CT. The basic principles of tomosynthesis and classical tomography are almost identical: during image acquisition, the source moves on a linear or circular pathway around the stationary sample. In tomosynthesis, multiple focal planes can be reconstructed from one acquisition, leading to a reduced dose compared to classical tomography [Niklason, 1997]. Those methods are also used in X-ray dark-field imaging, where a large number of studies on small samples were conducted [Schleede, 2013; Li, 2014; Garrett, 2015; Eggl, 2016]. Many of these works used filtered back projection as a reconstruction method. With the *linescanner*, it is possible to record X-ray dark-field radiography images of objects with a size in the vicinity of $30\text{ cm} \times 30\text{ cm}$, successfully translating X-ray dark-field radiography from small samples (the size of a mouse) to larger samples (the size of a human thorax). However, translating X-ray dark-field CT to larger samples is not straightforward. In the following, a method similar to tomosynthesis is used at the *linescanner* utilising the *table-scan* acquisition method (cf. Sec. 8) to obtain three-dimensional information of the sample. Therefore, an effect is utilised which is a disadvantage in the *table-scan* acquisition method (cf. Chap. 8): different features in the sample seemingly move with different velocity on the detector due to the cone geometry of the X-ray beam.

The findings in this chapter will be published in *Retrieval of 3D information in X-ray dark-field imaging with a large field of view* [Andrejewski, 2021b]. Figures and text passages in this chapter may appear identical to the publication. My primary contribution to this study was performing the measurements and the dose estimation as well as the adaptation of the progressing algorithm.

10.1 Imaging acquisition and processing

The images for this study were taken at the *linescanner* in configuration 3 (see Sec. 5.1). The sample was placed on the sample table positioned 35 cm above G_2 .

The flat field data were acquired by a simple stepping procedure. The sample data were acquired by a scan-step procedure. Therefore, image data of the sample were recorded as in the *table-scan* method (cf. Sec. 8.1). A schematic of the different relative sample positions is

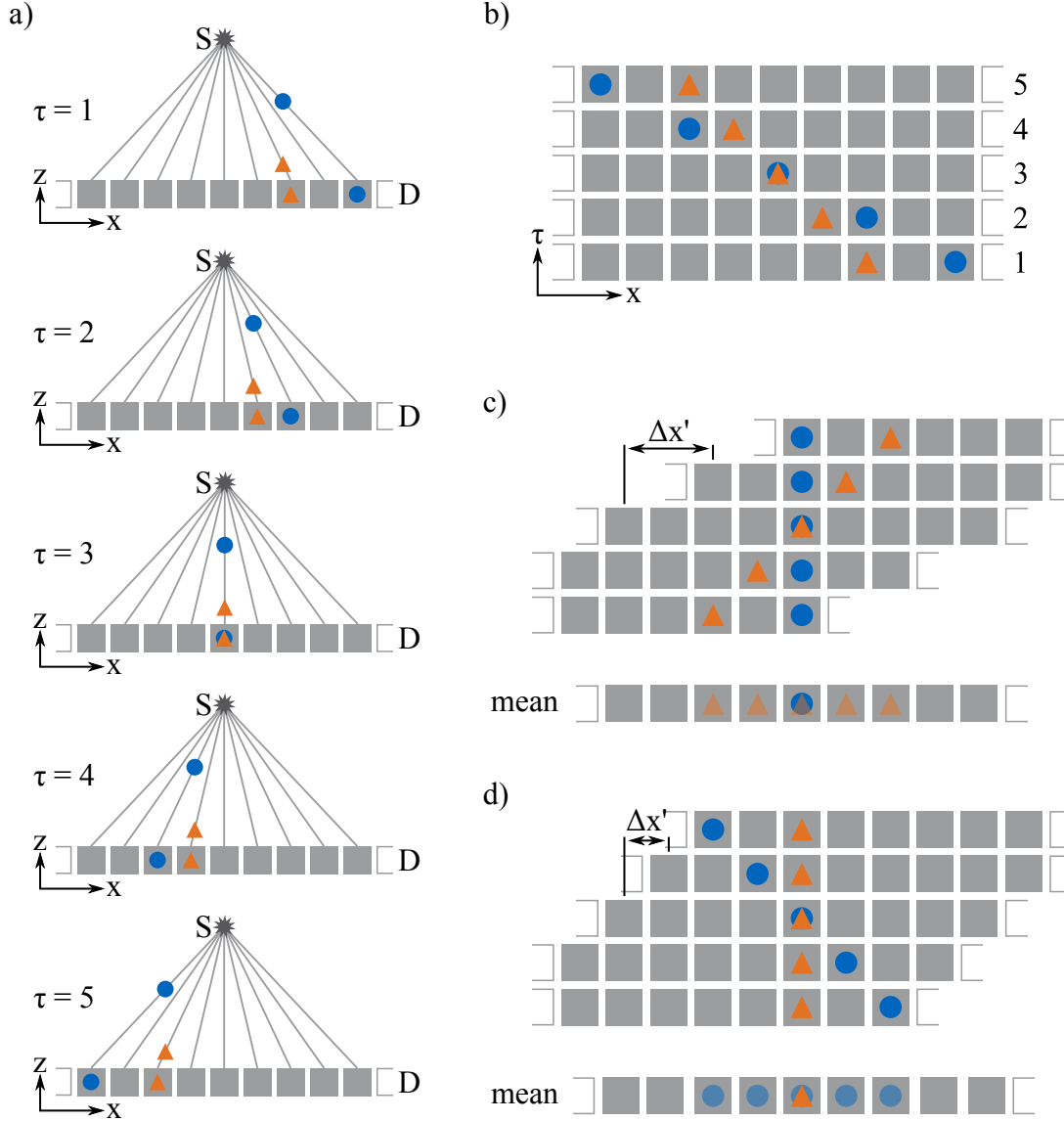


Figure 10.1: Schematic of the data resorting depicted for one modality (i.e. attenuation or dark-field). In a) the path of an X-ray from the source S through a sample (blue circle above an orange triangle) is depicted for different position indices τ of the sample. On the detector D , the blue circle travels faster than the orange triangle. The resulting image stack is depicted in b). The resorted data, where the blue circle is in the focal plane, are shown in c). To achieve this arrangement, each image had to be shifted by $\Delta x' = \Delta x(\tau, h)/\tau$ with respect to the previous image. Here, $\Delta x(\tau, h)$ denotes the absolute shift of the image in pixels. Taking the mean of this resorted data results in a sharp image of the blue circle and a blurred image of the orange triangle. This can be repeated for the orange triangle in the focal plane as shown in d).

given in Fig. 10.1 a), for a sample moving from right to left. Due to the cone beam, features at different heights, depicted by a blue circle and an orange triangle, are projected onto different detector pixels, depending on their relative sample position within the exposed slot. Once the sample has been moved completely across the slot, the G_0 grating was moved by one stepping distance (i.e. p_0/H , where H is the number of total steps), after which another scan was recorded. This was repeated H times until the G_0 grating was moved over an entire period. Thus, a complete stepping curve was recorded for each pixel at every relative sample position with corresponding position index τ . With the data from the flat-field and sample scan the attenuation A_τ and dark-field D_τ signal were obtained with Eq. (3.13) and (3.14) for each position index τ . This leads to a stack of 2D images with axes x , y , and τ for each modality, which is shown schematically in Fig. 10.1 b): the upper feature, the blue circle, seems to travel faster in the recorded images than the lower feature, the orange triangle. To retrieve information about the features' position in z -direction, the shift-and-add reconstruction method is used [Niklason, 1997]. Therefore, the stack has to be rearranged. First, a specific plane in z -direction has to be chosen as focal plane. For this focal plane a shift Δx in pixels for each τ is calculated using

$$\Delta x(\tau, h) = \frac{l_s \frac{\tau}{\tau_{\max}}}{s_p \cdot \frac{\overline{ST} - h}{\overline{SD}}}, \quad (10.1)$$

where l_s is the scan length (i.e. how far the sample was moved during one scan), s_p the pixel size of the detector, \overline{ST} the distance between source and the table, h the distance between table and the focal plane, and \overline{SD} the distance between the source and the detector. After each image in the stack has been shifted by Δx , only features in the focal plane are located at the same shifted x -position x' and y for all τ . Fig. 10.1 c) and d) show the shifted stacks for focal planes chosen for the two highlighted features, respectively. Averaging of the image stack in τ -direction results in a sharp image of the feature in the focal plane and blurred images of features outside the focal plane. Thus, from one set of recorded data, images corresponding to different focal planes can be reconstructed. As the sample is moved only in the x -direction, blurring of features outside the image plane occurs only in this direction. Features parallel to the x -axis remain unblurred in y -direction for all reconstructed height slices. Furthermore, the resolution in z -direction depends on how quickly blurring increases for features which are not in the focal plane with their distance to the focal plane. This, in turn, depends strongly on the effective opening angle of the X-ray beam.

10.2 Proof of principle measurements

For first proof of principle measurements, a neoprene cube with an edge length of 1 cm was placed between two open-celled foam slabs. Each foam slab has a height of 85 mm, thus the neoprene cube was 85 mm above the sample table. A scan range of 10 cm was chosen and total number of 75 exposures per scan were used. The tube voltage was set to 60 kV and the tube current to 150 mA. Images with a focal plane from $h = -100$ mm to $h = 200$ mm were reconstructed in 5 mm steps.

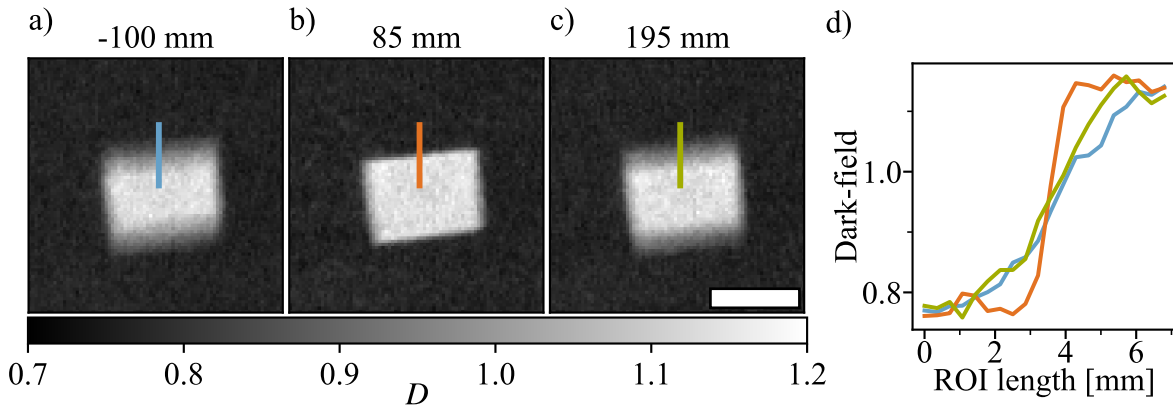


Figure 10.2: Dark-field images of a neoprene cube with an edge length of 1 cm reconstructed for focal planes 100 mm below (a), 85 mm above (b), and 195 mm above (c) the sample table. In d) the profile of the signal of the edge of the cube is shown for the three reconstructed focal planes. The colour of the line plots corresponds to the coloured ROIs in the dark-field images.

The dark-field images for reconstructed height slices of $h = -100$ mm, 85 mm and 195 mm are shown in Fig. 10.2 a) to c). As in the area of the neoprene cube, additional material-air interfaces are present, stronger X-ray scattering is present in this region. Therefore, the neoprene cube is visible in the dark-field images by its bright signal. In Fig. 10.2 a) and c) the upper and lower edge of the neoprene cube is blurred, whereas the right and left edge are relatively sharp. In the image with $h = 85$ mm all four edges of the cube are sharp (see. Fig. 10.2 b)). The profile of the dark-field signal in vertical direction for all three reconstructed heights are depicted in Fig. 10.2 d). Here, an ROI was chosen in all three images, with the upper edge of the cube inside the ROI (see blue, orange, and green lines in Fig. 10.2 a) to c)). The colour of the line plots corresponds to the colour of the lines in the dark-field images. The dark-field profile of the focal plane with $h = 85$ mm has the steepest increase of the three profiles. The profiles of the focal planes with $h = -100$ mm and $h = 195$ mm have similar slopes.

As the slope of the dark-field profile represents the sharpness of the cubes edge, it can be deduced that the sharpest image is that with a focal plane of $h = 85$ mm. The results of the visual and quantitative assessment of the dark-field signal for different focal planes are therefore in concordance: the focal plane with $h = 85$ mm delivers the sharpest image. This is also consistent with the layout of the sample as the neoprene cube was placed 85 mm above the sample table. However, the focal planes of the images presented here are 100 mm to 200 mm apart and the width of the blurring is only a couple of pixels, implying a low resolution in z-direction. This results from the narrow slot width and therefore narrow effective opening angle of the X-ray beam. Nevertheless, this first experiment shows that correct X-ray dark-field 3D information can be retrieved with the described method.

10.3 Improvement of the resolution in z-direction

The sample in the previous experiment was a simple geometrical shape. In the next step, a more complex sample was used. In view of medical imaging, a phantom was built, resembling the lung microstructure. Inside the phantom, materials to simulate liquid or soft tissue accumulation and air accumulation placed. Furthermore, the resolution in z-direction was improved.

10.3.1 Materials and methods

The phantom consisted of a plastic container filled with extruded polystyrene spheres (see Fig. 10.3 a)). Inside the phantom, sample vials (Eppendorf AG, Hamburg, Germany), with 0.6 ml and 1.5 ml fill volume, filled with water and air were placed to simulate liquid or soft tissue accumulation, and air accumulation, respectively (see Fig. 10.3 b)). The empty vials were attached at the lid of the container, approximately 85 mm above the sample table. The smaller one was placed in an upright position and the larger one was laid flat. At the bottom of the container (approx. 5 mm above the sample table) two water-filled sample vials were fixed. All vials were placed in such way that they do not overlap in the X-ray images.

Two measurements were performed. First, the image acquisition as described in Sec. 10.1 was carried out with the swing being perpendicular to the detector (i.e., in vertical position). In a subsequent measurement, data were acquired for seven slightly overlapping positions of the swing. This data were combined, simulating a setup with gratings covering the complete field of view of the detector. Thus, the effective opening angle of the X-ray beam was increased to 12° , which lead to an improved resolution in z-direction. For both measurements, the tube voltage was set to 60 kV and the tube current to 150 mA. The scan range was set to 45 cm and total number of 230 exposures per scan were used. Images with focal planes from $h = -100$ mm to $h = 200$ mm were reconstructed in steps of 5 mm.

For a quantitative determination of the height of the object planes, the course of the dark-field signal along the short axis of the sample vial was approximated for each reconstructed focal plane with a higher order Gaussian function, given by:

$$\mathbb{G}(x) = \mathfrak{A} \cdot \exp\left(-\left|\frac{(x - \bar{x})}{w}\right|^p\right) + o, \quad (10.2)$$

where \mathfrak{A} is the amplitude, $x - \bar{x}$ is the distance to the centre of the profile, w the width parameter, p the order, and o the baseline offset [Beirle, 2017]. To increase statistics, several dark-field profiles were averaged for each focal plane and each sample vial. Therefore, two ROIs were selected for each focal plane, one including the horizontal water-filled sample vial and the other the horizontal air-filled sample vial. Due to the blurring of the edges if the object is not in the focal plane, the width of the fitted higher order Gaussian function increases with rising distance between the focal plane and the object plane. However, the

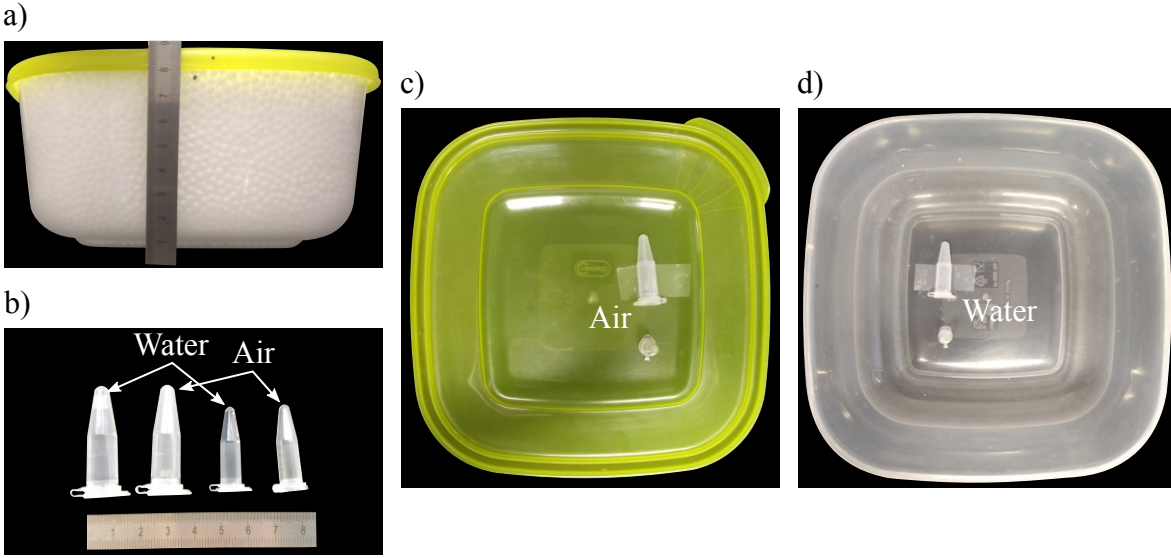


Figure 10.3: Photographs of the phantom. A plastic container is filled with polystyrene spheres to simulate the dark-field signal of the lung (a)). To simulate liquid or soft tissue accumulation and air accumulation, two sample vials were filled with water and two were left empty (b)). One of the vial pairs had a volume of 0.6 ml, the other 1.5 ml. The air-filled vials were attached to the lid of the plastic container (c)) and the water-filled vials were stuck to the bottom (d)).

width of a Gaussian function is ambiguous. For the standard Gaussian function (i.e., $p = 2$) often the full width half maximum (or minimum) or standard deviation Σ , which is related to w via $w_{p=2} = \sqrt{2}\Sigma$, is used. For the higher order Gaussian function the full width half maximum (or minimum) is dependent on p . Therefore, we will look at the full width $1/e^{\text{th}}$ minimum (FWEM), which is independent of p and equals to $2w$. Not only does the width of the fitted Gaussian function change for different focal planes but also the dark-field signal strength within the object. For noisy images and for an object scattering less than the background, this can be represented by the minimum of the fitted Gaussian function, calculated with $\min(D) = o - \mathfrak{U}$.

10.3.2 Results

Measurement with one interferometer frame position

Fig. 10.4 shows exemplary the dark-field and attenuation images of the phantom acquired with a single swing position for different reconstructed focal planes. All four sample vials are visible in both image modalities. The water-filled sample vials are located in the lower half of the images and those filled with air in the upper half. However, for the air-filled sample vials only the plastic walls of the vials are clearly visible in the attenuation images. The air-filled sample vials generate a lower dark-field signal than the water-filled sample vials.

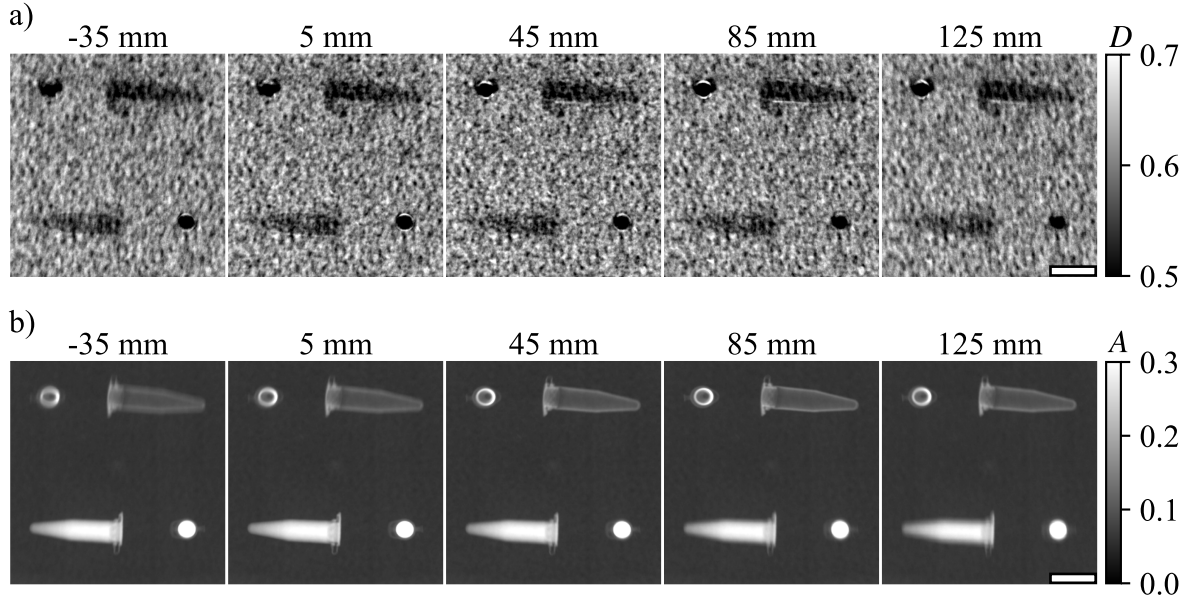


Figure 10.4: Dark-field (a) and attenuation (b) images of the sample vials in the plastic container for different focal planes. The distance of the focal planes to the sample table were -35 mm, 5 mm, 45 mm, 85 mm, 125 mm, where the negative sign corresponds to a plane below the sample table. The images were acquired with only one position of the swing. The background of the dark-field is quite patchy due to the polystyrene spheres. Although all four sample vials are clearly visible, a change in sharpness of the sample vials cannot be easily seen in the dark-field images. All four sample vials can also be seen in the attenuation images, where even a change of sharpness for different focal planes is visible.

In the attenuation images a changing sharpness of the sample vials is visible for different focal planes. The water-filled sample vials appear the sharpest in the focal planes -35 mm to 45 mm, whereas the air-filled vials are clearest in focal planes 45 mm to 85 mm. The dark-field images are patchy and making such visual assessments is more difficult.

Fig. 10.5 a) shows the dark-field profile along the short axis of the air-filled sample vial (left) for selected focal planes. The fitted higher order Gaussian are depicted on the right side of Fig. 10.5 a). The positions of the ROIs for the fits are indicated in Fig. 10.5 b). The orange rectangle corresponds to the ROI around the water-filled sample vial, and the blue one to the ROI around the air-filled sample vial. The dark-field profiles and higher order Gaussian fits for different focal planes are difficult to differentiate. However, the courses of the FWEM over all focal planes, as shown in Fig. 10.5 c) top, and $\min(D)$, as shown in Fig. 10.5 c) bottom, exhibit minima. The minima of the FWEM is at -20 mm for the water-filled sample vial and 55 mm for the air-filled sample vial. For $\min(D)$ the minima are located at -40 mm for the water-filled sample vial and 80 mm for the air-filled sample vial.

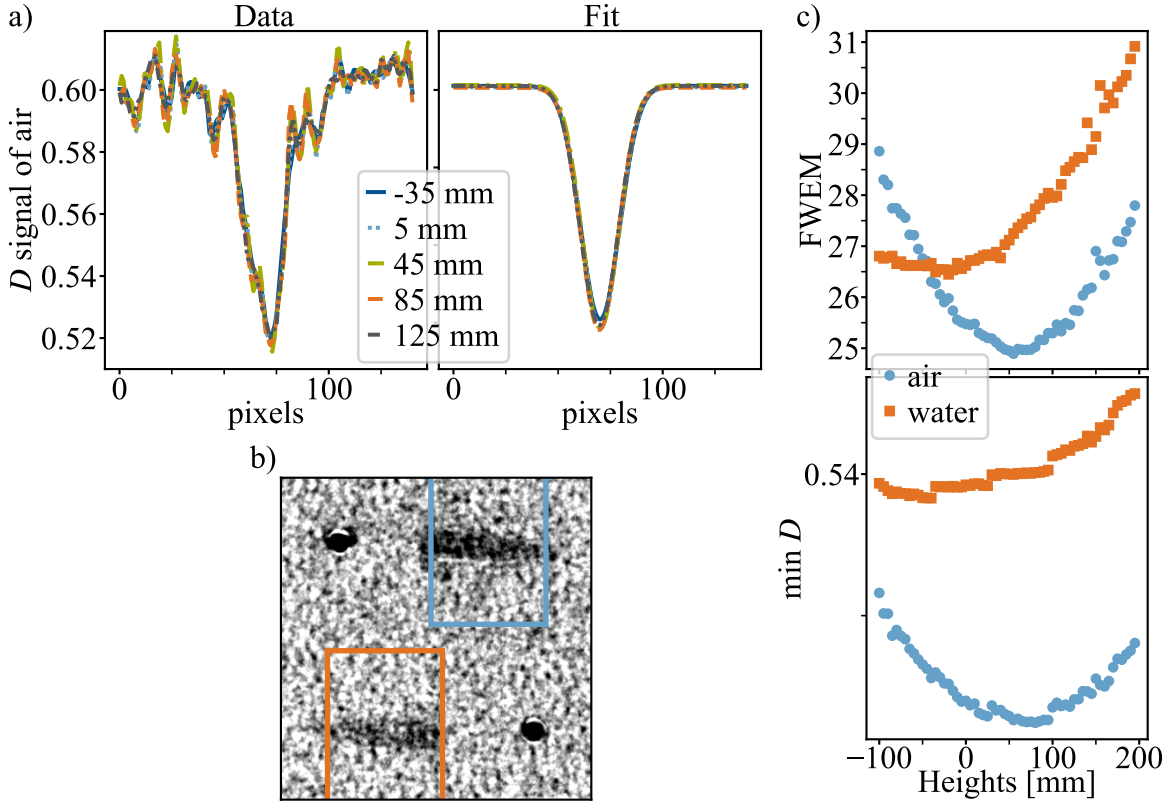


Figure 10.5: a) Dark-field line plot (left), acquired with one swing position, and the corresponding Gaussian fit (right) along the short axis of the air-filled sample vials for different focal planes. To increase statistics the mean of the dark-field signal inside a ROI was taken in horizontal direction. The ROIs are indicated in b), where the orange and blue rectangle correspond to the ROIs for the sample vial filled with water and air, respectively. c) The FWEM (top) and $\min(D)$ (bottom) of the Gaussian fit for all reconstructed focal planes are shown. The FWEM is minimal for focal planes at -20 mm for the water-filled sample vial and 55 mm for the air-filled sample vial. The minima of $\min(D)$ are at -40 mm and 80 mm for the water-filled and air-filled sample vial, respectively.

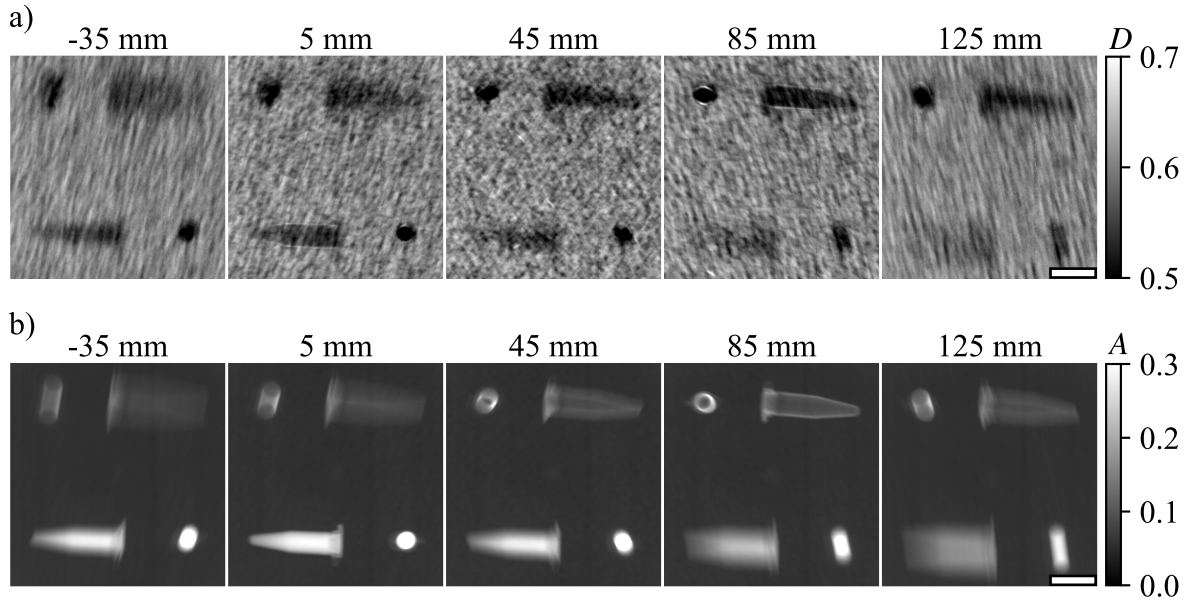


Figure 10.6: Dark-field a) and attenuation b) images of the sample vials in the plastic container for different focal planes. The distance of the focal planes to the sample table are -35 mm, 5 mm, 45 mm, 85 mm, 125 mm, where the negative sign corresponds to a plane below the sample table. The images were acquired for seven relative positions of the swing and detector to simulate a full field grating. A change of sharpness for different focal plans can be seen for all sample vials in both modalities. Furthermore, the patchy dark-field background becomes blurry for focal planes at -35 mm and 125 mm.

Measurement with seven interferometer frame positions

Fig. 10.6 shows the dark-field a) and attenuation b) images of the phantom for different focal planes acquired with seven swing positions covering the complete field of view of the detector. Again, all sample vials are visible in both modalities. Like before, the dark-field signal of the air-filled sample vial is lower than the dark-field signal of the water-filled sample vial. The patchiness of the background of the dark-field images seems to be blurred for focal planes at -35 mm and 125 mm. In both modalities the change of sharpness of all four sample vials are visible for different focal planes. The sharpest image of the sample vials filled with water and air is achieved in both modalities in the focal planes 5 mm and 85 mm above the sample table, respectively.

For the quantitative evaluation of the images, where the complete field of view of the detector was exposed, the same ROI positions as indicated in Fig. 10.5 b) were used. The line plots and higher order Gaussian fits along the short axis of the sample vials (cf. Fig. 10.7 a)) are much clearer to distinguish for different focal planes than for the case of one interferometer position (see Fig. 10.5 a)). The FWEM for different focal planes are shown in the top part of Fig. 10.7 b). It is minimal at 75 mm and 0 mm for the air-filled and water-filled sample

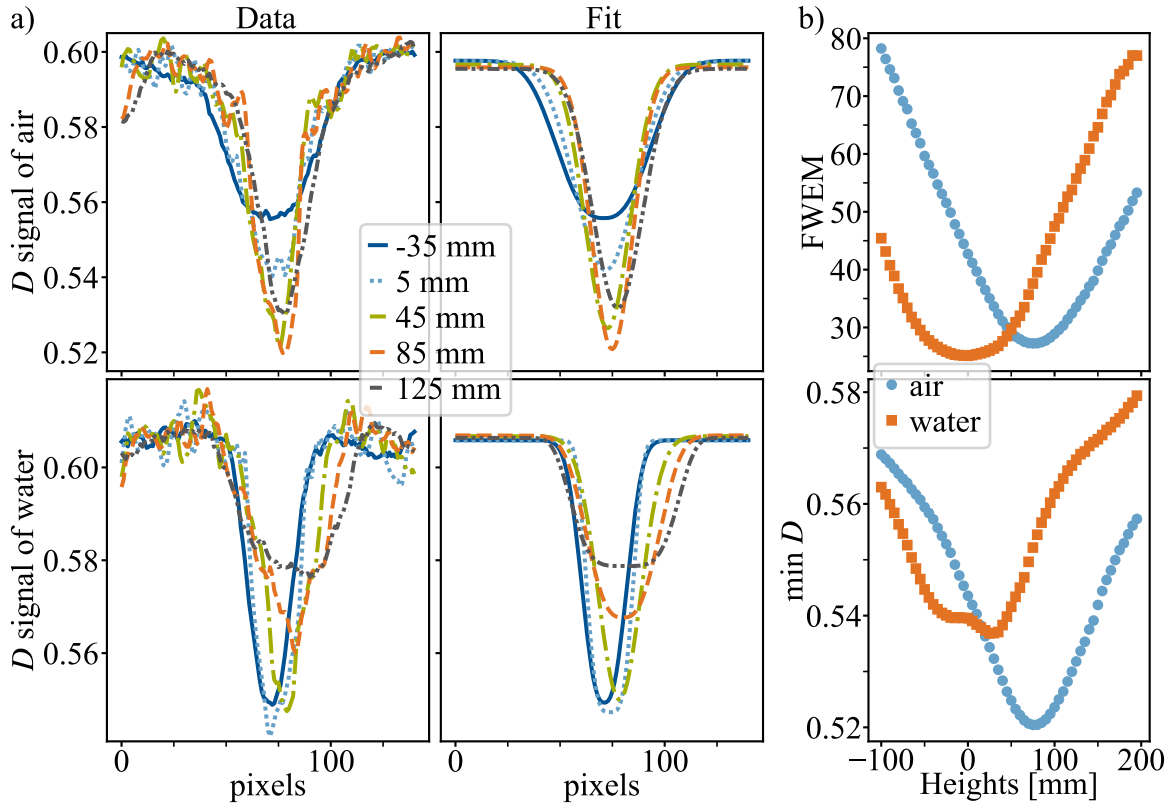


Figure 10.7: Dark-field line plots (left), acquired with seven swing position covering the complete detector's field of view, and corresponding higher order Gaussian fit (right) along the short axis of the sample vials for several focal planes a). The same ROIs as in Fig. 10.5 b) were chosen. The change of the FWEM over the height of the focal plane is shown in the top part of b). The FWEM are minimal for focal planes at 75 mm for the air-filled sample vial and 0 mm for the water-filled sample vial. At the bottom of b) $\min(D)$, determined with the higher order Gaussian fit, over the heights of the focal planes are shown. Here the minimal values are at 75 mm and 25 mm for the sample vial filled with air and water, respectively.

vial, respectively. At the bottom of Fig. 10.7 b) $\min(D)$ are plotted over the heights of the focal planes. Its value is minimal for focal planes at 75 mm and 25 mm for the air-filled and water-filled sample vial, respectively. Whereas the course of the minimum dark-field signal exhibits a distinct minimum for the air-filled sample vial, this is not the case for the water-filled sample vial.

10.3.3 Discussion

As seen in all dark-field images, the background is quite patchy. This is probably caused by the imaged polystyrene spheres. Different volumes of air between the spheres leads to an

unequal number of interfaces along which the X-rays are scattered. Furthermore, the spheres themselves might have different densities of air-material interfaces.

In the images acquired with one swing position, the sharpness of the sample vials changes only slightly for different focal planes. As the opening angle of the beam is very narrow for this method, the relative displacement of the projection of an object, while it passes through the beam, is small. Therefore, an object is only slightly blurred if it is not placed in the focal plane, leading to a low resolution along the beam (z-direction). This low z-resolution combined with the patchy background in the dark-field images hampers the visual determination of the correct object plane. Even a determination of the object plane looking at the line plots through the object and the Gaussian fits is difficult due to the poor z-resolution. However, the change of the FWEM and $\min(D)$ for different focal planes can be seen more clearly, when plotting it over the height of the focal plane over the table. The focal plane with the smallest FWEM or $\min(D)$ for the object indicates the object plane. Nevertheless, the determined heights of the object plane over the sample table, -20 mm (FWEM) and -40 mm ($\min(D)$) for the water-filled sample vial and 55 mm (FWEM) for the air-filled sample vial, do not match the heights known from the sample preparation, 5 mm and 85 mm, respectively. Only the determined height of the air-filled vial, 80 mm, is very close to the known height. However, change of the FWEM or $\min(D)$ from one focal plane to the next is very small, especially around the minimum value of the FWEM and $\min(D)$, respectively. This plus an slightly noise course of the FWEM or $\min(D)$ might lead to the offset between the experimentally determined object planes and the ground truth. Furthermore, the assumed relative distances between object and the sample table might be imprecise as an accurate measurement was difficult to perform.

By imitating full field gratings through combining multiple measurements, a larger effective opening angle of the X-ray beam was obtained. Thus, objects are blurred more strongly if they are not located in the focal plane and a better z-resolution is achieved. Therefore, it is easier in a visual assessment to determine the object plane, even in the patchy dark-field images. As the patchy dark-field background is also blurred if the focal plane is outside the plastic container, one can assume that the pattern is caused by the extruded polystyrene spheres.

Furthermore, the line plots and the Gaussian fits of the sample vials for different focal planes are more clearly distinguishable than for the acquisition with one swing position. Also, the variation of the FWEM or $\min(D)$ with focal plane height is higher than for the acquisition with one swing position. Therefore, the z-resolution is clearly increased. For the air-filled sample vial the same results were found when determining the object plane height FWEM and $\min(D)$ of the Gaussian fits. The determined object plane height differed by 25 mm for the water-filled sample vial using both methods. However, $\min(D)$ over each line plot did not exhibit a clear minimum as a function of focal plane height. The experimentally determined object plane heights concur good with the known ones, except for the object plane height for the water-filled sample vial determined by the minimum dark-field signal. The slight offset between the experimentally determined object plane heights and the known ones reinforces the assumption that the measured relative distances to the sample table are not accurate.

The sample used here is a rather simple lung phantom with no superposition of different features. However, if such a superposition is present, an evaluation of the object plane height might not be possible. We believe that the evaluation with the change of dark-field signal strength within the object is more robust toward this constraint. To achieve a good z-resolution, relatively large gratings are necessary. The method to imitate a full field grating presented here is rather time consuming. However, fabricating large gratings with sufficient quality is difficult and expensive.

To conclude, the resolution in z-direction can be improved by increasing the effective grating area. Thus, a visual assessment of the object planes becomes possible. Furthermore, the quantitative determination of the object plane becomes more accurate.

10.4 Measurements with a clinical lung phantom

As a next step, a clinical phantom was used as a sample. Again, sample vials with air and water were placed inside the phantom to mimic lung diseases. Furthermore, the dose of the reconstructed images was reduced.

10.4.1 Materials and methods

For more realistic measurements a human chest phantom, Multipurpose Chest Phantom N1 ‘Lungman’ (Kyoto Kagaku, Kyoto, Japan) (cf. Fig. 10.8 a) and b)) was used. Two 1.5 ml (diameter: 1 cm, length: 4 cm) vials (Eppendorf AG, Hamburg, Germany) filled with water and air, respectively (cf. Fig. 10.8 c)), were fixed at the inside of the phantom’s rib cage. The lung volume was filled with extruded polystyrene spheres to model the lung tissue with its many air-tissue interfaces. Please note that the bone substitutes generate a stronger dark-field signal than real bones [Frank, 2021]. The measurements were taken at 60 kV tube voltage and 600 mA tube current. The scan range was 47 cm and a total number of 239 exposures per scan were used. To achieve a better z-resolution, the image acquisition was performed for seven different positions of the swing, covering the complete field of view of the detector.

The dose area product was estimated from the incident air KERMA, measured with a PTW NOMEX dosimeter (PTW, Freiburg, Germany) and the area of the lung. With this, the ED can be approximately calculated using the conversion factor given in [Wall, 2011]. To evaluate image quality with reduced dose, image reconstruction was repeated with subsets of the recorded data. First, the number of phase steps used for the calculation of the dark-field and attenuation images was reduced from seven to five. Then, the number of exposures per scan was reduced from 239 to 14 evenly distributed exposures. Lastly, the number of positions of the swing was decreased from seven to four, omitting every other swing position.

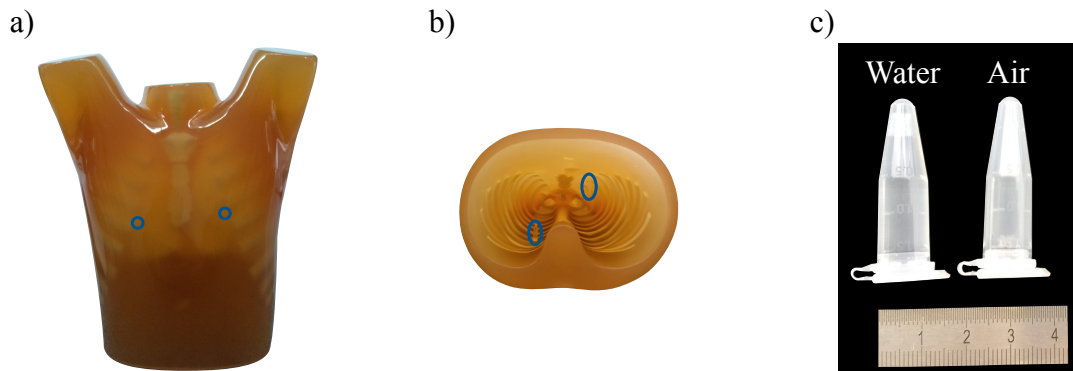


Figure 10.8: Photograph of the imaged phantom. The frontal view (a) and inner view (b) are shown. The position of the sample vials filled with water and air are indicated by the blue circles. For data acquisition, the lung region was additionally filled with extruded polystyrene spheres. (c) A photograph of the sample vials filled with water and air.

10.4.2 Results

Fig. 10.9 shows the dark-field (a)) and the attenuation (b)) images of the phantom for different reconstructed heights of the focal plane. The dark-field signal of the lung is overlaid by a strong signal of the rib cage for all focal planes due to strong scattering in the bone phantom material. With changing focal planes, the sharpness of ribs changes: at $h = 0$ mm the dorsal section of the rib cage and at $h = 165$ mm the ventral section of the rib cage appear sharpest. In the image with $h = 35$ mm, the water-filled vial becomes apparent as a clearly delineated shadow (orange square in Fig. 10.9 a). For other focal planes, this shadow is blurred or hardly visible. The air-filled vial is also visible and appears sharpest at $h = 165$ mm (blue square in Fig. 10.9 a)). As the ‘Lungman’ was constructed as a thorax phantom for conventional thorax radiography and CT, the attenuation images resemble those of a real human thorax well. While the air-filled vial is better visible in the dark-field images, the contrast for the water-filled vial is stronger in the attenuation images (Fig. 10.9 b)). The air-filled vial is barely visible in any of the attenuation images. However, the outline of the vial is visible. Both vials appear sharpest in the same focal planes as in the dark-field images.

For the images shown in Fig. 10.9 all, recorded image data were used for reconstruction, leading to an effective dose 2.8 mSv. Fig. 10.10 shows the dark-field images at reduced effective doses. For better comparison the dark-field images with an effective dose of 2.8 mSv are shown in the first row. In the second row, the number of phase steps was reduced from seven to five, leading to an effective dose of 2.0 mSv. Compared to the images with an effective dose of 2.8 mSv, only the noise level in the spine changes. The blurring of features outside the focal plane remains identical. Reducing the number of exposures during one scan from 239 to 14 (third row in Fig. 10.10) also only has a small impact on the image quality. However, this way the dose can be reduced significantly to 119 μ Sv. For the images in the bottom row, the number of swing positions was reduced from seven to four, leading to an

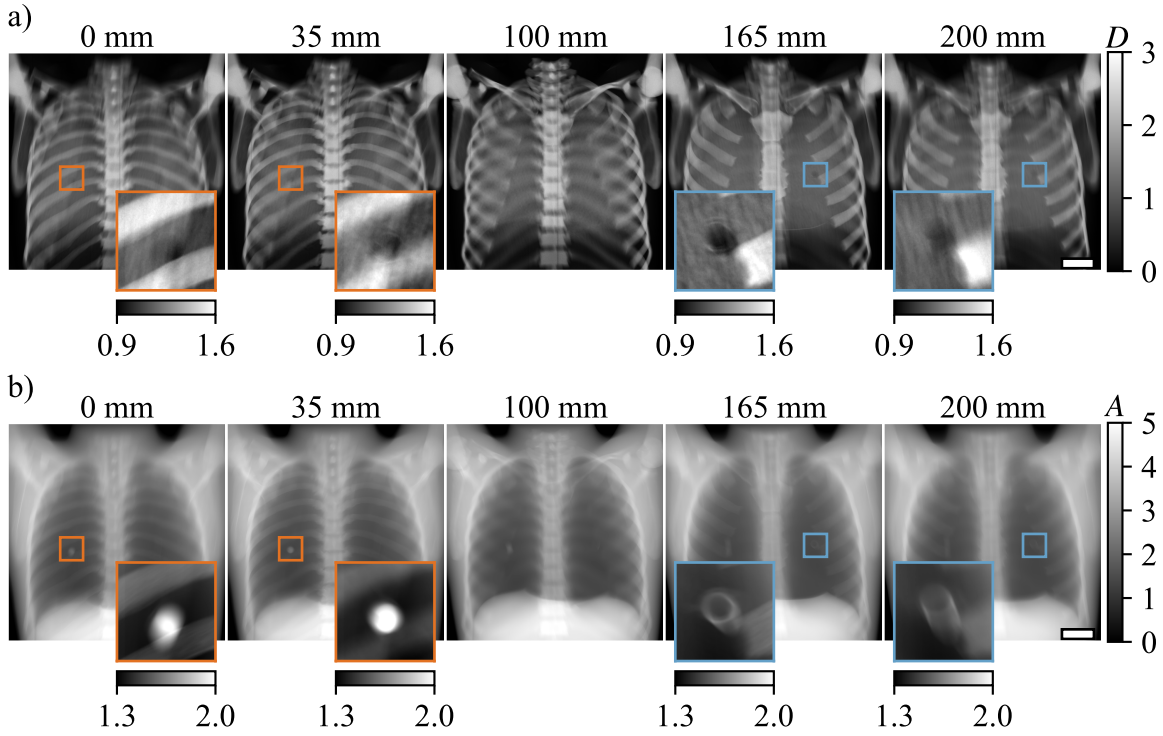


Figure 10.9: Dark-field a) and attenuation b) images of the phantom reconstructed for different focal planes with $h = 0$ mm, 35 mm, 100 mm, 165 mm, and 200 mm. To simulate a grating covering the full field of view, the images were acquired for seven swing positions. Furthermore, all seven phase steps and all 239 exposures per scan were used for reconstruction. The sharpness of the bones and the vials changes for different distances between the focal plane and the sample table in both image modalities. A magnification of the area where the water-filled vial was placed is shown for $h = 0$ mm and $h = 35$ mm (orange square). Here, the vial appears sharpest in the images at $h = 35$ mm, whereas the dorsal section of the rib cage appear sharpest in the images at $h = 0$ mm. The area where the air-filled vial was placed is magnified for $h = 165$ mm and $h = 200$ mm (blue square). The air-filled vial as well as the ventral section of the rib cage appear sharpest in the images at $h = 165$ mm. The scale bars have a length of 5 cm.

effective dose of $68\text{ }\mu\text{Sv}$. Ribs located outside the focal plane appear more prominent than in the previous images. However, the detectability of both inserts was not affected by the reduction in effective dose.

10.4.3 Discussion

We demonstrated the retrieval of X-ray dark-field images with 3D information using a human chest phantom. By visual assessment of the dark-field images, the relative position of various features within the thorax could be determined. As both vials, filled with water and air, respectively, do not scatter X-rays, they appear as darker regions in the lung image. If the vials are not in the focal plane of the image, these spots are blurred and the difference in the dark-field signal between vial and background of the lung decreases. The contrast of the air-filled vial is higher than for the one filled with water in the dark-field images. This is likely caused by a superposition of the water-filled vial and a rib of the phantom. As real bones generate a much weaker dark-field signal, the detectability of a foreign body in the lung is expected to be less affected by their signal superposition.

While the high effective dose of 2.8 mSv in the images shown in Fig. 10.9 might not be a problem for non-destructive testing, it is too high for clinical imaging. Reducing the number of exposures of the sample during the image acquisition also reduces the total effective dose. However, a good image quality needs to be maintained, to prevent a reduction of the diagnostic value of this method. The dose can be lowered by reducing the number of the phase steps. Still, enough steps are needed in order to calculate the different attenuation and dark-field images. Reducing the number of exposures during one scan or the number of swing positions, reduces the number of angles under which a voxel is sampled. If the number of angles is too small or not evenly distributed, artefacts can arise in the final images. The artefacts appear as multiple images of the features, as can be seen for the clavicles in the image taken at $h = 0\text{ mm}$ with $68\text{ }\mu\text{Sv}$. The clavicles are far from the image plane and appear several times. From this observation, it is clear that the angular sampling is insufficient to blur them evenly. Nevertheless, both vials are still visible in these images. At the same time the effective dose applied is only two times higher than for clinical X-ray dark-field radiography [Willer, 2021].

The results presented here are a first proof of principle. To determine the diagnostic value of this method in a clinical application, an extensive study would have to be performed. Moreover, the best trade-off between image quality and dose has to be determined. The larger the angle range, i.e. total beam divergence, the better is the z-resolution. The beam divergence of the current setup is insufficient to achieve a reasonable z-resolution with a set of data from one single swing position. This problem was here circumvented by recording seven data sets with different swing positions. Consequently, the measurement procedure is time consuming. This might not be a problem in material testing, but it is not practical for clinical imaging. Additionally, the fabrication of large gratings covering the complete area of the detector has not yet been achieved. Constructing a setup with multiple slot interferometers with

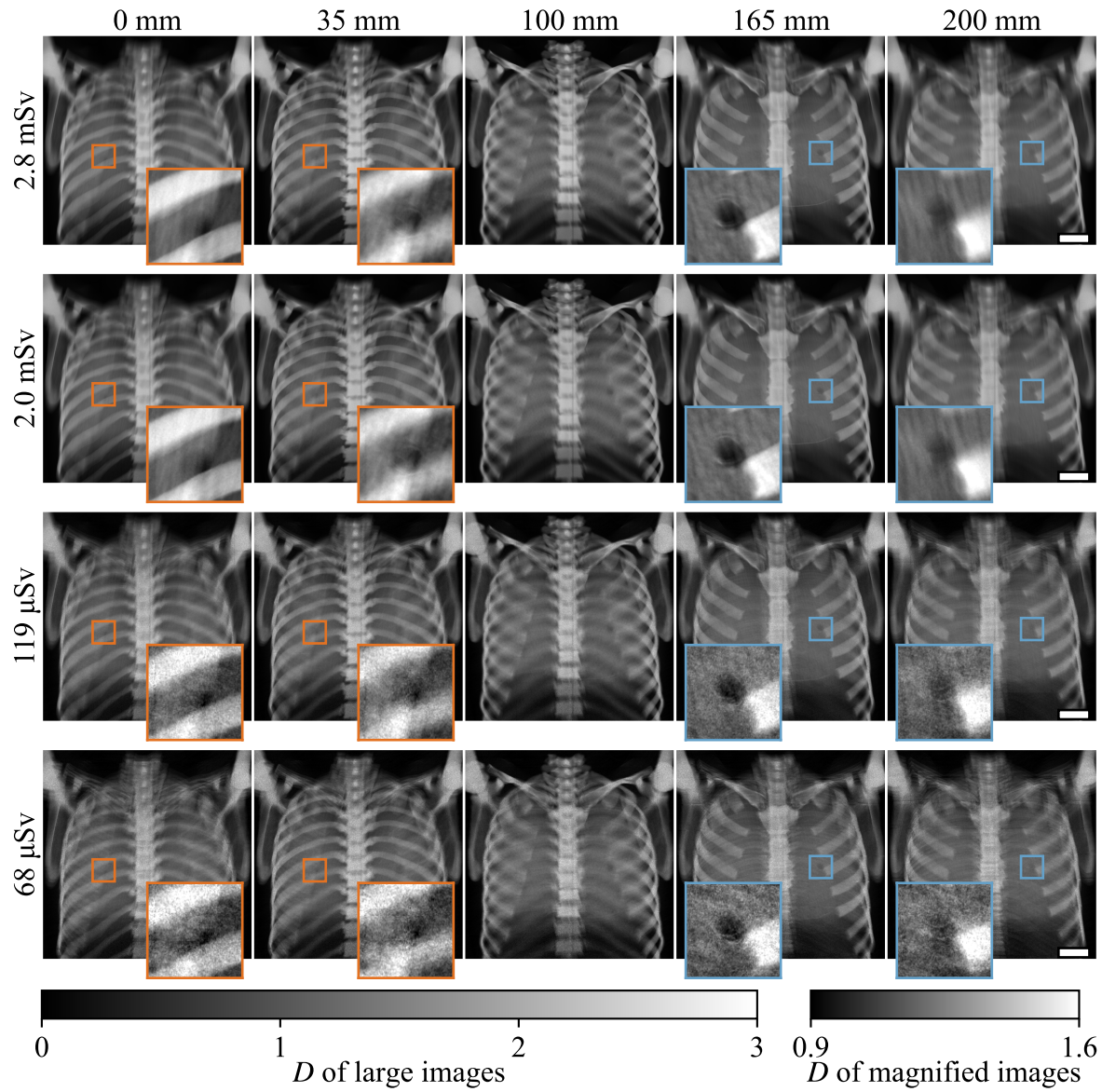


Figure 10.10: Dark-field images of the phantom for different effective doses (rows) and different focal planes (columns). The dose was reduced by successively decreasing the number of images used for reconstruction. In the first row, the dark-field images with an effective dose of 2.8 mSv are shown for better comparison. In the second row, the number of phase steps was reduced from seven to five, compared to Fig. 10.9. In the third row, additionally to the reduction of phase steps from seven to five, the number of exposures per scan was reduced from 239 to 14. In the last row, the number of swing positions was decreased from seven to four, omitting every second swing position. Here, the reduced number of phase steps (five) and exposures per scan (14) were also used for reconstruction. Only in this last step, artefacts appear and affect the image quality. The scale bars have a length of 5 cm

different projection angles could be a solution to this problem. With such a setup, acquisition of attenuation and dark-field images at a relatively low effective dose might be possible. The reconstruction method used here was a simple shift-and-add method. This leads to several appearances of features if the angular sampling is insufficient. However, there are other reconstruction methods like filtered back projection or iterative reconstruction, which might be able to reduce those artefacts. Furthermore, as seen with the water-filled vial, a superposition of the signal from the examined feature with the signal from other objects could hamper the detectability of the feature. Further studies should be conducted to evaluate the magnitude of this effect for different types of samples. Dark-field CT does not suffer from the superposition of structures. However, combining dark-field with a large-field-of-view CT scanner is technical challenging. Therefore, the method presented here offers a good trade-off: it supplies more information than X-ray dark-field radiography, but it is technical easier to implement than a large-field-of-view dark-field CT scanner.

In conclusion, we were able to gain 3D information of the position of features in the sample in X-ray dark-field imaging. However, the presented study is only a first proof of principle and the benefits from this method for non-destructive testing and clinical applications has to be demonstrated in further studies.

11 Conclusion and outlook

This thesis discusses studies and experiments at the *linescanner*, a large-field-of-view X-ray dark-field setup. The first two presented studies were an important addition to the already existing work on medical X-ray dark-field imaging: the optimal tube voltage for X-ray dark-field thorax radiography was determined (cf. Chap. 6). Therefore, two studies were conducted in which the subjective image quality and signal strength in the dark-field images and the objective dark-field contrast were determined in each study. While the first study evaluated thorax images acquired at the *linescanner* of a human cadaver, in the second study, images of a thorax phantom taken at a clinical prototype for X-ray dark-field thorax imaging were investigated. Both studies revealed that the optimal tube voltage for dark-field thorax radiography of 60 kV to 80 kV is lower than for attenuation thorax radiography at 120 kV to 130 kV. The signal strength and image quality of the attenuation images taken at these tube voltages are only slightly lower than that of the images taken the tube voltages used in clinical routine. The results obtained in these studies are important for further clinical chest studies, as X-ray dark-field chest imaging is a new clinical method and therefore, ideal acquisition parameters such as tube voltage were previously not determined.

The third study presented first results of dark-field signal strengths in different organs in the human body (cf. Chap. 7). Whereas the dark-field signal in the lung is predominantly generated by small angle scatter of the X-rays on the air tissue interfaces of the alveoli, the signal in the bone is caused by both small angle scatter and beam hardening effects. Despite the lung and bony structures, dark-field signal is also generated by calcifications within the superficial femoral arteries and foreign bodies. As the presented study gave an overview, in-depth studies have to be performed in the future, evaluating the clinical benefit of X-ray dark-field imaging of different organs.

The initially implemented acquisition procedure at the *linescanner* is based on the rotation of the interferometer around the focal spot of the source, while source, detector, and sample remain stationary (in this thesis called ‘*swing-scan*’). However, it is also possible to keep interferometer, source and detector stationary and move the sample through the exposed slot (in this thesis called ‘*table-scan*’). Chap. 8 describes the implementation of the *table-scan* method at the *linescanner* setup. The adaptation of the processing is described, and images taken with the *table-scan* method are shown. Comparing images acquired with both methods reveals almost identical attenuation images. Also, the dark-field images are very similar but exhibit different artefacts depending on the acquisition method. Moreover, the artefacts in the dark-field images are stronger than in the attenuation images. Furthermore, in the *table-scan* acquisition artefacts on sharp edges of thick samples occur, which can be reduced most likely with a narrower exposed slot. Further studies as well as setup and processing upgrades

have to be performed to determine the origin of the artefacts and reduce the artefacts. A possible application of this method is a conveyor belt like imaging setup which might be useful in non-destructive testing of a large number of samples. Therefore, the processing might have to be adapted to allow real time image processing.

Chap. 9 transfers XVR-imaging from setups with small field of view to a setup with a large field of view. XVR-images of a wooden sample and of a calf femur were presented. The XVR-images of a calf femur revealed a comparable degree of anisotropy signal as reported in other studies. However, artefacts due to the gaps between grating tiles are visible in the images describing the degree of anisotropy and orientation of scattering structure. Furthermore, the field of view was limited by the opening of the rotation stage. For imaging larger samples than the ones presented here, a rotation stage with a larger opening has to be utilised. This study demonstrated that XVR imaging is possible at large-field-of-view setups.

In the last study (cf. Chap. 10), a method similar to tomosynthesis to retrieve three-dimensional information in X-ray dark-field imaging of large samples is presented. By moving the sample through the divergent beam of the *linescanner*, projections of features with different distances from the source seemingly move with different velocity over the detector. Therefore, after resorting the acquired images, different focal planes can be obtained. First, proof of principle measurements of a neoprene cube were presented. Then, the resolution in z-direction was improved by obtaining images at different interferometer positions, covering the complete field of view of the detector. Lastly, a chest phantom was imaged with the presented technique. It was possible to allocate different features within the sample to corresponding focal planes, demonstrating that the presented method is able to retrieve 3D information in X-ray dark-field imaging not only for a simple phantom but also for more complex samples. However, the acquisition of the images with improved z-resolution was very time consuming. A possibility for faster acquisition was proposed (i.e., a setup with multiple slot interferometers). Future studies on the feasibility of such a setup are needed.

In conclusion, this thesis presents various studies on pre-clinical X-ray dark-field imaging and the translation of dark-field radiography to a large field of view. The here presented results are important for future X-ray dark-field studies in the medical research and the improvement of the X-ray dark-field imaging method.

A Supplementary information of Sec. 6.1

Image quality score

kV	Individual readings				Grouped readings			
	Dark-field		Absorption		Dark-field		Absorption	
	R	L	R	L	R	L	R	L
60	4, 5 , 6	4, 4 , 6	4, 5 , 5	4, 5 , 5	4, 5 , 5	4, 4 , 5	4, 5 , 5	4, 5 , 5
70	3, 5 , 6	3, 5 , 6	4, 5 , 5	4, 5 , 5	3, 5 , 5	3, 5 , 5	4, 5 , 5	4, 5 , 5
80	2, 5 , 5	3, 5 , 5	4, 5 , 5	4, 5 , 5	2, 5 , 6	3, 5 , 6	4, 5 , 6	4, 5 , 6
90	2, 5 , 6	3, 5 , 6	5, 5 , 6	5, 5 , 6	2, 5 , 5	2, 5 , 5	5, 5 , 6	5, 5 , 6
100	2, 4 , 5	2, 4 , 5	5, 5 , 6	5, 5 , 6	2, 3 , 5	3, 3 , 5	5, 5 , 6	5, 5 , 6
110	2, 4 , 4	2, 4 , 4	5, 5 , 6	5, 5 , 6	2, 2 , 5	2, 3 , 5	5, 5 , 6	5, 5 , 6
120	1, 2 , 4	1, 2 , 4	5, 5 , 6	5, 5 , 6	1, 2 , 4	1, 2 , 4	5, 5 , 6	5, 5 , 6

Table A.1: Subjective image quality score (as derived from the reader study) of dark-field and absorption images for the right (R) and the left (L) lung at the different tube voltages. Values for the individual readings, as well as for the grouped readings are shown. Value triplets (one per reader) are given as: minimum, median (bold), maximum.

Signal strength score

kV	Dark-field, individual readings						
	60	70	80	90	100	110	120
R-UZ	2, 3 , 3	1, 3 , 3	1, 2 , 3	1, 2 , 2	1, 2 , 2	1, 1 , 2	1, 1 , 2
R-MZ	3, 4 , 4	2, 4 , 4	2, 3 , 3	2, 3 , 3	2, 2 , 3	1, 2 , 3	1, 2 , 3
R-LZ	3, 3 , 4	2, 3 , 4	2, 3 , 3	2, 3 , 3	2, 2 , 3	1, 1 , 3	1, 1 , 3
L-UZ	2, 3 , 3	1, 3 , 3	1, 3 , 3	1, 2 , 2	1, 2 , 2	1, 1 , 2	1, 1 , 2
L-MZ	4, 4 , 5	3, 4 , 4	2, 4 , 4	3, 3 , 4	2, 2 , 3	1, 2 , 3	1, 2 , 3
L-UZ	5, 5 , 5	4, 5 , 5	3, 3 , 4	3, 4 , 4	3, 3 , 4	2, 2 , 4	2, 2 , 3
kV	Absorption, individual readings						
	60	70	80	90	100	110	120
R-UZ	3, 4 , 5	3, 4 , 5	4, 4 , 5	4, 4 , 5	4, 4 , 5	4, 4 , 5	4, 5 , 5
R-MZ	2, 3 , 3	2, 3 , 3	2, 3 , 3	2, 3 , 3	2, 3 , 3	2, 3 , 3	2, 2 , 3
R-LZ	1, 2 , 2	1, 2 , 2	1, 2 , 2	1, 2 , 2	1, 2 , 2	1, 2 , 2	1, 2 , 3
L-UZ	4, 5 , 5	4, 5 , 5	4, 5 , 5	4, 5 , 5	4, 5 , 5	4, 5 , 5	4, 5 , 5
L-MZ	5, 5 , 5	5, 5 , 5	5, 5 , 5	5, 5 , 5	5, 5 , 5	5, 5 , 5	5, 5 , 5
L-UZ	2, 3 , 4	2, 3 , 4	3, 3 , 5	3, 3 , 5	3, 3 , 5	3, 3 , 5	3, 3 , 5
kV	Dark-field, grouped readings						
	60	70	80	90	100	110	120
R-UZ	2, 2 , 2	1, 2 , 3	1, 2 , 2	1, 2 , 2	1, 1 , 2	1, 1 , 2	1, 1 , 1
R-MZ	3, 3 , 4	2, 3 , 4	2, 3 , 3	2, 3 , 3	2, 2 , 2	1, 2 , 2	1, 2 , 2
R-LZ	2, 3 , 3	2, 3 , 3	2, 3 , 3	2, 3 , 3	2, 2 , 2	1, 2 , 2	1, 1 , 1
L-UZ	2, 3 , 3	1, 3 , 3	1, 2 , 2	1, 2 , 2	1, 1 , 2	1, 1 , 2	1, 1 , 1
L-MZ	3, 4 , 4	3, 4 , 4	2, 3 , 3	2, 3 , 3	2, 2 , 2	1, 2 , 3	1, 2 , 2
L-UZ	5, 5 , 5	4, 5 , 5	3, 4 , 4	3, 4 , 4	3, 3 , 3	2, 2 , 3	2, 2 , 2
kV	Transmission, grouped readings						
	60	70	80	90	100	110	120
R-UZ	3, 4 , 5	3, 4 , 5	4, 4 , 5	4, 4 , 5	4, 4 , 5	4, 4 , 5	4, 5 , 5
R-MZ	2, 3 , 3	2, 3 , 3	2, 3 , 3	2, 3 , 3	2, 3 , 3	2, 3 , 3	2, 3 , 3
R-LZ	1, 2 , 2	1, 1 , 2	1, 2 , 2	1, 2 , 2	1, 2 , 2	1, 2 , 2	1, 2 , 2
L-UZ	4, 5 , 5	4, 5 , 5	4, 5 , 5	4, 5 , 5	4, 5 , 5	4, 5 , 5	4, 5 , 5
L-MZ	5, 5 , 5	5, 5 , 5	5, 5 , 5	5, 5 , 5	5, 5 , 5	5, 5 , 5	5, 5 , 5
L-UZ	2, 3 , 4	2, 3 , 4	3, 3 , 5	3, 3 , 5	3, 3 , 5	3, 3 , 5	3, 3 , 5

Table A.2: Signal strength score of dark-field and absorption images (as derived from the reader study) at all examined tube voltages. Values for the individual readings as well as for the grouped readings are shown. Readings were performed for three zones of every lung, resulting in a total of six zones for every image [right/left lung: R/L, upper/middle/lower zone: UZ/MZ/LZ]. Value triplets (one per reader) are given as: minimum, median (**bold**), maximum.

Bibliography

- [AlsNielsen, 2011] Als-Nielsen, J. *Elements of Modern X-ray Physics* 2nd ed. (John Wiley and Sons, 2011) (Cited on pages [6](#), [8](#), [11–13](#)).
- [Andrejewski, 2021a] Andrejewski, J. *et al.* Whole-body x-ray dark-field radiography of a human cadaver. *Eur. Radiol. Exp.* **5** (2021) (Cited on page [61](#)).
- [Andrejewski, 2021b] Andrejewski, J. *et al.* Retrieval of 3D information in X-ray dark-field imaging with a large field of view. *submitted* (2021) (Cited on page [85](#)).
- [Andreo, 2017] Andreo, P., Burns, D. T., Nahum, A. E., Seuntjens, J. & Attix, F. H. *Fundamentals of Ionizing Radiation Dosimetry* (Wiley-VCH, 2017) (Cited on page [5](#)).
- [Arboleda, 2019] Arboleda, C. *et al.* Towards clinical grating-interferometry mammography. *European Radiology* **30**, 1419–1425 (2019) (Cited on page [2](#)).
- [Attwood, 1999] Attwood, D. *Soft X-rays and extreme ultraviolet radiation: Principles and Applications* (Cambridge University Press, 1999) (Cited on pages [5](#), [10](#), [11](#), [13](#), [14](#)).
- [Aumüller, 2020] Aumüller, G. *et al.* *Duale Reihe Anatomie* 5th ed. (Georg Thieme Verlag, 2020) (Cited on page [82](#)).
- [Bachche, 2017] Bachche, S. *et al.* Laboratory-based X-ray phase-imaging scanner using Talbot-Lau interferometer for non-destructive testing. *Scientific Reports* **7**, 6711 (2017) (Cited on page [2](#)).
- [Baum, 2015] Baum, T. *et al.* X-ray Dark-Field Vector Radiography — A Novel Technique for Osteoporosis Imaging. *J. Comput. Assisted Tomogr.* **39**, 286–289 (2015) (Cited on pages [3](#), [61](#), [67](#), [79](#)).
- [Bech, 2013] Bech, M. *et al.* In-vivo dark-field and phase-contrast x-ray imaging. *Sci. Rep.* **3**, 3209 (2013) (Cited on pages [2](#), [61](#)).
- [Behling, 2020] Behling, R. X-ray sources: 125 years of developments of this intriguing technology. *Physica Medica* **79**, 162–187 (2020) (Cited on page [7](#)).
- [Beirle, 2017] Beirle, S., Lampel, J., Lerot, C., Sihler, H. & Wagner, T. Parameterizing the instrumental spectral response function and its changes by a super-Gaussian and its derivatives. *Atmospheric Measurement Techniques* **10**, 581–598 (2017) (Cited on page [89](#)).

-
- [Bille, 2002] *Medizinische Physik 2 - Medizinische Strahlenphysik* (eds Bille, J. & Schlegel, W.) (Springer, 2002) (Cited on page [16](#)).
- [Biswas, 2000] Biswas, S. *Cosmic Perspectives in Space physics* (Springer, 2000) (Cited on page [5](#)).
- [Bonse, 1965] Bonse, U. & Hart, M. An X-Ray Interferometer. *Applied Physics Letters* **6**, 155–156 (1965) (Cited on page [1](#)).
- [Braig, 2018] Braig, E. M. *et al.* Simultaneous wood and metal particle detection on dark-field radiography. *European Radiology Experimental* **2** (2018) (Cited on page [61](#)).
- [Braig, 2020] Braig, E.-M. *et al.* X-ray Dark-Field Radiography: Potential for Visualization of Monosodium Urate Deposition. *Investigative Radiology* **55**, 494–498 (2020) (Cited on page [2](#)).
- [Buzug, 2008] Buzug, T. M. *Computed Tomography From Photon Statistics to Modern Cone-Beam CT* (Springer, 2008) (Cited on pages [10](#), [31](#)).
- [Cerrito, 2017] Cerrito, L. *Radiation and Detectors* (Springer, 2017) (Cited on page [5](#)).
- [Chabior, 2011] Chabior, M. *et al.* Signal-to-noise ratio in x ray dark-field imaging using a grating interferometer. *J. Appl. Phys* **10**, 053105 (2011) (Cited on page [40](#)).
- [Chabior, 2011] Chabior, M. *Contributions to the characterization of grating-based x-ray phase-contrast imaging* PhD thesis (Technische Universität Dresden, 2011) (Cited on page [23](#)).
- [Chapman, 1996] Chapman, H. N., Jacobsen, C. & Williams, S. A characterisation of dark-field imaging of colloidal gold labels in a scanning transmission X-ray microscope. *Ultramicroscopy* **62**, 191–213 (1996) (Cited on page [2](#)).
- [Clauser, 1992] Clauser, J. F. & Reinsch, M. W. New theoretical and experimental results in Fresnel optics with applications to matter-wave and X-ray interferometry. *Applied Physics B: Photophysics and Laser Chemistry* **54**, 380–395 (1992) (Cited on pages [2](#), [20](#)).
- [Cormack, 1963] Cormack, A. M. Representation of a function by its line integrals, with some radiological applications. *Journal of Applied Physics* **34**, 2722–2727 (1963) (Cited on pages [1](#), [28](#)).
- [Davis, 1995] Davis, T. J., Gao, D., Gureyev, T. E., Stevenson, A. W. & Wilkins, S. W. Phase-contrast imaging of weakly absorbing materials using hard X-rays. **373**, 595–598 (1995) (Cited on pages [2](#), [14](#)).

- [De Marco, 2019] De Marco, F. *et al.* Correlation of X-ray dark-field signal with thickness and ventilation pressure of in vivo pig lungs and CNR comparison with conventional radiography. *PLoS ONE* **14**, e0217858 (2019) (Cited on page 3).
- [De Marco, 2021] De Marco, F. *Image reconstruction, pre-clinical studies, and signal formation investigations at a dark-field chest radiography setup* PhD thesis (Technical University of Munich, 2021) (Cited on pages 32, 35, 38, 39, 70–72, 84).
- [De Marco, 2020] De Marco, F. *et al.* X-ray dark-field signal reduction due to hardening of the visibility spectrum. In: *arXiv.org*, arXiv:2011.03542 (2020) (Cited on page 2).
- [Desch, 1996] Desch, H. E. & M., D. J. *Timber: Structure, Properties, Conversion and Use* 7th ed. (Macmillan Press LTD, 1996) (Cited on page 81).
- [Diekmann, 2011] Diekmann, F. & Bick, U. Breast Tomosynthesis. *Seminars in Ultrasound, CT and MRI* **32**, 281–287 (2011) (Cited on page 31).
- [Donath, 2009] Donath, T. *et al.* Inverse geometry for grating-based x-ray phase-contrast imaging. *Journal of Applied Physics* **106**, 054703 (2009) (Cited on pages 21, 61).
- [Dössel, 2016] Dössel, O. *Bildgebende Verfahren in der Medizin* 2nd ed. (Springer, 2016) (Cited on pages 6, 16).
- [Eggl, 2015] Eggl, E. *et al.* Prediction of Vertebral Failure Load by Using X-Ray Vector Radiographic Imaging. *Radiology* **275**, 553–561 (2015) (Cited on pages 3, 61, 67, 79).
- [Eggl, 2016] Eggl, E. *et al.* X-ray phase-contrast tomosynthesis of a human ex vivo breast slice with an inverse Compton x-ray source. *EPL (Europhysics Letters)* **116**, 68003 (2016) (Cited on page 85).
- [Ekpo, 2014] Ekpo, E. U., Hoban, A. C. & McEntee, M. F. Optimisation of direct digital chest radiography using Cu filtration. *Radiography* **20**, 346–350 (2014) (Cited on pages 42, 51, 58, 60).
- [Fingerle, 2019] Fingerle, A. A. *et al.* Imaging features in post-mortem x-ray dark-field chest radiographs and correlation with conventional x-ray and CT. *European radiology experimental* **3**, 25 (2019) (Cited on page 3).
- [Frank, 2021] Frank, M. *et al.* Dosimetry on first clinical dark-field chest radiography. *Medical Physics* **n/a**. eprint: <https://aapm.onlinelibrary.wiley.com/doi/pdf/10.1002/mp.15132> (2021) (Cited on pages 3, 53, 96).

-
- [Garrett, 2015] Garrett, J., Ge, Y., Li, K. & Chen, G.-H. Correction of data truncation artifacts in differential phase contrast (DPC) tomosynthesis imaging. *Physics in Medicine and Biology* **60**, 7713–7728 (2015) (Cited on page 85).
- [Gassert, 2021] Gassert, F. T. *et al.* X-ray Dark-Field Chest Imaging: Qualitative and Quantitative Results in Healthy Humans. *Radiology* **0**, 210963 (2021) (Cited on pages 3, 53).
- [Gratton, 1970] *Non-Solar X- and Gamma-Ray Astronomy* (ed Gratton, L.) (Springer, 1970) (Cited on page 5).
- [Gromann, 2017] Gromann, L. *Development of a large-animal X-ray dark-field scanner* PhD thesis (Technical University of Munich, 2017) (Cited on pages 3, 25, 32, 61, 66).
- [Grossmann, 1935] Grossmann, G. Imaging features in post-mortem x-ray dark-field chest radiographs and correlation with conventional x-ray and CT. *The British journal of Radiology* **8**, 733–751 (1935) (Cited on pages 1, 28).
- [Hauke, 2018] Hauke, C. *et al.* A preclinical Talbot-Lau prototype for x-ray dark-field imaging of human-sized objects. *Medical Physics* **45**, 2565–2571 (2018) (Cited on pages 3, 24, 61, 66).
- [Hellbach, 2015] Hellbach, K. *et al.* In vivo dark-field radiography for early diagnosis and staging of pulmonary emphysema. *Investigative Radiology* **50**, 430–435 (2015) (Cited on page 2).
- [Hellbach, 2016] Hellbach, K. *et al.* Facilitated Diagnosis of Pneumothoraces in Newborn Mice Using X-ray Dark-Field Radiography. *Invest. Radiol.* **51**, 597–601 (2016) (Cited on pages 2, 61).
- [Hellbach, 2018a] Hellbach, K. *et al.* Depiction of pneumothoraces in a large animal model using x-ray dark-field radiography. *Scientific Reports* **8**, 2602 (2018) (Cited on page 3).
- [Hellbach, 2018b] Hellbach, K. *et al.* X-Ray Dark-field Imaging to Depict Acute Lung Inflammation in Mice. *Scientific Reports* **8**, 2096 (2018) (Cited on page 2).
- [Horn, 2017] Horn, F. *et al.* High-energy x-ray Talbot–Lau radiography of a human knee. *Physics in Medicine & Biology* **62**, 6729–6745 (2017) (Cited on page 3).
- [Hounsfield, 1973] Hounsfield, G. N. Computerized transverse axial scanning (tomography): Part I description of system. *British Journal of Radiology* **46**, 1016–1022 (1973) (Cited on pages 1, 28).
- [Ingal, 1995] Ingal, V. N. & Beliaevskaya, E. A. X-ray plane-wave topography observation of the phase contrast from a non-crystalline object. *Journal of Physics D: Applied Physics* **28**, 2314–2317 (1995) (Cited on page 2).

- [Jensen, 2010a] Jensen, T. H. *et al.* Directional x-ray dark-field imaging. *Physics in Medicine and Biology* **55**, 3317–3323 (2010) (Cited on pages 3, 26, 79).
- [Jensen, 2010b] Jensen, T. H. *et al.* Directional x-ray dark-field imaging of strongly ordered systems. *Physical Review B* **82**, 214103 (2010) (Cited on pages 3, 79).
- [Jud, 2017] Jud, C. *et al.* Trabecular bone anisotropy imaging with a compact laser-undulator synchrotron x-ray source. *Scientific Reports* **7**, 14477 (2017) (Cited on pages 3, 79, 83).
- [Jud, 2018] Jud, C. *X-ray Vector Radiography for Biomedical Applications* PhD thesis (Technical University of Munich, 2018) (Cited on pages 19, 26, 27, 83).
- [Kenntner, 2012] Kenntner, J. *et al.* Fabrication and characterization of analyzer gratings with high aspect ratios for phase contrast imaging using a Talbot interferometer. *AIP Conference Proceedings* **1437**, 89–93 (2012) (Cited on page 24).
- [Koehler, 2015] Koehler, T. *et al.* Slit-scanning differential x-ray phase-contrast mammography: Proof-of-concept experimental studies. *Medical Physics* **42**, 1959–1965 (2015) (Cited on pages 3, 25).
- [Korenblum, 1958] Korenblum, B. I., Tetelbaum, S. I. & Tyutin, A. A. ОБ ОДНОЙ СХЕМЕ ТОМОГРАФИИ [About one scheme of tomography]. ИЗВЕСТИЯ ВЫСШИХ УЧЕБНЫХ ЗАВЕДЕНИЙ – РАДИОФИЗИКА [*Proceedings of higher educational institutions – Radiophysics*] **1**, 151–157 (1958). Translation: A. Gustschin, 2020, arXiv:2004.03750 [eess.IV] (Cited on pages 1, 28, 30).
- [Kottler, 2007] Kottler, C., Pfeiffer, F., Bunk, O., Grünzweig, C. & David, C. Grating interferometer based scanning setup for hard x-ray phase contrast imaging. *Review of Scientific Instruments* **78**, 043710 (2007) (Cited on pages 3, 23, 25, 69, 77).
- [Lau, 1948] Lau, E. Beugungserscheinungen an Doppelrastern. *Annalen der Physik* **2**, 418–423 (1948) (Cited on page 20).
- [Li, 2014] Li, K. *et al.* Grating-based phase contrast tomosynthesis imaging: Proof-of-concept experimental studies. *Medical Physics* **41**, 011903 (2014) (Cited on page 85).
- [Littelton, 1996] Littelton, J. T. & Durizch Littelton, M. L. in *A History of the Radiological Sciences* (eds Gagliardi, R. & McClellan, B. L.) (Radiology Centennial, Inc., 1996) (Cited on pages 1, 28).
- [Ludwig, 2019] Ludwig, V. *et al.* Exploration of different X-ray Talbot-Lau setups for dark-field lung imaging examined in a porcine lung. *Physics in Medicine and Biology* **64** (2019) (Cited on page 3).

-
- [Lynch, 2011] Lynch, S. K. *et al.* Interpretation of dark-field contrast and particle-size selectivity in grating interferometers. *Appl. Opt.* **50**, 4310 (2011) (Cited on page 2).
- [Malecki, 2013] Malecki, A. *et al.* Coherent Superposition in Grating-Based Directional Dark-Field Imaging. *PLOS ONE* **8**, e61268 (2013) (Cited on pages 79, 80).
- [Malecki, 2014] Malecki, A. *et al.* Correlation of X-Ray Dark-Field Radiography to Mechanical Sample Properties. *Microsc. Microanal.* **20**, 1528–1533 (2014) (Cited on page 80).
- [Malecki, 2015] Malecki, A. *X-Ray Tensor Tomography – From Two-Dimensional Directional X-Ray Dark-Field Imaging to Three Dimensions* PhD thesis (Technical University of Munich, 2015) (Cited on page 21).
- [Meinel, 2014] Meinel, F. G. *et al.* Improved Diagnosis of Pulmonary Emphysema Using In Vivo Dark-Field Radiography. *Invest. Radiol.* **49**, 653–658 (2014) (Cited on pages 2, 61).
- [Mohr, 2012] Mohr, J. *et al.* High aspect ratio gratings for X-ray phase contrast imaging. *AIP Conference Proceedings* **1466**, 41–50 (2012) (Cited on page 24).
- [Momose, 2003] Momose, A. *et al.* Demonstration of X-Ray Talbot Interferometry. *Japanese Journal of Applied Physics* **42**, L866–L868 (2003) (Cited on pages 2, 18).
- [Momose, 2014] Momose, A. *et al.* X-ray phase imaging: From synchrotron to hospital. *Philosophical transactions. Series A, Mathematical, physical, and engineering sciences* **372**, 20130023 (2014) (Cited on page 3).
- [Morrison, 1992] Morrison, G. R. & Browne, M. T. Dark-field imaging with the scanning transmission x-ray microscope. *Review of Scientific Instruments* **63**, 611–614 (1992) (Cited on page 2).
- [Muhogora, 2012] Muhogora, W. *et al.* Comparison of image quality and patient dose for chest x-ray examinations on conventional and low cost computed radiography systems. *Radiography* **18**, 275–278 (2012) (Cited on pages 42, 51, 58, 60).
- [Nagashima, 2013] Nagashima, M. *et al.* Application of X-ray grating interferometry for the imaging of joint structures. *Anatomical science international* **89**, 95–100 (2013) (Cited on page 3).
- [Niklason, 1997] Niklason, L. T. *et al.* Digital tomosynthesis in breast imaging. *Radiology* **205**, 399–406 (1997) (Cited on pages 31, 85, 87).
- [Harris, 2020] Harris, C. R. *et al.* Array programming with NumPy. *Nature* **585**, 357–362 (2020) (Cited on page 54).

- [Park, 2007] Park, J. M., Franken, E. A., Garg, M., Fajardo, L. L. & Niklason, L. T. Breast Tomosynthesis: Present Considerations and Future Applications. *RadioGraphics* **27**, S231–S240 (2007) (Cited on page 31).
- [Pelzer, 2016] Pelzer, G. *et al.* A beam hardening and dispersion correction for x-ray dark-field radiography. *Med. Phys.* **43**, 2774–2779 (2016) (Cited on page 40).
- [Pfeiffer, 2006] Pfeiffer, F., Weitkamp, T., Bunk, O. & David, C. Phase retrieval and differential phase-contrast imaging with low-brilliance X-ray sources. *Nature Physics* **2**, 258–261 (2006) (Cited on pages 2, 20).
- [Pfeiffer, 2008] Pfeiffer, F. *et al.* Hard-X-ray dark-field imaging using a grating interferometer. *Nat. Mater.* **7**, 134–137 (2008) (Cited on pages 2, 20).
- [Podgorsak, 2016] Podgorsak, E. *Radiation Physics for Medical Physicists* 3rd (Springer, 2016) (Cited on pages 10, 11).
- [Potdevin, 2012] Potdevin, G. *et al.* X-ray vector radiography for bone micro-architecture diagnostics. *Physics in Medicine and Biology* **57**, 3451–3461 (2012) (Cited on pages 3, 79).
- [Prade, 2015] Prade, F., Yaroshenko, A., Herzen, J. & Pfeiffer, F. Short-range order in mesoscale systems probed by X-ray grating interferometry. *EPL (Europhysics Letters)* **112**, 68002 (2015) (Cited on page 61).
- [Prade, 2016] Prade, F. *et al.* Time resolved X-ray Dark-Field Tomography Revealing Water Transport in a Fresh Cement Sample. *Scientific Reports* **6**, 29108 (2016) (Cited on page 2).
- [Prade, 2017] Prade, F. *Grating-based X-ray Dark-Field Imaging: Theory and Applications in Materials Research* PhD thesis (Technical University of Munich, 2017) (Cited on page 19).
- [Qin, 2010] *Micro-Manufacturing Engineering and Technology* (ed Qin, Y.) (William Andrew Publishing, 2010) (Cited on page 24).
- [Rauch, 2020] Rauch, T. *et al.* Discrimination analysis of breast calcifications using x-ray dark-field radiography. *Medical Physics* **47**, 1813–1826 (2020) (Cited on page 66).
- [Revol, 2010] Revol, V., Kottler, C., Kaufmann, R., Straumann, U. & Urban, C. Noise analysis of grating-based x-ray differential phase contrast imaging. *Rev. Sci. Instrum* **81**, 073709 (2010) (Cited on page 40).

-
- [Revol, 2012] Revol, V., Kottler, C., Kaufmann, R., Neels, A. & Dommann, A. Orientation-selective X-ray dark field imaging of ordered systems. *Journal of applied physics* **112**, 114903 (2012) (Cited on page 79).
- [Röntgen, 1895] Röntgen, W. C. Ueber eine neue Art von Strahlen. Vorläufige Mittheilung. *Sitzungs-Berichte der Physikalisch-medicinischen Gesellschaft zu Würzburg*, 132–141 (1895) (Cited on page 1).
- [Sauter, 2019] Sauter, A. P. *et al.* Optimization of tube voltage in X-ray dark-field chest radiography. *Scientific Reports* **9**, 8699 (2019) (Cited on page 42).
- [Sauter, 2021] Sauter, A. P. *et al.* Correlation of image quality parameters with tube voltage in X-ray dark-field chest radiography: a phantom study. *Scientific Reports* **11**, 14130 (2021) (Cited on page 42).
- [Schaff, 2014] Schaff, F. *et al.* Correlation of x-ray vector radiography to bone micro-architecture. *Scientific Reports* **4**, 3695 (2014) (Cited on pages 3, 79).
- [Scherer, 2016] Scherer, K. *et al.* Improved Diagnostics by Assessing the Micromorphology of Breast Calcifications via X-Ray Dark-Field Radiography. *Scientific Reports* **6**, 2045–2322 (2016) (Cited on page 66).
- [Scherer, 2017] Scherer, K. *et al.* X-ray Dark-field Radiography - In-Vivo Diagnosis of Lung Cancer in Mice. *Sci. Rep.* **7**, 402 (2017) (Cited on pages 2, 61).
- [Schleede, 2012] Schleede, S. *et al.* Emphysema diagnosis using X-ray dark-field imaging at a laser-driven compact synchrotron light source. *Proceedings of the National Academy of Sciences* **109**, 17880–17885 (2012) (Cited on pages 2, 61).
- [Schleede, 2013] Schleede, S. *et al.* X-ray phase-contrast tomosynthesis for improved breast tissue discrimination. *European Journal of Radiology* **83**, 531–536 (2013) (Cited on page 85).
- [Virtanen, 2020] Virtanen, P. *et al.* SciPy 1.0: Fundamental Algorithms for Scientific Computing in Python. *Nature Methods* **17**, 261–272 (2020) (Cited on page 54).
- [Seibert, 2005] Seibert, J. A. & Boone, J. M. X-ray imaging physics for nuclear medicine technologists. Part 2: X-ray interactions and image formation. *Journal of Nuclear Medicine Technology* **33**, 3–18 (2005) (Cited on pages 9, 14, 16).
- [Seifert, 2019] Seifert, M. *et al.* Talbot-Lau x-ray phase-contrast setup for fast scanning of large samples. *Scientific Reports* **9**, 1–11 (2019) (Cited on pages 3, 67, 69, 77).

- [Snigirev, 1995] Snigirev, A., Snigireva, I., Kohn, V., Kuznetsov, S. & Schelokov, I. On the possibilities of x-ray phase contrast microimaging by coherent high-energy synchrotron radiation. *Review of Scientific Instruments* **66**, 5486–5492 (1995) (Cited on page 2).
- [Standring, 2015] *Gray's Anatomy* 41st ed. (ed Standring, S.) (Elsevier, 2015) (Cited on page 82).
- [Strobl, 2014] Strobl, M. General solution for quantitative dark-field contrast imaging with grating interferometers. *Scientific Reports* **4**, 7243 (2014) (Cited on page 2).
- [Talbot, 1836] Talbot, H. F. Facts relating to Optical Science. *Philosophical Magazine* **9**, 401–407 (1836) (Cited on page 17).
- [Tanaka, 2012] Tanaka, J. *et al.* Cadaveric and in vivo human joint imaging based on differential phase contrast by X-ray Talbot-Lau interferometry. *Zeitschrift für medizinische Physik* **23**, 222–227 (2012) (Cited on page 2).
- [Tetelbaum, 1957] Tetelbaum, S. I. О МЕТОДЕ ПОЛУЧЕНИЯ ОБЪЕМНЫХ ИЗОБРАЖЕНИЙ ПРИ ПОМОЩИ РЕНТГЕНОВСКОГО ИЗЛУЧЕНИЯ [About a method of obtaining volumetric images by means of X-ray radiation]. Известия Киевского Ордена Ленина Политехнического Института [*Bulletin of the Kiev Polytechnic Institute*] **22**, 154–160 (1957). Translation: A. Gustschin, 2020, arXiv:2001.03806 [physics.hist-ph] (Cited on pages 1, 28, 30).
- [Tilli, 2010] *Handbook of Silicon Based MEMS Materials and Technologies* (eds Tilli, M. *et al.*) (William Andrew Publishing, 2010) (Cited on page 24).
- [Umkehrer, 2020] Umkehrer, S. *et al.* A proof-of-principal study using phase-contrast imaging for the detection of large airway pathologies after lung transplantation. *Sci. Rep.* **10**, 18444 (2020) (Cited on page 61).
- [vdPlaats, 1980] Van der Plaats, G. J. *Medical X-ray Techniques in Diagnostic Radiology* 4th ed. (Marinus Nijhoff Publishers, 1980) (Cited on page 6).
- [Wall, 2011] Wall, B. *et al.* *Radiation risks from medical X-ray examinations as a function of the age and sex of the patient* (Health Protection Agency, Centre for Radiation, Chemical and Environmental Hazards, 2011) (Cited on pages 1, 16, 62, 64, 96, 119).
- [Webb, 1990] Webb, S. *From the Watching of Shadows – The Origins of Radiological Tomography* (IOP Publishing Ltd, 1990) (Cited on pages 28–30).

-
- [Weitkamp, 2005] Weitkamp, T. *et al.* X-ray phase imaging with a grating interferometer. *Optics Express* **13**, 6296 (2005) (Cited on page 2).
- [Weitkamp, 2006] Weitkamp, T., David, C., Kottler, C., Bunk, O. & Pfeiffer, F. *Tomography with grating interferometers at low-brilliance sources* in *Developments in X-Ray Tomography V* (SPIE, 2006), 63180S (Cited on page 18).
- [Wilkins, 1996] Wilkins, S. W., Gureyev, T. E., Gao, D., Pogany, A. & Stevenson, A. W. Phase-contrast imaging using polychromatic hard X-rays. *Nature* **384**, 335–338 (1996) (Cited on page 2).
- [Willer, 2018] Willer, K. *et al.* X-ray dark-field imaging of the human lung—A feasibility study on a deceased body. *PLOS ONE* **13** (ed Nolan, A.) (2018) (Cited on pages 3, 53, 61, 66).
- [Willer, 2021] Willer, K. *et al.* X-ray Dark-Field Chest Imaging can Detect and Quantify Emphysema in COPD Patients – A Diagnostic Accuracy Study. *The Lancet Digital Health* **3**, e733–44 (2021) (Cited on pages 3, 99).
- [Willmott, 2011] Willmott, P. *An Introduction to Synchrotron Radiation: Techniques and Applications* (John Wiley and Sons, 2011) (Cited on pages 7, 9, 11–14).
- [Willner, 2016] Willner, M. *Quantitative phase-contrast computed tomography for biomedical applications* PhD thesis (Technical University of Munich, 2016) (Cited on page 22).
- [Yanch, 2009] Yanch, J. C., Behrman, R. H., Hendricks, M. J. & McCall, J. H. Increased Radiation Dose to Overweight and Obese Patients from Radiographic Examinations. *Radiology* **252**, 128–139 (2009) (Cited on page 51).
- [Yaroshenko, 2013] Yaroshenko, A. *et al.* Pulmonary emphysema Diagnosis with a Preclinical small-animal X-ray Dark-Field scatter-contrast scanner. *Radiology* **269**, 427–433 (2013) (Cited on page 2).
- [Yaroshenko, 2015] Yaroshenko, A. *et al.* Improved In vivo Assessment of Pulmonary Fibrosis in Mice using X-Ray Dark-Field Radiography. *Sci. Rep.* **5**, 17492 (2015) (Cited on pages 2, 61).
- [Yashiro, 2010] Yashiro, W., Terui, Y., Kawabata, K. & Momose, A. On the origin of visibility contrast in x-ray Talbot interferometry. *Opt. Express* **18**, 16890–16901 (2010) (Cited on page 2).
- [Yashiro, 2015] Yashiro, W., Vagovič, P. & Momose, A. Effect of beam hardening on a visibility-contrast image obtained by X-ray grating interferometry. *Optics Express* **23**, 23462 (2015) (Cited on page 67).
- [Zdora, 2018] Zdora, M.-C. State of the Art of X-ray Speckle-Based Phase-Contrast and Dark-Field Imaging. *Journal of Imaging* **4** (2018) (Cited on page 2).

Bibliography

- [Zernike, 1942] Zernike, F. Phase contrast, a new method for the microscopic observation of transparent objects. *Physica* **9**, 686–698 (1942) (Cited on page [1](#)).
- [Ziedses des Plantes, 1932] Ziedses des Plantes, B. G. Eine neue Methode zur differenzierung in der Röntgenographie (Planigraphie). *Acta Radiologica* **13**, 182–192 (1932) (Cited on pages [1](#), [29](#)).

Abbreviations

2D	Two-dimensional
3D	Three-dimensional
AD	Absorbed dose
CT	Computed tomography
CNR	Contrast to noise ratio
DAP	Dose area product
DRIE	Deep reactive-ion etching
ESD	Entrance surface dose
ED	Effective dose
EqD	Equivalent dose
FWEM	Full width 1/e th minimum
G₀	Source grating
G₁	Reference grating
G₂	Analyser grating
KERMA	Kinetic energy released per unit mass
LIGA	German acronym for Lithographie, Galvanoformung, Abformung; English: lithography, electroplating, molding
POM	Polyoxymethylene
ROI	Region of interest
XVR	X-ray vector radiography

Symbols

\tilde{A}	Mean of stepping curve
A	Attenuation
\bar{A}	Mean attenuation
a	Area
C	Contrast
c	Speed of light in vacuum, $c = 2.9979 \cdot 10^8$ m/s
\mathfrak{D}	Visibility reduction
$\mathfrak{D}_{\text{corr}}$	Beam hardening corrected visibility reduction
D	Dark-field
\bar{D}	Mean dark-field
D_A	Degree of anisotropy
d	Distance between reference and analyser grating
d_T	Talbot distance
E	Photon energy
E_b	Binding energy
E_k	Kinetic energy
f	Atomic scattering factor
f'	Real part of atomic dispersion correction
f''	Imaginary part of atomic dispersion correction
f_{tot}	Total (complex) atomic scattering factor
H	Number of total steps
h	Height over sample table
h_p	Planck-constant, $h_p = 6.626 \cdot 10^{-34}$ Js
I	Intensity
I_0	Intensity of incoming wave
I_k	Intensity of stepping curve
I_{max}	Maximal intensity
I_{min}	Minimal intensity
j	Pixel index

\vec{k}	Wave vector
k_0	Length of wave vector in vacuum
l	Distance between source and reference grating
L_L	Longitudinal coherence length
L_T	Transverse coherence length
M	Magnification factor
\mathfrak{M}	Arithmetic mean
m	Factor dependent on grating type
m_e	Mass of electron
N	Number of atoms per unite volume
n	Complex refractive index
p_0	Period of source grating
p_1	Period of reference grating
p_2	Period of analyser grating
\vec{Q}	Scattering vector
R	Distance to source
\vec{r}	Position vector
r_e	Electron radius,
ref	Reference measurement
s	Shift of intensity pattern
S	Sensitivity
S_D	Source size
sam	Sample measurement
\overline{SD}	Source detector distance
\overline{SO}	Source object distance
T	Transmission
t	Time
V	Visibility
w_r	Radiation weighting factor (for X-rays: $w_r = 1$)
w_t	Tissue weighting factor
w_w	Weighting factor given in [Wall, 2011]
Z	Atomic number
α	Refractive angle

A Abbreviations

β	Absorption index
δ	Refractive index decrement
ϵ	Angle between the propagation direction of the incident photon and the scattered photon
ε	Propagation direction angle
H	Number of total steps
η	Iteration over steps
Θ	Sample orientation around the optical axis
θ	Orientation of scattering structure
θ_s	Angle between the direction of sensitivity and the x-axis.
λ	Wavelength
μ	Absorption coefficient
ν	Frequency of radiation
ρ	Density
ρ_a	Atomic number density
Σ	Standard deviation
σ_{coh}	Cross section of coherent scattering
$\sigma_{\text{e,coh}}$	Electronic cross section of coherent scattering
σ_{incoh}	Cross section of incoherent scattering
$\sigma_{\text{incoh}}^{\text{KN}}$	Klein-Nishina cross section of incoherent scattering
σ_{ph}	Cross section of photoelectric effect
$\sigma_{\text{e,R}}$	Rayleigh cross section
σ_{R}	Atomic Rayleigh cross section
$\sigma_{\text{e,Th}}$	Thomson cross section
σ_{Th}	Atomic Thomson cross section
σ_{tot}	Total atomic cross section
σ_{Ph}	Atomic cross section of photoelectric effect
τ	Index of relative position of sample and slot
$\Delta\Phi$	Phase shift of wave
ϕ_η	Lateral shift of stepped grating
φ	Phase of stepping curve
$\Delta\varphi$	Phase of stepping curve
Ψ	Wave function
Ψ_0	Amplitude of wave

ω Angular frequency
 ω_r Angular resonance frequency

Acknowledgements

During my time at E17 and the course of this work I received great support and assistance without which this thesis would not have been possible.

My deepest gratitude goes to Prof. Dr. Julia Herzen for giving me the opportunity to work on this project and be part of E17 and her group. Thank you, Julia, for giving me the freedom to realise my ideas, but always providing me with support, advice, and guidance in case of problems.

I want to thank Prof. Dr. Franz Pfeiffer for piquing my interest in X-ray imaging with his lectures and his support during my master's and PhD time.

I am very grateful to Dr. Fabio De Marco for his endless support and many invaluable discussions on various topics. Thank you, for sharing your knowledge and helping me with all kinds of problems during my work.

Special thanks go to Konstantin Willer, Manuela Frank, Theresa Urban, Wolfgang Noichl, and Rafael Schick for our many fruitful discussions and support on both processing and experimental issues.

I am grateful to Dr. Thomas Koehler and the rest of Philips Medical Systems team in Hamburg for their support and providing the hardware and software for the *linescanner* setup.

I would like to thank Dr. Daniela Pfeiffer, Dr. Andreas Sauter, Dr. Alexander A. Fingerle and Dr. Felix Meurer for their great assistance and contributions during our collaborations.

Many thanks go to Dr. Christian Braun, Dr. Florian Fischer, and Fabian Kriner from the Institut für Rechtsmedizin, Ludwig-Maximilians-Universität München, for their support in the human cadaver studies.

I am very thankful to Dr. Pascal Meyer and Alex Gustschin for their assistance on all matters concerning gratings.

I also want to thank my bachelor students Franziska Hinterdobler and Annika Ries for their assistance. It was a lot of fun to work with you.

I am grateful to Dr. Martin Dierolf for sharing his knowledge on many occasions and his support on various technical problems.

Many thanks go to Alen Begic for constructing customised, fancy components for the *line-scanner* setup.

Special thanks go to Dr. Fabio De Marco, Manuela Frank, Lisa Heck, Simon Pinzek, and

Theresa Urban for proof-reading this thesis.

A big thank you goes to Dr. Martin Dierolf, Wolfgang Noichl, Clemens Schmid and all the others who keep the IT-infrastructure at E17 running.

I am very grateful to Nelly de Leiris, Dr. Klaus Achterhold, and Veronica Bodek for their assistance in all the administrative and bureaucratic work.

I would like to thank everyone at the Chair of Biomedical Physics and the Group for Biomedical Imaging Physics for the great working atmosphere and fun times during breaks, at the seminar days, and other activities.

Finally, I would like to thank my family and friends for their everlasting support throughout the years.